MODELING OF CONSOLIDATION AND FLOW OF GRANULAR MATERIAL UNDER VARYING CONDITIONS

by

Adel F. Alenzi

B.Sc. in ChE, University of Missouri-Columbia, MO, USA, 1996

M.Sc. in ChE, Kuwait University, Kuwait, 2002

Submitted to the Graduate Faculty of

the Swanson School of Engineering in partial fulfillment

of the requirements for the degree of

Doctor of Philosophy

University of Pittsburgh

2012

UNIVERSITY OF PITTSBURGH

SWANSON SCHOOL OF ENGINEERING

This dissertation was presented

by

Adel F. Alenzi

It was defended on

June 27, 2012

and approved by

Joseph J. McCarthy, Ph.D., Professor, Department of Chemical and Petroleum Engineering

Robert S. Parker, Ph.D., Associate Professor, Department of Chemical and Petroleum Engineering

Robert M. Enick, Ph.D., Professor, Department of Chemical and Petroleum Engineering

Luis E. Vallejo, Ph.D., Professor, Department of Civil and Environmental Engineering

Dissertation Director: Joseph J. McCarthy, Ph.D., Professor, Department of Chemical and Petroleum Engineering

MODELING OF CONSOLIDATION AND FLOW OF GRANULAR MATERIAL UNDER VARYING CONDITIONS

Adel F. Alenzi, PhD

University of Pittsburgh, 2012

Granular materials are ubiquitous. They are widely used in many natural and man-made processes such as formation of lunar regolith, dunes and beach sand, as well as processes in pharmaceutical, chemical, and construction industries. Despite their clear industrial relevance, a fundamental understanding of most of the phenomena that involve granular materials in the chemical industry is lacking. Recently, it has been found that cyclic variation of the temperature of a granular bed can cause static particle beds to consolidate (increase their packing fraction) over time due to thermo-mechanical coupling. We employ experimental techniques and numerical simulations, using the thermal particle dynamics method (TPD), to study this phenomenon. In order to simulate many natural phenomena such as lunar regolith formation, one needs to determine a simulation depth of the bed which will yield realistic results yet be manageable computationally. Here we use penetration theory to estimate the required simulation bed height. Lateral periodic boundary conditions are used in our simulations to show that consolidation still occurs during vertical heating even in the absence of confining side walls.

Granular flows in which shearing plays a key role are prevalent in natural and industrial applications and understanding their behavior and flow characteristics is of considerable importance. Nevertheless, difficulties in making accurate experimental measurements, complexities involved in doing bulk characterization, and the non-linear nature of interparticle interactions have made development and testing of theoretical models extremely challenging. For this reason, the discrete element method (DEM) is often used as the gold standard for

comparison to continuum-level theories of granular material flows. Due to the fact that this modeling approach is derived from first-principle constructs – like contact mechanics – its use in lieu of experimentation is reasonably wide-spread and is becoming a staple even in industrial practice. In this work, we explore various aspects of quantitative validation of DEM simulations using detailed measurements of simple, well-characterized flows that allow us to examine the effect of rough surfaces, rotational rates, collisional and frictional force models on granular flow using different devices. Experimentally, we use digital particle tracking velocimetry (DPTV) to obtain velocity, solids fractions, and granular temperature profiles. Computationally, we compare the results obtained using different contact mechanics force laws to those from experimental measurements and perform sensitivity analyses on device and particle geometry as well as material properties employed. In general, the frictional force models range from pragmatic linear techniques to rigorously more complex (nonlinear) contact mechanics inspired routines. Here, we examine both force models to compare with the experimental measurements. In addition, we examine the robustness of these observations to both particle materials properties as well as systemic variables (such as total system solids fraction).

Keywords: Particle Dynamics (PD), Thermal Particle Dynamics (TPD), DEM, Thermoelastic Contact, Granular Media, Thermal Cycling, Solid Fraction, Consolidation, Granular Flow, Shear Cell, Collisional Flow, Normal Forces, Frictional Forces.

TABLE OF CONTENTS

LIST OF TABLES

LIST OF FIGURES

PREFACE

I am extremely grateful to many people who made this work a success technically, financially and emotionally.

My advisor, Prof. Joseph J. McCarthy, with his extensive knowledge and long experience is the kind of leader that every young researcher wants to have. I am extremely indebted to Prof. McCarthy for his unconditional guidance, respect, support, and encouragement throughout the journey of my PhD work. The wisdom I gained while working with him would stay with me for a life-time.

I am also thankful to all of my PhD committee members, Prof. Robert Parker, Prof. Robert Enick and Prof. Luis E. Vallejo for their excellent comments and suggestions which enriched the quality of this work.

The work in this thesis would not have been accomplished without the financial support of my sponsor, Public Authority for Applied Education and Training (PAAET), Kuwait. Specifically, I would like to thank Shoghig Sahakyan for her help and support during my study at Pitt.

In addition, I would like to thank my friends and colleagues who accompanied me during my stay at Pittsburgh, particularly, Tathagata Bhattacharya. I am also grateful to my past lab-mates: Watson Vargas, Isabel Figueroa, Suman Hajra and Deliang Shi, for their help and support.

Finally, I wish to acknowledge my family whose infinite patience and understanding are never taken for granted. My wife Khawlah Alenezi and my kids Bander, Fawaz, Yousef and Maryam (Ema) provide me with the energy to complete this work.

1.0 INTRODUCTION

Granular media are frequently encountered in different fields of science and industry. They are also among the most commonly used materials in human activities. Handling, storage, and processing of these materials is significant in industries such as pharmaceutical, petrochemical, and polymers. Although heterogeneous media have received much attention, most of the phenomena that involve granular materials in the chemical industry are far from being well understood. These materials often behave differently from ordinary single phase systems, and their physicochemical and transport properties are of interest in the analysis, design, and optimization of industrial processes, and in the understanding of natural phenomena. When granular materials consolidate, dramatic effects can result. Every year, hundreds of industrial silos, bins and hoppers used for storage and handling purposes experience some problems or failure due to the compaction/consolidation that takes place during storage. In contrast with mechanical consolidation, the increase in granular packing (consolidation) can be achieved by simply raising and then lowering the temperature in a cyclic manner (Thermal Cycling) as might be encountered in simple day-night thermal variation.

While particle phenomena has been an area of active research since the time of Reynolds [1], a solid fundamental understanding of transport in particulate systems is not yet complete. Heat conduction, in particular, is a relevant topic in many different disciplines where knowledge of the thermal conduction phenomena is essential for the analysis of the associated heat transport processes. Studying these systems requires the determination and use of effective properties, which are unfortunately difficult to measure experimentally and may sometimes be imprecise. It has been shown computationally [2] and experimentally [3] that even in simple, non-cohesive, elastic particles stress is not distributed uniformly, but is principally carried in chains. We believe that a primary reason for the failure of previous theories

in bulk property determination (see [4, 5]) lies in the fact that particle forces/interactions are inherently non-uniform, and that it is, in fact, the non-uniformities themselves that determine many of the bulk properties.

A better understanding of the basic processes governing granular flow is critically important to a wide variety of industries such as mining and food processing, as well as scientific applications. However, a fundamental understanding of the flow of granular materials has yet to be achieved. While granular flows can behave, under certain conditions, similarly to other forms of matter such as solids, liquids, or gases [6,7], there is no accepted set of governing equations of motion describing the behavior of granular flow. In addition, it is difficult to experimentally measure the bulk properties of the materials (e.g., stress, strain, voidage, etc.) as well as the macroscopic flow variables such as velocity and granular temperature profiles [8]. Examples of experimental granular shearing studies include positron tomography [9, 10], magnetic resonance imaging [11], gamma ray tomography [12], direct particle tracking [13–18], or combined techniques [19]. However, no technique has been proven ideal to build and/or validate theoretical models [8].

Simulation of granular flows provides a useful means of investigating particulate behavior. As a support to experiments, a number of computational modeling studies of particulate flows [20–23] were used to gain an insight into the behavior of granular shearing flow. In particular, Particle Dynamics (PD) has gained widespread acceptance as a viable and well developed technique for modeling the flow of granular materials, and for comparing with experiments [24–26].

Particle Dynamics (PD), often referred to as the Discrete Element Method (DEM) – first developed by Cundall and Strack [27] in 1979 – has emerged as a successful simulation technique to study granular materials, giving insight into phenomena ranging from force transmission, agglomerate formation, flow of cohesionless materials, static packed beds, etc. In this simulation technique, an explicit time integration of Newton's equations of motion is performed for every particle and the trajectories of each particle are traced in order to determine the macroscopic flow of the granular bed. Modeling the contact properties between particles is the essential part of the PD methodology since it is used not only to model the flow of the granular bed but also to simulate processes that involve the transfer of heat [28–30]

and mass [31]. In this work, we employ experimental techniques and numerical simulations – using the Particle Dynamics technique (PD) and the Thermal Particle Dynamics method (TPD), which is an extension of the well-known Particle Dynamics (PD) technique– to study consolidation and flow of granular materials, with an emphasis on particle/bed material properties, force models, material properties, particle uniformity, and bed geometry, among other factors.

This document is organized as follows. Chapter 2 presents a general background of the relevant literature. An overview of the packing fraction in discrete modeling is described. In addition, previous work on thermal cycling in granular material, both experiments and simulations, is reported. Also included is a review of heat transfer in granular media. Finally, descriptions of the Particle Dynamics (PD) and Thermal Particle Dynamics (TPD) techniques are covered in this chapter. Next, Chapter 3 focuses on consolidation of granular materials under thermal cycling. Experimental and simulation studies are presented. Chapter 4, covers studies on the flow of granular materials. In particular, a DEM validation study using an annular shear cell is presented. Chapter 5 closes with a brief summary and discussion of the impact of this work and provides an outlook on future extensions.

2.0 BACKGROUND

Granular material refers to those solid particles that have a typical size greater than 10 μm. In dry grains, the forces that play an important role in the interaction between the particles are repulsive and frictional forces. When the grains are non-cohesive, any interstitial fluid such as air can be neglected in determining many of the flow and static properties of dense granular systems (although moving interstitial fluids can become important in instances with rapid fluid flow, such as fluidized beds) [6]. However, when the grains are wet, attractive forces are involved in addition to the repulsive and frictional forces. In this work, we shall focus only on non-cohesive (dry) granular material systems where the motion (if any) of interstitial fluids is slow enough that it may be neglected.

2.1 COMPACTION IN GRANULAR MATERIAL

2.1.1 Granular Packing

Discrete modeling and mathematical algorithms of granular packing have been widely studied [2, 32–44]. Many researchers investigate the most efficient way of packing granular materials, particularly spherical shapes. The highest possible packing fraction for mono-disperse spherical material is 74% with face center cubic (FCC) or hexagonal close packing (HCP) lattices. However, it is rare that granular systems are arranged in an ordered lattice. Hence, the packing fraction of a typical granular bed is much less than that of FCC or HCP structures. Song *et al.* [40] presented a theory for packing mono-disperse spheres and constructed a phase diagram that provides a unified view of the hard-sphere packing problem. Their re-

sults showed that 63.4% is the maximum density limit for random packing of hard spheres. Another approach to handle polydisperse material was explained by Farr and Groot [41], where they introduced a theory for the random close packing density of hard spheres of arbitrary size distribution. Connelly [45] gave an introduction to dense packings of disks in various spaces from the point of view of the theory of Tensegrity Structures. This has an application to jamming in granular materials as well as leading to a better understanding of jammed packings. A numerical study of the effect of air on the packing structure of fine particles was performed by Xiang [36]. Both continuum and discrete numerical models were used in the study and various forces were considered such as gravity, contact force, drag force, and van der Waals forces.

These algorithms and models usually involve many assumptions that come from geometrical consideration without taking into account the inter-particle interactions and forces. This deficiency was overcome by a novel technique called discrete element method (DEM) developed in 1979 by Cundall and Strack [27]. DEM is one of the most successful techniques used in discrete modeling for the simulation of particle assemblies. Unlike a continuum model, DEM can investigate the micro-mechanics of granular material and model different phenomena for their ability to describe the mechanics of the contacts between particles. The principle of DEM is to track the trajectory and rotation of each particle in a system to evaluate its position and orientation, and then to calculate the interactions between the particles and their neighbors [46]. In many models, the deformation is contact history dependent and contact mechanics models with different approaches have been proposed [2, 47–50]. Fu *et al.* [32] demonstrated a novel technique where a combination of X-ray microtomography (XMT) and discrete element method (DEM) were used to investigate randomly packed particles in model pharmaceutical powders. The XMT method enabled the particle size and shape distributions to be determined for mono-and polydisperse mixtures of spherical particles. Then, a DEM model for the powder packing was produced based on the individual particle information obtained from XMT. Makse *et al.* [38] employed a 3-D simulation study using DEM technique to investigate the random packings of compressible spherical grains under external confining stress. It was shown that the solid phase volume density depends on whether the grains interact via only normal forces (random close packings), where there is

no movement or spinning of the grains, or by a combination of normal and friction generated transverse forces (random loose packings). According to Makse *et al.*, the contact forces were localized along force chains which carry most of the applied stress.

2.1.2 Thermal Cycling

Granular materials are ubiquitous, impacting a variety of industrial processing in the pharmaceutical, polymer, chemical, and construction industries, but also having implications in natural phenomena such as the formation of lunar regolith, dunes and beach sand. Therefore, one of the most important parameters to consider for any application is the change that occurs to the packing fraction of those products. The packing fraction - named solid fraction in our work - varies between 57% to 64% for random spherical particles depending on the way the material is packed. Industries are interested in increasing the solid fraction of the grains in order to be cost effective during handling and processing. Powders that compact fast are expected to flow easily, while those that compact slowly, can effectively refuse to flow [51].

Lately, researchers have begun to look into different methods for changing the packing fraction of granular material by external excitation effects. The packing fraction increases when granular materials consolidate. Experiments and discrete modeling were used to study compaction in granular material via some perturbation effects such as tapping [52–54] and vibration [55–58], which induce the grains to rearrange and settle. Experimentally, Scott [59] showed that steel balls of equal size could be packed in two different ways, dense packing and loose packing [37]. For the loose packing, the steel balls were poured in the container without allowing for further rearrangements and it resulted in achieving 60% packing fraction. Whereas, in the dense packing, a packing fraction of 64% was obtained when the balls were gently shaken down into the packing container allowing for rearrangement contribution. It was shown in industry that temperature changes could cause damage to silo structures [60]. Carson *et al.* [61] indicated that during the investigation of a silo failure, calculations showed that the silo was under-designed and did not account for a phenomenon called thermal ratcheting by design engineers. As the silo walls expand during the day, the

material inside undergoes settling. However, when the silo walls contract at night when the temperature drops, the material resists the contraction, which in turn causes increased tensile stresses in the wall. The effect is repeated each day that the material sits at rest.

Recently, it has been found that cyclic variation of the temperature of a granular bed can cause the ostensibly static bed to consolidate (increase its packing fraction) over time due to thermo-mechanical coupling. Studies on thermal cycling whether experimental [62–66] or computational [67] are few. Chen *et al.* [62] demonstrated that the same results achieved by tapping or vibration methods can be obtained by thermal cycling. The experimental study showed that the thermal expansion of the particles could have a great effect on the consolidation of the granular media. Moreover, it was shown that the packing fraction of a granular bed could be increased in a very systematic and controllable way by simply raising and then lowering the temperature, without the input of any mechanical disturbance. It was observed that the change in the packing fraction was up to 2% in a bed of glass beads in a plastic cylinder with variable cycling temperature difference. According to Chen *et al.*, when a granular material is heated, both the grains and their container undergo thermal expansion, which in turn leads to settling due to the metastable (fragile) nature of the grains contact network. This settling does not reverse when the grains and their container are cooled to ambient temperature. Chen *et al.* explained that the primary reason for the changes in packing fraction is the difference between the thermal expansion of the grains and the container. It was found that the results are not affected by the height to which the containers are filled, the heating rate, or the time spent at the cycle temperature; but did change slightly ($< 20\%$) when the container diameter was changed by an order of magnitude.

Vargas *et al.* [67] reported results and analyses in a simulation study on the effects of thermal expansion on compaction by thermal cycling in a 3-D packed bed using thermal particle dynamics (TPD) technique – a modified discrete element simulation introduced by Vargas and McCarthy [30]. The simulation models the behavior of a polydisperse system of non-cohesive spheres (glass) bounded by a rigid wall and an open top. Vargas *et al.* argued that their simulation results, which didn't account for the wall thermal expansion, showed similar trends, although with smaller changes in packing, as the experimental results reported by Chen *et al.* . Vargas *et al.* claimed that the thermal expansion of the wall might

increase the degree of compaction attained yet it is not necessary since particle expansion and contraction alone is sufficient to achieve bed compaction.

Slotterback *et al.* [66] investigated, experimentally, the motion of particles close to jamming relative to their neighbors in granular material subject to a slow compaction by thermal cycling. Glass beads immersed in index matching oil in a cylinder were subjected to thermal cycling via a water bath. The internal structure and dynamics of a 3-D jammed granular system was observed using a laser sheet scanning tool and both the trajectories and Voronoi cells about each particle were determined for the particles rearrangement in this compaction process.

Divoux *et al.* [65] verified, in an experimental work, that temperature variations of even a few degrees in amplitude could induce the compaction of a granular pile and lead to an increase in the thermal properties of the system, such as thermal linear expansion coefficient and thermal conductivity. Thus, uncontrolled temperature variations can be responsible of part of the observed ageing of the physical properties of a granular material at rest. Measurements of the thermal linear expansion coefficient and the thermal conductivity of a granular pile were reported. The values of thermal properties increase as a result of the thermal cycling process of the granular pile. It was concluded that the difference between the thermal expansion coefficient of the beads and that of the container is probably not the primary cause of the compaction during the thermal cycling process.

2.2 HEAT TRANSFER IN GRANULAR MATERIALS

Heat transfer in particulate systems can be encountered in many engineering, scientific, and industrial applications. Hence, understanding the thermal properties of a system becomes a significant factor in the design and operation of these applications. In any medium, heat can be transfered via three major phenomena: conduction, convection, and radiation. Although radiation and convection contributions can be important, the conduction contribution usually has the most contribution in dense particulate systems when the solid conductivity is larger than that of the interstitial medium (which is true for most solid-gas systems) [68–70]. Hence,

the distribution of particle contacts and the resulting stress chains [2,3,6] play a significant role in the heat conduction problem. In our work, we deal essentially with static systems where the conduction contribution is the major one.

Research in the area of granular heat transfer presents many methods that are based on a continuous macroscopic description of the particle bed that generally gives good solutions for steady average temperature profiles within the material when detailed characterization of the microstructure is available [30, 71]. However, the simplest case of heat conduction through a solid phase presents challenges under transient conditions. The use of "effective" thermo-physical properties of the bulk material becomes essential to these methods. These can be determined either theoretically or experimentally, which could be troublesome in some cases. The study of effective thermal conductivity of packings of spheres, experimentally and numerically, has been investigated by many scholars [69, 72, 72–77]. Other heat transfer mechanisms are supposed to be largely dominated by solid phase conduction. This assumption indicates that the effective thermal conductivity depends on the geometry of the packing, the geometry of the contact, and the conductivity of the solid material [69].

Heat transfer in packed beds with interstitial fluid takes place via the following mechanism, neglecting the radiant contribution: thermal conduction through the solid, thermal conduction through the contact area between two particles, and thermal conduction through the fluid between the neighboring particles, if applicable. Heat transfer by inter-particle convection needs to be considered if there is a fluid flow involved [71]. In this work, as discussed previously, only the first two mechanisms of conduction, will be considered. Batchelor and OBrien [78] estimated this assumption to be valid as long as

$$\frac{k_s a}{k_f R} \gg 1 \tag{2.1}$$

where a is the contact radius, R is the particle radius of curvature, k_f denotes the fluid interstitial medium conductivity and k_s is the thermal conductivity of the solid granular material. This condition is approximately true for high conductivity ratios (k_s/k_f), and identically true for solid particles in a vacuum ($k_f \to 0$).

Based on the type of process and material variables, heat transfer between the heated surfaces and the particles and between the particles themselves is controlled by contact

conductance (H_c), which is defined as the ability of two touching materials to transmit heat across their mutual interface. In the contact conductance problem of conduction between two smooth particles under vacuum with small but finite area of contact, the resistance to heat transfer is assumed to be solely due to the constriction of the heat flow lines from one particle to another. Research in this area proposed approximate analytical solutions [78–82] for the contact conductance problem. All of these models predicted that the contact conductance varies with the imposed normal force as $H_c \propto {F_n}^{1/3}$.

Contact conductance theories were incorporated in the Discrete Element Method (DEM) to simulate many two-body thermal interactions. In fact, only a few studies incorporate the thermal effect into DEM models [28–30, 83]. In our work, as explained in Section 2.4, the model referred to as Thermal Particle Dynamics (TPD) solves simultaneously and for each time-step both the dynamic and thermal balances for the granular system. This novel technique makes it possible to study the heating mechanism that governs the transport of heat through a granular bed.

2.2.1 Thermoelastic Contact

Heat conduction plays a major role in thermoelastic contact. When heat is conducted across an interface between two dissimilar materials, the interaction between thermoelastic distortion, which affects the contact pressure distribution, and the existence of pressure-sensitive thermal contact resistance at the interface can cause the system to be unstable in the steady state [84, 85]. Barber *et al.* [86, 87] investigated the stability consideration in thermoelastic contact in a simple one-dimensional model of a rod conducting heat between rigid walls in which thermoelastic contact conditions give rise to non-uniqueness of solutions. A perturbation method is used to investigate the conditions for stability of the various steady state solutions discovered. The results show that when the steady state solution was unique, it was also stable, whereas when multiple solutions exist, they were alternately stable and unstable [88]. To illustrate, the criteria for stability and uniqueness are identical if the system only involves a single body and a rigid wall. In other words, steady state solutions are only unstable when they are non-unique.

Barber and Zhang extended the previous work to investigate the transient behavior and the stability of a system that consists of two different thermally conducting elastic rods in contact on their end faces [88]. The other ends of the rods are attached to rigid walls which are maintained at two different temperatures. A thermal resistance is assumed to exist at the interface between the rods and it is a function of the contact pressure or the gap. A perturbation method is used to study the stability of the system, and then a finite difference method is used to model and analyze the transient behavior. Unlike the one-dimensional case, Barber and Zhang found that the characteristic equation obtained involves the thermal diffusivities of the two materials as well as the steady state properties such as conductivity and thermal expansion coefficient. To illustrate, when both bodies (rods) are deformable, stability depends additionally on the thermal diffusivity ratio of the material. In the results, several qualitatively different stability patterns were obtained in the contact of the two rods, depending on the diffusivity ratios and the rod lengths. The numerical analysis demonstrates that under certain types of conditions an oscillatory behavior occurs in which the temperature and the contact pressure varies with time.

Stability analysis for thermoelastic contact has been conducted by linear perturbation methods for one dimensional [86,87] and simple two dimensional [84] geometries, but analytical solutions become very complicated for finite geometries. Yeo *et al.* [85] therefore proposed a method in which finite element analysis is used to reduce the stability problem to an eigenvalue problem, where a time-independent set of homogeneous equations are obtained. The results show good agreement with previous analytical investigations and illustrate the use of this method in the simple two rod system of Barber and Zhang [88].

When two elastic bodies at different temperatures (i.e., hot and cold) are pressed together, there will be generally some resistance to heat flow across the interface [84]. This resistance is a function of the local contact pressure, which is itself influenced by the thermal distortion, and hence by the temperature fields in the bodies. As a result, the right way to describe this function is by coupling the heat conduction and elasticity solutions (thermomechanical coupling) through the boundary conditions. Zhang [84] *et al.* investigated the influence of material properties on the stability criterion of two dissimilar materials. Based on certain material combinations, the results obtained can be classified into two types of

stability behavior. In the first, stability behavior is similar to the one-material systems explained earlier by Barber [86], yet instability only occurs when the heat flows into the material with higher distortivity. In other words, instability is only possible for one direction of heat flow. The second type of instability can occur for either direction of heat flow (i.e., into the material with higher and lower distortivity). For the less distortive material case, the steady state solution is unique and the stability boundaries are characterized by the oscillatory growth of a pressure perturbation.

The thermo-mechanical coupling associated with thermal boundary conditions that depends on contact pressure, or gap, leads to an extraordinarily rich variety of physical phenomena, none of which can occur in the absence of coupling [89]. Many of these phenomena still need further investigation and more research for better understanding.

2.3 PARTICLE DYNAMICS MODELING

Discrete modeling, particularly Particle Dynamics (PD) – known as the Discrete Element Method (DEM), of granular materials has been widely accepted as an efficient and reliable numerical technique in studying the mechanical behavior of granular materials [49, 90–98]. This technique can work as an alternative or supplement to experimental studies of granular flows [99–103]. This method was developed by Cundall and Strack in 1979 [27] with their first application to study the dynamic behavior of granular material. Unlike continuum techniques, the advantage of the particle dynamics method is that it simulates effects at the particle level due to its first-principle construct. In this section, we present background relevant to particle dynamics including the general algorithm of DEM, followed by the types of force models used for this method.

2.3.1 Algorithm

Depending on the bulk density and characteristics of the flow to be modeled, two types of particles dynamics methods of calculating the trajectories are most common: hard-sphere

model and soft-sphere model. Typically, the hard-sphere model is used for rapid, not-so-dense granular flows where a sequence of instantaneous collisions is processed and the typical duration of a collision is much shorter than the mean time between successive collisions. The particles are rarely in mechanical contact with more than one other particle. For the hard-sphere model, particles do not bear any deformation. Hence, the forces between particles are not explicitly considered in the hard-sphere model. This indicates that this model is most useful for rapid flows of granular material. Tracking the next collision is the main focus of hard-sphere modeling and the particle trajectories are obtained from a set of collision rules, where no integration is required. These collision rules relate the post-collision velocities as a function of pre-collision velocities. In this model, the conservation of linear and angular momentum for each collision is applied sequentially [104]. The collisions are typically inelastic with a coefficient of restitution for the normal impact and a coefficient of friction for the tangential impact [105].

However, the work presented in this document uses the soft-sphere approach in particle dynamics modeling (or DEM). This approach is used for slow, dense granular flow, which is the nature of the systems that we simulate in this work. Here, particles undergo an enduring contact and multi-particle collisions. In this model, deformation of particles can occur, hence, forces arise due to this deformation. Particle trajectories are obtained via explicit solution of Newton's equations of motion for every particle at discrete time intervals as the simulation marches forward in time.

In DEM, we capture the macroscopic behavior of a particulate system where every particle is tracked individually to determine its trajectories within the mass. The global flow of the granular material is then determined via simultaneous integration of the interaction forces between individual pairs of particles in contact. The individual particle trajectories are governed by Newton's equations of motion [27]. The equations that describe the particle motion are:
Linear Motion:

$$m_p \frac{d\vec{v}_p}{dt} = -m_p \vec{g} + \vec{F}_n + \vec{F}_t \tag{2.2}$$

Angular Motion:

$$I_p \frac{d\vec{\omega}_p}{dt} = \vec{F}_t \times \vec{R} \tag{2.3}$$

where $\vec{F}_n$ and $\vec{F}_t$ are, respectively, the normal and tangential inter-particle forces acting on the particle (See Figure 1). In Figure 1, when two particles are under loading, a very small overlap results, where the dimensionless strain is less than 0.1% of the particle radius. The relevant distance is the one that shows the overlap perpendicular to the particles contacting plane. The mass of the particle is denoted as m_p, $\vec{v}_p$ and I_p are the particle velocity and moment of inertia, respectively, ω_p is the angular velocity, $\vec{R}$ is the radius, and t is the time. For symmetrical spherical particles, the normal force changes the translational motion of the particles and the tangential force changes both the translational and rotational motion of the particles. Both components of the force are functions of the relative positions of the particles $(\vec{R}_i - \vec{R}_j)$ and of the relative velocity $(\vec{v}_i - \vec{v}_j)$. As discussed in Section 2.3.2, the forces on the particles, aside from gravity, are determined via contact mechanics considerations [106]. The ability to determine the contact forces between particles when they suffer minute deformations (overlap) is the key feature of the PD technique. In their simplest form, these relations include normal, Hertzian, repulsive, and some approximation of tangential friction (due to Mindlin [107]).

In our algorithm, the integration scheme and time-step are used such that all forces acting on each particle are determined from the positions of particles, and the net linear and angular acceleration of each particle are obtained. The positions and orientations at the end of the next time-step are then evaluated explicitly using one type of finite-difference method initially adopted by Verlet and attributed to Störmer [108].

$$\dot{x}_{t+\frac{1}{2}\Delta t} = \dot{x}_t + \frac{1}{2}\ddot{x}_t \Delta t \tag{2.4}$$

$$x_{t+\Delta t} = x_t + \frac{1}{2}(\dot{x}_t + \dot{x}_{t+\Delta t})\Delta t \tag{2.5}$$

The particle positions are determined at certain time-steps. Constant or linearly varying conditions are assumed over the time interval, hence, the time-step Δt must be sufficiently

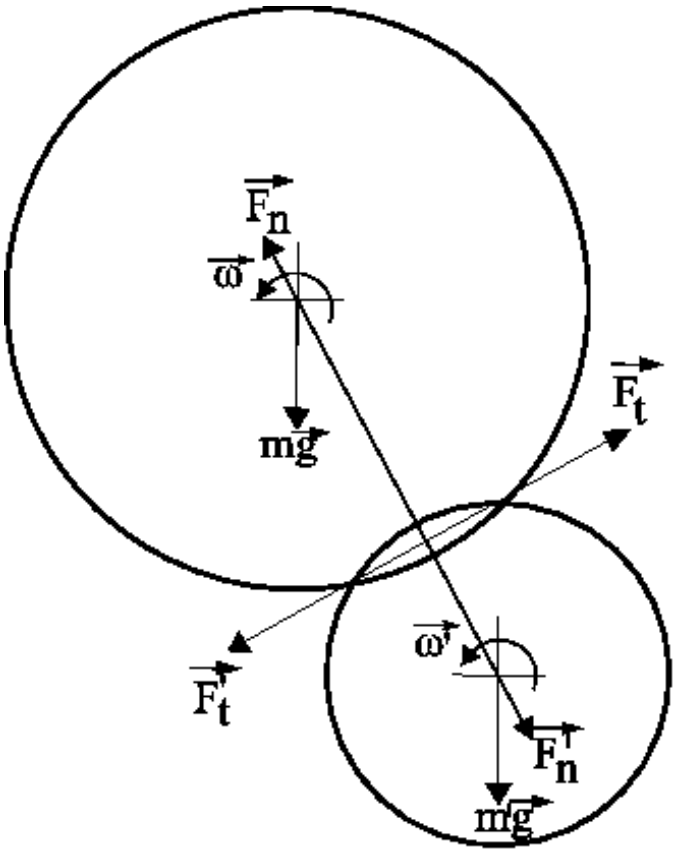

Figure 1: Schematic illustration of the forces between two particles in contact in PD

small such that any disturbance (in this case a displacement-induced stress on a particle) does not propagate further than that particle's immediate neighbors within one time-step, allowing for more accuracy. If the time-step is too small, the computer run time will be unnecessarily long and rounding errors can propagate over the time-steps causing errors. If the time-step is chosen to be too large, computational errors become significant and inaccurate results occur. In addition, the model could become unstable since it may lead to unrealistic overlap and large accelerations. Generally, the proper selection of the time-step is met by choosing a time-step that is smaller than R/λ, where R is the particle radius and λ represents the relevant disturbance wave speed (i.e., dilatational, distortional, and Rayleigh waves [91]). Under these conditions, the method becomes explicit, and therefore at any time increment the resultant forces on any particle are determined exclusively by its interaction with the closest neighbors in contact. Thornton and Randall [91] suggest that the time-step be chosen to correspond with Rayleigh wave speed so that

$$\Delta t = \frac{\pi R}{\alpha_o}\sqrt{\frac{\rho}{G}} \tag{2.6}$$

where R is the particle radius, α_o is a constant (taken to be $0.1631\sigma + 0.8766$ in our case), ρ is the density of the particle and G is the shear modulus, and σ is the Poisson ratio of the particle. For safety, we have used one quarter of the time-step value given by Equation 2.6, which resulted in a time-step $\Delta t \approx 10^{-6}$ s.

For our DEM simulations, the values of the coordinates $\vec{r}_p$(t=0), the velocities $\vec{v}_p$(t=0) and angular velocities $\vec{\omega}_p$(t=0) should be specified for $p = 1, ..., N$, where N is the total number of particles in the system. A typical initial condition for our simulations is accomplished by allowing a bed of particles arranged in a randomly perturbed lattice to settle under the action of gravity using a traditional isothermal PD simulation (particle mechanics only) so that a relaxed state is obtained. Initial positioning of the particles in the lattice sites should avoid large overlaps as this would generate very large spurious forces, which are unrealistic, and the simulation would not proceed further.

2.3.2 Force Models

In a granular flow, the particles experience forces and torques due to interparticle interactions (e.g., collisions, contacts, or cohesive interactions) as well as interactions between the system and the particles (e.g., gravitational forces). In general, the collisional force models range from pragmatic linear "spring and dashpot" techniques to rigorously derived contact mechanics-inspired routines [106], and in this work we examine both ends of the spectrum. The accuracy of a soft particle simulation is almost always dependent on the choice of contact mechanics, which may act in the direction normal to the contact surface (normal force) or tangential to the contact surface (tangential or friction force). In 1882, Hertz [109] was the first to attempt to study the mechanics of elastic contacts between particles. Hertz predicted the static normal compression between the two bodies as a function of the mechanical properties of the materials and assumed that there is no energy loss due to elastic wave propagation. Hence, the coefficient of restitution was set to unity. In order to overcome this shortcoming, several studies [27, 94, 103, 110–112] were proposed by many researchers. Cundall and Strack [27] first formulated their force model accounting for the contact mechanics through the use of a spring, a dash-pot and a slider configuration, as shown in Figure 2. Walton and Braun [94] presented a normal contact model which was able to mimic elasto-plastic and plastic collisions giving realistic coefficients of restitution when compared with experiments. Oden and Martins [111, 113] introduced a more computationally complex normal force model giving restitution coefficients in good agreement with experiments.

In addition to normal forces, at oblique collision, friction (tangential) forces were also included. For friction force models describing the tangential loads between particles, Mindlin and Deresiewicz described the processes of microslip and sliding that occur due to the normal and tangential forces [107,114]. Mindlin and Deresiewicz model was simplified by Walton and Braun [94], where two history dependent terms were included. The deformation or energy dissipation is contact history dependent and different studies on frictional contact mechanics models have been proposed [27, 48, 91, 103]. A thorough description of the interaction laws can be found elsewhere [105, 115–118]; therefore only the models employed will be reviewed here.

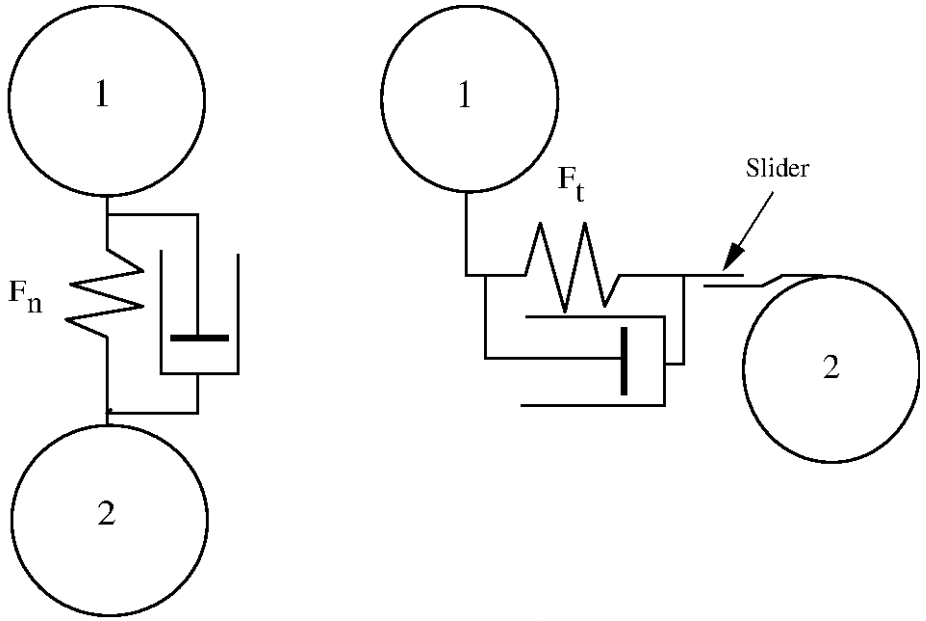

Figure 2: Schematic illustration of the models of contact forces acting on particle 1 from contacting particle 2 through use of a spring (left), a dash-pot and a slider configuration.

2.3.2.1 Normal Forces Two approaches are used to model normal forces in this work: a Hertzian spring-dashpot model and an elasto-plastic material model [119, 120]. In both cases, the deformation of the particles is mimicked via a computational "overlap" (see Figure 3) so that $\alpha = (R_1 + R_2) - S_{12}$, where R_i is the particle radius and S_{12} is the distance between particle centers of particle 1 and 2. Again, in both cases, during the initial stages of loading, the normal force, F_n, is purely elastic and is given by

$$F_n = k_n \alpha^{3/2}, \tag{2.7}$$

where k_n is the normal force constant from the Hertz theory [106]. This constant is a function of the particle radii, R_i, and elastic properties (Young's modulus, E_i, and Poisson ratio, σ_i):

$$k_n = \frac{4}{3} E^* \sqrt{R^*}, \tag{2.8}$$

where the effective particle radius, R^*, and the effective Young's modulus, E^*, are given by

$$\frac{1}{E^*} = \frac{1 - \sigma_1^2}{E_1} + \frac{1 - \sigma_2^2}{E_2} \tag{2.9}$$

$$\frac{1}{R^*} = \frac{1}{R_1} + \frac{1}{R_2} \tag{2.10}$$

respectively. At this point the two models differ in their model of energy dissipation. In the case of the spring-dashpot model, a damping term that is proportional to the relative normal velocity between particles is linearly added to the repulsive force from Equation 2.7. While the damping term can take several forms, we choose the formulation suggested by Oden and Martins [111] due to the fact that it qualitatively reproduces the experimentally observed dependence of the coefficient of restitution on impact velocity for many engineering materials (i.e., a power law decrease). Combining the repulsive force and this dissipation term yields what we will refer to as our *spring-dashpot* model, which is given as

$$F_n = k_n \alpha^{3/2} - \beta \alpha \dot{\alpha}, \tag{2.11}$$

where $\dot{\alpha}$ is the relative normal velocity of the particles, and β is a damping parameter that is assumed to be adjustable as discussed below.

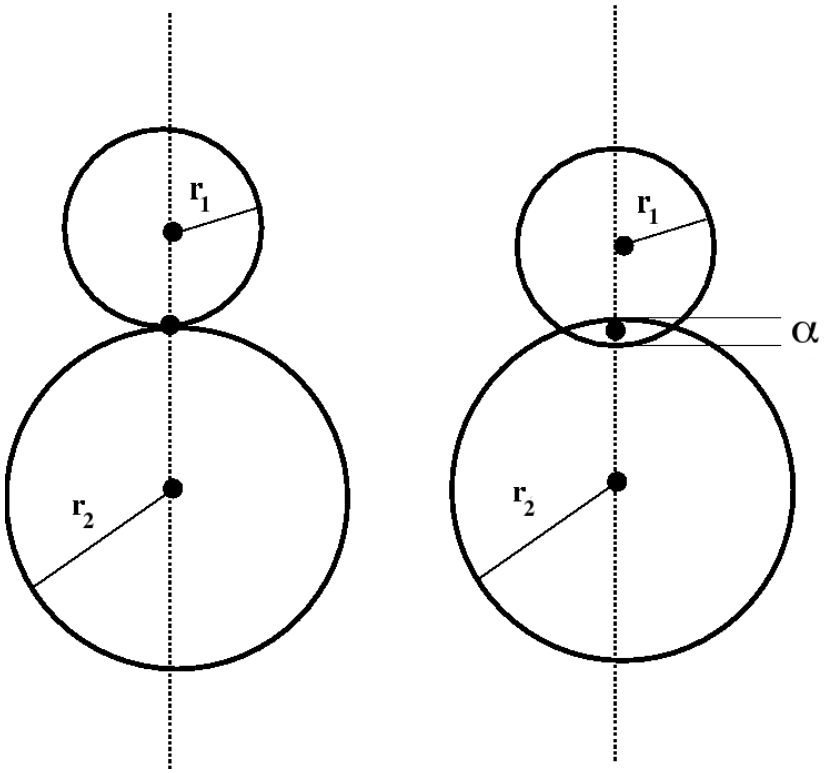

Figure 3: Schematic illustration of the contact point between two particles showing the overlap α

In contrast, in our *elasto-plastic* model, dissipation is assumed to arise from the plastic deformation of the center of the contact spot. In this model, once the normal force exceeds a yield force, F_y, further loading is given by the linear expression

$$F_n = F_y + k_y(\alpha - \alpha_y). \tag{2.12}$$

In this expression, k_y is the plastic stiffness which is related to the yield force by $k_y = (3/2)(F_y/\alpha_y)$, and α_y is the deformation at the point of yield (i.e., where both Equation 2.7 and 2.12 give $F_n = F_y$). Unloading prior to exceeding the yield limit is purely elastic, while unloading after the yield limit is given by

$$F_n = F_{max} - k_n\sqrt{\bar{R}}(\alpha_{max} - \alpha)^{3/2}, \tag{2.13}$$

where F_{max} and α_{max} are the maximum force and deformation, respectively and $\bar{R}$ is dimensionless and given by the ratio of the new contact curvature due to plastic deformation, R_p, to R^*,

$$\bar{R} = \frac{R_p}{R^*} = \frac{F_y}{F_{max}}\left(\frac{2F_{max} + F_y}{3F_y}\right)^{3/2}. \tag{2.14}$$

Reloading after initial yield follows the same path as Equation 2.13 up to the maximum prior force, at which point the contact continues to deform plastically (Eqn. 2.12). While the yield force, F_y, can be loosely related to the yield stress of the bulk material, in this work, we treat it in the same manner as β from the spring-dashpot model.

2.3.2.2 Tangential Forces Tangential forces arise under oblique collisions between particles. Many factors can have an effect on the nature of the tangential forces developed between bodies in contact such as history of the contact and the response of the interface to normal forces [111]. Therefore, it is important to include these type of forces in DEM simulations. For typical particles, we can apply the Coulomb limit between friction and the normal force (see Figure 4) once macroscopic sliding occurs as follows

$$F_t \leq \mu_f F_n \tag{2.15}$$

where F_t is the tangential force, F_n is the normal force, and μ_f is the friction coefficient. However, modeling the onset of sliding is more complicated [107]. Mindlin [107] made a clear distinction between macroscopic sliding and microslip where only portions of the contact surface are in motion relative to each other. Mindlin's model requires the complete history of the loading and unloading for each particle. Different particle dynamics models [27,47,94, 103,112] approximate Mindlin's work to varying degrees. Modeling the tangential forces that arise from oblique particle impacts has elicited a considerably wider range of force models than those of normal interactions.

For the purposes of this document, we will refrain from examining models that elicit "creep" (i.e., models whose tangential force is based on the tangential *velocity*) [103]. In one non-creep frictional model proposed by Tsuji [103], microslip is ignored and no history dependent terms are retained. Instead, we will consider both the simplest [27] and most comprehensive [91] of the "history dependent" friction models, which are very similar to the tangential force model proposed by Walton and Braun [94,121]. That is, for each time-step, the new tangential force acting at a particle-particle contact, F_t, is updated by

$$F_t = F_{t_o} - k_t \Delta s, \tag{2.16}$$

where F_{t_o} is the old tangential force and $k_t \Delta s$ is the incremental change in the tangential force during the present time-step due to relative particle motion; i.e., Δs is the tangential displacement during the present time-step. This displacement is calculated from the component of velocity tangent to the contact surface, v_t (i.e., $\Delta s = v_t \Delta t$ where Δt is the time-step). In the simpler of our two friction models, we will assume that the tangential stiffness, k_t, is a constant, which we will call k_{t_o}. Also, for the linear model, no energy is dissipated prior to macroscopic sliding, as particles do in reality during loading and unloading, (Figure 5) provided the Coulomb limit is not exceeded during the contact.

In this model, we must impose a discontinuity in order to limit the tangential force to the Coulomb's Law limit given by Equation 2.15. We will refer to this model as the *linear* model. In the more involved scenario (referred to as the *nonlinear* model), two history dependent terms are included. The model allows for microslip so that it dissipates energy prior to macroscopic sliding as shown in Figure 5. In order to mimic an annular region of microslip

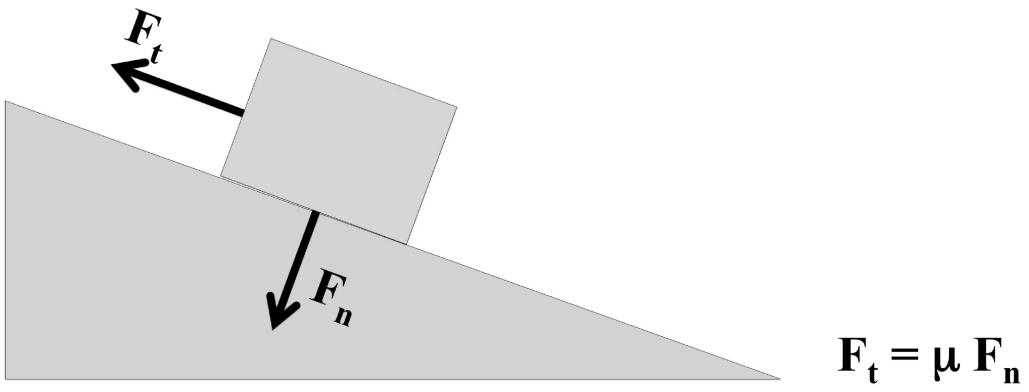

Figure 4: Schematic illustration of the relationship between normal and tangential forces in Coulomb relation.

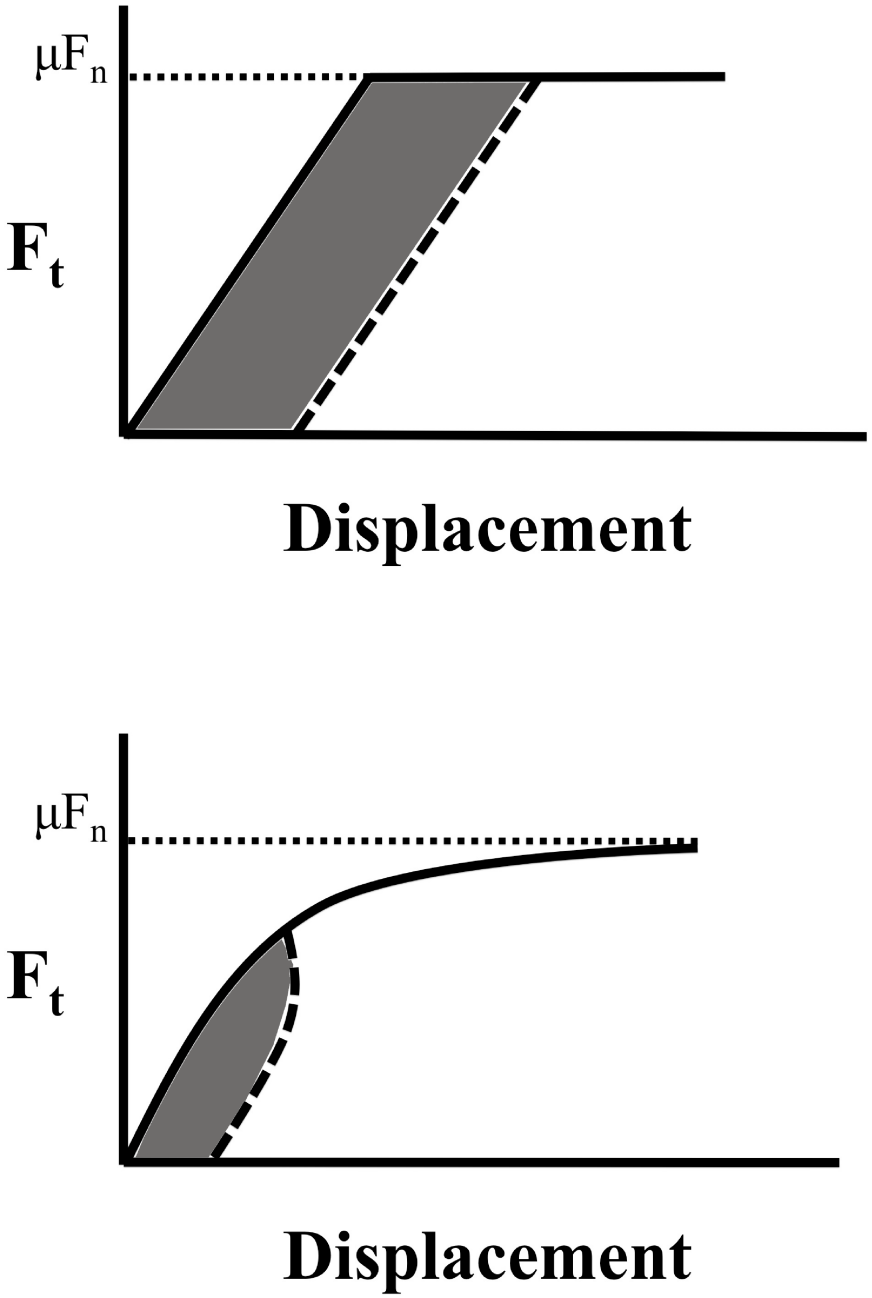

Figure 5: Schematic illustration of the energy dissipation (area under the curve) during the loading (solid-line) and unloading (dotted-line) process for the two different friction models. (Top) Linear model: No energy dissipation prior to macroscopic sliding. (Bottom) Nonlinear model: Energy dissipates prior to macroscopic sliding.

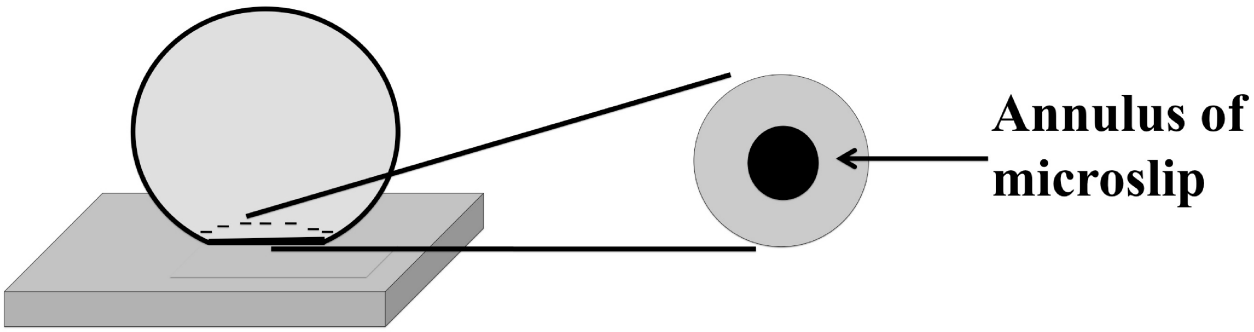

Figure 6: Schematic illustration showing the annular region at the edge of the contact undergoing microslip prior to macroscopic sliding.

at the edge of the contact (see Figure 6) as well as smoothly satisfy the Amonton's/Coulomb's Law limit, the frictional stiffness, k_t, is given by the nonlinear expressions obtained following the procedure given in [91].

$$k_t = k_{t_o}\theta \pm \mu\frac{(1-\theta)}{\Delta s}\Delta F_n \tag{2.17}$$

with

$$\begin{aligned}\theta_L &= \left[1 - \tfrac{T+\mu\Delta F_n}{\mu F_n}\right]^{\frac{1}{3}} \\ \theta_U &= \left[1 - \tfrac{T^*-T+2\mu\Delta F_n}{\mu F_n}\right]^{\frac{1}{3}} \\ \theta_R &= \left[1 - \tfrac{T-T^{**}+\mu\Delta F_n}{\mu F_n}\right]^{\frac{1}{3}}.\end{aligned} \tag{2.18}$$

The subscripts L, U and R in equation 2.18 correspond to loading, unloading and reloading, respectively. The negative sign in 2.17 is only used for the unloading stage. The load reversal points T^* and T^{**} need to be continuously updated as $T^* = T^* + \mu F_n$ and $T^{**} = T^{**} + \mu F_n$ to account for the effect of varying normal force. This *nonlinear* friction force will be denoted with an $\mathbf{N}$. In both the linear and nonlinear case, the (initial/constant) tangential stiffness, k_{t_o}, can be related to the normal stiffness k_n by

$$k_{t_o} = \frac{k_n(1-\sigma)}{1-\sigma/2}. \tag{2.19}$$

Note that the rates of change of displacement with loading should be similar for tangential versus normal interaction, so that their ratio [106] is given as

$$\frac{ds/dF_t}{d\alpha/dF_n} = \frac{1-\sigma/2}{1-\sigma}. \tag{2.20}$$

2.4 THERMAL PARTICLE DYNAMICS

The Thermal Particle Dynamics (TPD) simulation technique, which is based upon a traditional PD technique [27], allows the determination of both mechanical and transport properties of granular systems under static and/or dynamic conditions. The key feature of TPD is that by incorporating contact conductance theories many simultaneous two-body interactions may be used to model heat transfer in a system composed of many particles. In analogy with PD, this description requires that the time-step be chosen such that any disturbance (in this case a change in a particle's temperature) does not propagate further than that particle's immediate neighbors within one time-step. While for this work we consider particles in lasting contact, this criterion is also satisfied in the majority of collision-dominated flows, although the amount of heat transferred between colliding particles under these conditions can be small [122].

Contact conductance refers to the ability of two materials in contact to transmit heat across their mutual interface. It is the key ingredient added to PD in order to form TPD. In terms of the contact conductance to heat transfer, the heat flow, Q, between the two particles (Figure 7) is given by

$$Q_c = H_c \Delta T_{ij} \tag{2.21}$$

where ΔT_{ij} is the temperature difference (driving force) between the mid-planes of the spheres, and H_c is the contact conductance. Approximate analytical solutions have been proposed independently by Yovanovich [79], Holm [81], and Batchelor and O'Brien [78]. All of these models predict that the conductance from one particle center-line to the other is given by

$$H_c = 2k_s a \tag{2.22}$$

where k_s is the conductivity of the solid, and a is the radius of the contact point. The contact conductance is coupled to the contact mechanics through the contact radius and the material properties. For smooth-elastic spheres in a vacuum, H_c depends on the contact

radius which may be obtained from Hertz's elastic contact theory so that Equation 2.22 can be expressed as

$$H_c = 2k_s \left[\frac{3F_n R^*}{4E^*} \right]^{1/3} \tag{2.23}$$

where E^* is the effective Young's modulus for the two particles, and R^* is the geometric mean of the particle radii.

In the same way that contact mechanics is well understood for two-body interaction [106] to capture the mechanical properties of the particles in PD, contact conductance models are also well established [123], [124]. Therefore, it is desired to make a direct analogy with PD's use of contact mechanics in the context of heat transfer. Here, the disturbance is a temperature change instead of a displacement-induced stress.

To incorporate the concept of conductance to model the transfer of heat between particles, consider particles i and j that are in contact (Figure 8) and whose temperatures far from the contact points are T_i and T_j, receptively. The amount of heat transported across their mutual boundaries per unit time is given by

$$Q_{ij} = H_c \left(T_j - T_i \right) \tag{2.24}$$

The evolution of the temperature of particle i, for pair-wise contacts, may be given in some average sense as

$$\frac{dT_i}{dt} = \frac{Q_i}{\rho_i c_i V_i} \tag{2.25}$$

where Q_i is the total amount of heat transported to particle i from its neighbor (particle j), and $\rho_i c_i V_i$ is the particle's "thermal capacity". Scale-up from this equation to multi-body contacts (for use in TPD Simulations) is straight-forward, but requires two caveats. The first is that each i-j particle contact "sees" the same temperature for particle i such that the temperature does not vary significantly from one contact point to another and each heat interaction may be calculated from Equation 2.24.

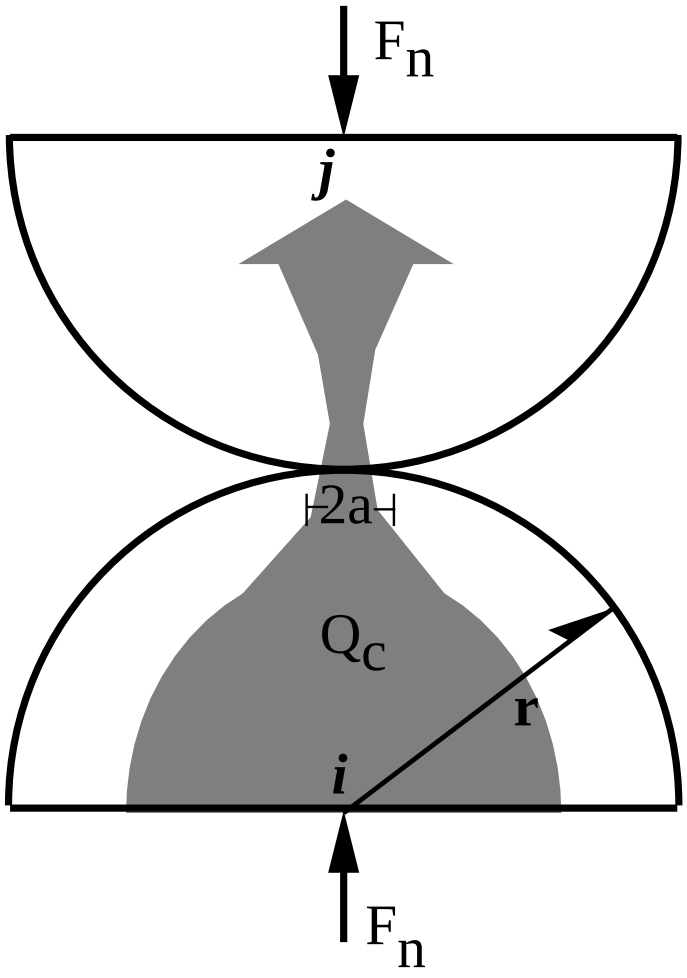

Figure 7: Heat Conduction between two smooth-elastic spheres

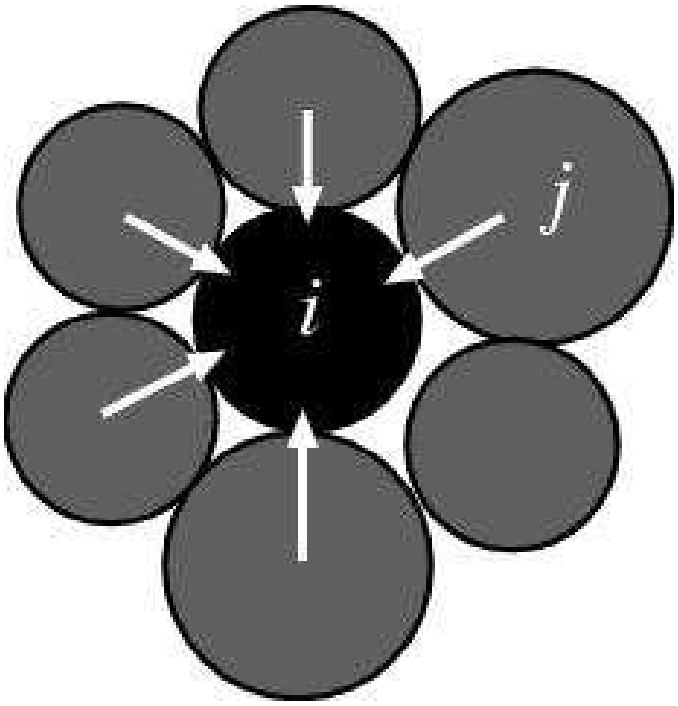

Figure 8: Thermal interaction between particle i and its neighbor j in TPD

Under these conditions it is reasonable to assume that the total heat transfer between particle i and all (N) of its neighbors, j, can be expressed as

$$Q_i = \sum_{j=1}^{N} Q_{ij}. \tag{2.26}$$

While approximating the transient heat flow by the steady-state value is not strictly correct – incorporating a contact "capacitance" is possible to make this formally true [125] – it is conceptually simple and is found to be accurate over the time-scales examined here. Moreover, justifying the assertion that the total heat flow may be obtained by summing individual heat flows requires that the resistance to heat transfer inside a particle is significantly smaller than the resistance between interacting particles. In other words, the Biot number of the particle heating problem for two elastic spheres in contact should be very small and can be expressed as

$$Bi = \frac{H_c}{k_s A/R} = \frac{H_c}{k_s \pi R} = \frac{2}{\pi}\left(\frac{a}{R}\right) \ll 1 \tag{2.27}$$

where Bi is known as the Biot number, and A is the cross sectional area of the particle.

To take into account the effect of the thermal expansion, the change in the radius of the particles due to expansion is incorporated into the simulation as

$$R = R_o + \beta \Delta T, \tag{2.28}$$

where R_o is the initial radius of the particles at the reference temperature, β is the thermal expansion coefficient of the solid particle material, R is the current radius, and ΔT is the temperature rise relative to the reference temperature. A similar approach has been previously applied by Lu *et al.* [126].

2.5 FLOW OF GRANULAR MATERIALS

Granular material flows play a significant role in many of our industries such as pharmaceuticals, polymers, constructions, and food processing. The understanding of granular flows of

materials that are subjected to shearing is the key for many applications to predict natural phenomena such as avalanches, landslides, and soil erosion [13]. In this section, we will introduce the general characteristics of granular flows in 2.5.1. Then, a review of experimental studies of granular flows will be given in Section 2.5.2 followed by granular computational studies, in Section 2.5.3.

2.5.1 General Characteristics of Granular Flows

Campbell [7] gives a good overview of the general field of granular flows, and includes material on the basic transport processes governing such flows, the contact mechanics important in interparticle contacts, and the limiting regimes which have been used to describe granular flow behavior under certain ranges of conditions. A granular solid can be defined as a collection of discrete solid particles. If the particles are large and heavy, generally the effect of the interstitial fluid which fills the spaces between the particles on the flow properties can be neglected [7]. While cohesive effects between particles may be important for some applications, they are generally less important for large particles where the ratio of surface area to volume is small [7].

Campbell notes that there are two mechanisms by which force is internally transmitted within a granular flow. There are contact stresses, which arise from interparticle contacts as well as streaming stresses which result from motion of a particle relative to the bulk material. Generally speaking, streaming stresses are only important at small concentrations for dense suspensions of granular materials; where the volume fraction of solids may be more than 50%; the contact stresses and the interparticle collisions which give rise to them will dominate [7].

The methods which have been used to describe the normal and tangential forces between particles is described by Campbell [7, 20]. He reviews the elastic [109] and inelastic [94, 127, 128] models which have been used to represent the normal forces as well as discussing the tangential forces which arise from frictional forces resulting from particle contact which can eventually cause the particles to slide or slip relative to one another.

In 1773, granular flow modeling began with the work performed by Coulomb [129] who first described the yielding of granular materials as a frictional process. Campbell [7] traces the history of the development of models for granular flows which date to the quasistatic models which were developed for slow granular flows and used techniques derived from plasticity theory. He notes extension of these plasticity-derived techniques to the study of granular flows has had some success in predicting flows from hoppers, where the flow can be assumed to be always yielding (see [130–132]).

In addition, Campbell discusses the approaches used to model the behavior of rapid granular flows under conditions where particle collisions dominate [7]. He notes the pioneering work by Bagnold [18], who was the first to attempt to develop a granular material from the point of view of individual particles. He notes that Bagnolds concept of the picture of the individual granules moving in a shear flow invited comparison to the motion of molecules in the kinetic theory of gases, which led to the concept of the granular temperature, first formulated by Ogawa [133]. The models for rapid granular flows [96], where granules interact by instantaneous collisions and transport rates are governed by the granular temperature.

Campbell [7] concludes by proposing that the flow regime for granular flows can be more usefully divided into the Elastic and Inertial regimes, which can be shown to describe the transition between the quasistatic and rapid flow regimes. He closes with a number of lessons or precepts which are recommended to researchers in the field as a guide for model development or data interoperation: rigid sphere models are inapplicable to dense systems, particle surface friction is essential to modeling dense systems, dense flows are not "frictional", and all important granular flows are dense.

Experimental and computational studies using different devices have provided valuable knowledge about the flow characteristics due to shear rate, boundary conditions, material properties, and solid concentrations [134]. Shearing flows, using annular shear cells and other shearing devices, have been intensively explored experimentally [135–139] and computationally [20, 96, 140–142] by many researchers, where computer simulations have shown to be a powerful tool to investigate granular flow. These studies of granular shear flows will be reported in the following sections.

2.5.2 Experimental Studies of Granular Flows

Granular flows are prevalent in natural and industrial flows and understanding their behavior and flow characteristics is of considerable importance. Because of their non-linear characteristics, and the general challenges in characterizing and describing multiphase granular flows, it has been difficult to develop models for and to simulate their behavior. Experimental studies have frequently been employed to develop a better understanding of their behavior and to both guide and develop theoretical and computational models for them.

For granular flows, many industrial processes and applications involve heat transfer either to or from the granular materials. Wang and Campbell [135] carried out a heat transport study to experimentally measure the apparent thermal conductivity and the apparent viscosity of a dense dry particulate material as it undergoes shear in an annular shear cell device. In this study, it was experimentally found that in relatively rapid flows, the bulk shear motion improves the internal transport of both heat and momentum. In addition, the results show that both transport coefficients (the apparent thermal conductivity and the apparent viscosity) increase linearly with the imposed shear rate, suggesting that similar internal mechanisms drive both transport processes (i.e., heat and momentum). Momentum is transported both by particle collisions and by random motion of the particles. However, because heat transfer is a slow process, little heat can be conducted during short contact times. Consequently, Wang and Campbell found that for large particle concentrations, there is almost no shear-induced enhancement of the effective thermal conductivity due to the limited mobility of the particles which is in turn hinders the particles's self-diffusivity and ultimately the mixing process.

The effect of shearing on the convective heat transfer coefficients in a vertical granular flows was experimentally investigated in a channel by Natarajan and Hunt [136]. Experiments were performed with two types of wall conditions, a smooth wall condition to generate uniform plug flows and a rough wall condition to generate nonuniform sheared flow, in order to examine the influence of boundaries on the shear rate, medium density, and particle agitation. In addition, velocity fields were measured using image processing techniques. The results for both the shear and plug flows showed that at lower flow rates, the values of the

heat transfer coefficients were higher for the sheared flows for comparable values of flow velocity near the wall. On the other hand, the dilation close to the wall became a dominant factor at higher flow rates, and reduced the bulk conductivity significantly. In short, the medium density adjacent to the wall played a critical role in determining the overall heat transfer.

Measurements of the macroscopic flow variables such as velocity and granular temperature profiles can be a complicating factor when describing granular flows. However, there have been notable advances in non-invasive experimental methods for measuring the macroscopic flow parameters. A phenomenological study of a batch mixer using a positron camera was reported by Broadbent *et al.* [9]. In this study, particulate motion within a Lödige mixer has been analyzed using a refinement of the nuclear imaging technique, positron emission tomography. The authors demonstrated the capability of the positron camera for examining powder mixing, where the bulk flow patterns and segregation behavior can be seen. The positron camera can provide a reliable information of the detailed flow behavior of the mixer by determining not only axial, radial and angular locations but also the axial, radial and angular (tangential) velocity distributions.

Nakagawa *et al.* [11] reported non-invasive measurements of granular flows by magnetic resonance imaging (MRI). In this technique, MRI was used to non-invasively measure velocity and concentration profiles of flowing mustard seeds in a partially filled, steadily rotating, long, horizontal cylinder, commonly referred to as a kiln or a drum. The technique was first tested to confirm its validity by performing a rigid body rotation of a cylinder filled with granular material. The results show a uniform radial concentration profiles under certain rotation rates which assure that the method yields accurate concentration profiles. Furthermore, the results of the spatial linearity of the velocity profiles as well as the linearity of the slopes with the rotation rates demonstrate the validity of this technique.

In another technique explored by Nikitidis *et al.* [12], size segregation by self-diffusion during gas-phase flow of slow-shearing (coarse) binary granular mixture flows is quantified using a novel dual energy gamma-ray photon technique. This technique is capable of producing solids fraction profiles for each of the individual components of a binary mixture in addition to the voidage profiles. Also, the self-diffusion velocities and the diffusion co-

efficients of coarse and fine particles in the mixture are calculated based on a statistical mechanical analysis of local random drift during the flow. These calculations are compared with the theoretical predictions of self-diffusion coefficients based on the kinetic theory, which assumes random collisions between inelastic particles.

Digital particle tracking velocimetry (DPTV), the technique used in this work, employs high speed video cameras that are used to capture a series of images of colliding particles. This approach offers the ability to extract positions of individual particles in either Cartesian or cylindrical coordinate frames. The method requires sophisticated analysis techniques to automate the process of extracting the particle centroid location and movement from frame to frame from the large set of raw data contained within the hundreds or thousands of frames of images of colliding particles. Once the particle centroids have been identified in consecutive frames, their velocities can then be computed and this information can be used to resolve granular flow properties such as velocity, solid fraction, granular temperature, and slip both spatially and temporally. Veje *et al.* [14] and Mueth *et al.* [19] both used DPTV type techniques in their studies of granular flows while Xu *et al.* [143] commented on possible errors that could result from improperly conducted DPTV measurements, including the effects of insufficient frame rate, insufficient sampling, and finite pixel size. In their application of the DPTV technique, Jasti and Higgs [13] avoided such error of the first two type by choosing a high frame rate of 3000 Hz and analyzing five trials of 450 frames for each data point, but could not avoid error due to finite pixel size as the maximum image size was determined by the resolution of the digital camera. Xu *et al.* [143] noted that the limitation of finite pixel size would be more likely to result in errors in granular temperature in the dense particle regime than in the kinetic regime. Other workers who have used DPTV approaches to characterize granular flows include Chambon *et al.* [15] and Jain *et al.* [16].

Since the pioneering work of Bagnold [18], experimental studies of the shear behavior of granular flows have continued to appear in the literature. A good summary of a number of these studies is provided by MiDi [144] who also comments on the common flow features shared by the configurations used in those studies. Earlier studies, such as those of Tardos *et al.* [145], measured macroscopic properties such as the global torque for a system where glass beads were sheared between concentric vertical cylinders. In other words, torque and

shear stress measurements were performed in a vertical narrow-gap Couette device containing a fine, dry frictional powder. Tardos and coworkers determined experimentally that, in a column of granular material undergoing continuous shearing, normal and shear stresses compressing the powder increase linearly with depth in a shearing column. Another study by Veje *et al.* [14] focused on detailed measurements of the local flow behavior by exploring the kinematic statistical properties of a two-dimensional granular flow using a Couette system consisting of photoelastic (polymer) disks undergoing slow shearing. The authors used particle tracking techniques to obtain local measurements of particle velocities, rotation rates (spins), and density distributions for the system. Mueth *et al.* [19] extend their investigations to three dimensional systems by combining the digital particle tracking technique with magnetic resonance imaging and x-ray tomography to capture the local steady state local property measurements of particle velocity, rotation and packing density for shear flow in a three-dimensional Couette geometry. It was concluded that key characteristics of the granular microstructure determine the shape of the velocity profile. Employing a two-dimensional rough annular shear cell, Jasti and Higgs [13] obtained local flow properties from video images taken in their granular shear cell (GSC) experiments using digital particle tracking technique, by averaging discrete kinematic data of individual granules within a polar rectangle. The purpose of the study is to understand the interaction of rough surfaces and granular flows. They divided the rectangle into six radial bins where bin one was adjacent to the moving inner wheel and bin six was next to the stationary outer wall. Each bin was approximately two particle diameters wide. They computed and reported the local tangential velocity, solid fraction, and granular temperature as a function of normalized bin radius. They also computed and reported the slip and total translational kinetic energy of the flow.

The operational parameters used in the various experimental studies differ depending upon the particular application of interest. For example, Jasti and Higgs [13] note that the shear rates and cell rotation rates used in some of the studies cited earlier ([14,19,145]) were lower than in studies performed by authors who are interested in the behavior of granular flows under conditions similar to those experienced in bearings, where linear velocities may range from ms to kms. Elliott *et al.* [146] performed some experiments at higher speeds,

but in their experiments, the conditions were maintained in the kinetic region by making use of shear cells where both the inner and the outer boundaries moved in opposite and relative motion. Liao *et al.* [147] and Hsiau *et al.* [148] also performed shear cell experiments at high speeds and rotation rates, but in their work, the granular material was confined within an annular trough where shear was created by the relative rotation of end disks and they only performed tracking on a small percentage of the tracer particles in their flow. Jasti and Higgs [13] performed high speed experiments to quantify and assess the effect of wall roughness on granular flows using digital particle tracking velocimetry to extract solid fraction, velocity, and granular temperature data from the experiments as a function of roughness factor and rotation rate. Marinack *et al.* [17] extended the work of Jasti and Higgs to further investigate the effects of parameters such as material dependent properties like the coefficient of restitution as well as the global solid fraction on the local flow properties of the granular medium. They studied the effect of changing the shearing materials on the local flow properties such as velocity, solid fraction, granular temperature, and slip. The concept was that a change in the relationship between the physical properties of the wheel and granules would affect the granule coefficient of restitution (COR). Their experiments included measurement of the coefficient of restitution values using a particle drop test apparatus analyzed by high speed photography.

For shear flow of granular materials where rough walls are present, the interaction and momentum exchange between the rough driving surface and the granules affects the behavior of the shear flow. It is particularly important to understand the role of wall roughness in the transfer of energy to the granular flow [17]. While a number of authors have understood the importance of the roughness of the wall boundaries on granular behavior, the approaches to include this effect have varied in the level of sophistication and quantification employed. For example, Mueth *et al.* [19] and Bocquet *et al.* [149] glued particles to the driving wheel to achieve an effective roughness factor while Elliott *et al.* [146] affixed toothed belts to the drive wheel to achieve the same effect. Jasti and Higgs [13] used a set of interchangeable driving wheels that was designed for the setup with different quantifiable roughness factor. They defined a wall roughness factor, R, which varied between zero for a moderately smooth wall to one for an extremely rough wall. Hui *et al.* [150] defined the roughness factor as

the fraction of lateral momentum transferred to the granules by the walls while Jenkins and Richman [151] chose a definition based on the the fraction of granules that fit exactly between the wall cylinders of the shear cell disks. Jasti and Higgs [13] defined a roughness factor similar but not identical to the latter definition. They defined the roughness factor R as the fraction of granules that fits between the wall hemispheres. In their work, a roughness of zero corresponds to wall hemispheres that are directly adjacent with no spacing for a granule to fit between them, while a roughness of one means that the gap between adjacent hemispheres is equivalent to one granule diameter. Jasti and Higgs noted that their definition had the advantage of being simple to implement and quantify. In their arrangement, a set of interchangeable inner wheels were used in their granular shear cell, each having a different roughness prescribed by the size of steel hemispheres protruding from the aluminum wheel.

2.5.3 Computational Studies of Granular Flows

The flow of granular materials can display behavior similar to solids, liquids, or gases depending upon the flow conditions and granular properties [6]. Experimentally, it is difficult to measure the bulk properties of the granular materials such as stress, strain, and voidage, as well as macroscopic flow variables such as velocity and granular temperature profiles. McCarthy *et al.* [8] noted that while a host of non invasive experimental have been employed to characterize granular flows, no one method has proven to be a generally suitable framework for building or validating theoretical granular flow models due to difficulties in simultaneously gathering and evaluating all of the required information.

These issues have led to increasing reliance on computational modeling of particulate flows either as an alternative or supplement to experiments as a complement to theoretical approaches. Discrete element modeling (DEM) is a frequently chosen computational method for this purpose. In the DEM method, the macroscopic behavior of a particulate system is captured via calculation of the trajectories of each of the individual particles within the system. The manner in which these computed trajectories evolve over time determines the global flow of the granular material. DEM based methods for simulating granular flows have become popular partially because they offer a way to extract the kind of detailed information

for these flows that is difficult to measure experimentally. From a validation viewpoint this is something of a conundrum, because it also tends to make the kind of experimental data that can be used to directly validate the results of DEM simulations scarce. Therefore, many researchers have chosen to validate DEM results in qualitative ways, using comparisons based on global features such of mixing rates and gross features of concentration profiles.

Due to the deficiencies of experimental methods of flowing granular materials, Campbell and Brennen [20] developed a computer simulation to describe two-dimensional unidirectional flows of inelastic fully rough disks. They present results that include distributions of velocity, density, and granular temperature (a measure of the kinetic energy contained in the random particle motion) for Couette shear flow calculations with two types of wall boundary conditions. Computationally, the authors compared the shear and normal forces on the solid walls with the experimental and theoretical results, in addition to exploring the effect of density and shear rate on the granular temperature. Furthermore, this simulation technique has been applied to gravity-driven inclined chute flows [104] and the gravity-free flow in a Couette shear cell, where both models show good agreement with independent experimental measurements.

Kuo *et al.* [22] studied granular flow in a V-mixer and developed a number of quantitative methods for comparing DEM and experimental data. In their analysis, the authors modeled the mechanical interactions between particles and between particles and walls in granular flows using linear springs, dash-pots and friction sliders. The authors compare their simulation results with results derived from radioactive tracer measurements of particle motion, and reported remarkably good agreement for restitution coefficient values of 0.7 and 0.9, internal friction coefficient values of 0.3 and 0.6 and wall friction coefficient values of 0 and 0.3. They state that the internal and wall friction coefficients are important in determining the initiation of particle movement, while the value of the restitution coefficient has a larger influence on particles in a dynamic state.

The significance of boundary conditions on the dynamics of granular flows have been observed both in experimental and computational results. Lun [134] developed a numerical study to simulate an assembly of inelastic, frictional hard spheres inside a control volume undergoing a steady-state rapid Couette flow induced by the top and bottom bumpy walls.

The bumpy walls are made of hemispheric particles fixed to two parallel flat plates, where collisions between the flow particles and the exposed flat areas of the walls are permitted. The study demonstrate the effect of bumpy walls on the trasport properties such as stress and energy dissipation. The results show that different wall-particle packing patterns with the same solid fraction of particles at the wall cause variations in stresses and slip velocity. It was reported that at high solid fractions, the wall-particle concentration and distribution can have a significant effect on the dynamics of the flow system by directly influencing the collisional angle distribution and the collisional frequencies of the flat wall and the individual wall particle, thus changing the effectiveness of transmitting energy and momentum from the bumpy walls to the flow field.

Louge *et al.* [152] employed computer simulations to investigate rapid granular shear flows driven by identical, parallel, bumpy boundaries. The results of the numerical simulations for the rapid, steady shear flow of identical smooth and nearly elastic disks are compared with the predictions of Hanes *et al.* [153] for the shear stress, normal stress, and gap width. Louge and coworkers indicated that the variations of the dynamic friction coefficient (large or small) are confirmed by the simulations by suitably preparing the boundaries of the cell. The results of the simulations are in good agreement with the theory of Hanes *et al.*. In another study, Louge [21] investigated rapid granular flows of spheres interacting with a flat, frictional boundary using computer simulations. In this work, the theory of Jenkins [154] was tested using numerical simulations for the interaction between a rapid granular flow of spheres and a flat, fictional wall. The results indicate that the dynamic friction coefficient and the normalized flux of fluctuation energy depend on the collision properties of the boundary and the normalized mean slip of the contact point. Although the theory captures the trends of the boundary conditions at low friction, the results show that it does not predict their behavior at large friction. The author concluded that Jenkins' assumptions in his theory can be improved.

P*ö*schel and Buchholtz [155] reported a study of two-dimensional molecular dynamics (MD) simulations of a spherical and non-spherical granular material flowing in a rotating cylinder with constant angular velocity. For the spherical particles, it was found that the flow fluctuates irregularly with time, and that the angle of the material as well as the velocity

of the grains at the surface fluctuate significantly. Unstable convection cells are formed due to the flow of the particles in the rotating cylinder. While several cells are observed for low but constant angular velocity, only one cell is captured for high angular velocity. When using non-spherical particles, the simulations show that the flow moves in a stick-slip fashion, where avalanches of different size at the surface of the flow occur. The non-spherical particles consist of four spheres at the corners of a square and one in the middle of the square which radius is chosen to touch the others (see Figure 10 in Ref. [155]). Hence, it was found that the inclination of the granular material with the non-spherical grains is more than two times larger than in the simulations with the spherical ones. The results in this study agree with experiments by Rajchenbach [156].

Using molecular dynamics (MD), Schöllmann [24] investigated simulations of a two-dimensional cylindrical shear cell. It was shown that MD simulations are capable of reproducing the main features of granular shear flow in a Couette shear cell consisting of many photoelastic disks, when the simulation results were compared to those of experiments. It was found that the distribution of tangential velocity of the disks shows an exponential decrease within the shear zone near the inner ring. In addition, the probability distributions of the fluctuating tangential, radial, and angular velocities of the disks become narrower with increasing distance from the inner boundary. The influence of both coefficient of restitution and friction coefficient was found to be insignificant on the tangential velocity profile. On the other hand, packing fraction has a crucial role in determining the system's response, particularly the distribution profiles of the tangential velocities.

While many discrete element method (DEM) simulations and modeling have considered two-dimensional flows and circular particles, Cleary and Sawley [157] reported three-dimensional case studies and the effect of particle shape on hopper discharge by employing DEM modeling for an industrial granular flow. The authors indicated that the incorporation of the choice of particle shape into DEM models is very important and allows many flow features, particularly in hoppers, to be more accurately reproduced. It was shown that elongated particles produce flow rates up to 30% lower than for circular particles and give flow patterns that are quite different. In addition, the 3D case studies that the authors presented indicate that DEM modeling is sufficiently advanced that it can make useful contributions to

process optimization and equipment design, where complicated geometries executing complex motion can be modelled easily. Finally, it was reported that simulations of flow through a vibrating screen and discharge from single, and four, port cylindrical hoppers illustrate the potential of DEM to handle diverse aspects of particle handling equipment. Other investigations by Cleary and coworkers can be found in references [158, 159].

A direct comparison between a physical experiment and a parallel computer simulation, using discrete element method (DEM), of rapidly sheared granular materials in an annular shear cell was reported by Ji *et al.* [26]. Experimentally, a normal load was applied when the annular shear cell was filed with particles. While the bottom of the shear cell was rotated at a given speed, the top boundary was held stationary in the horizontal direction but allowed freedom to move up and down. Computationally, the authors used artificially softened particles to reduce the computational time to a reasonable level. In order to ensure that such artificial modification is acceptable, a sensitivity study on the particle stiffness was investigated. A qualitative discrepancy of nearly a factor of two was reported when comparing the required torque to shear the materials under different rotational speeds between the experiment and the simulation. A number of parameters such as boundary conditions, particle size distribution, particle damping and friction (sliding and rolling), and contact force model were tested to determine their effects on the computational results. It was concluded that rolling friction between particles, which is not commonly considered in many DEM models, had the most significant effect on the macro shear stress levels among all other parameters.

McCarthy *et al.* [8] performed experiments and simulations in a horizontal granular shear cell in order to obtain detailed local information for the velocity, granular temperature, and solids fractions profiles both experimentally and computationally to facilitate validations of the predictions from their DEM simulations. Their experimental measurements were obtained using digital particle tracking velocimetry. In their DEM simulations, the authors considered, using DEM, the effect of a variety of contact mechanics inspired force interaction laws and also performed a sensitivity analysis on device and particle geometry and material properties. The authors report that the three experimentally measured profiles proved to be a powerful discriminator between the varieties of force models typically used in the literature. They found that even through their particles were as close to spherical as possible for a

commercial supplier source, they found it necessary to model the very slight asphericity in order to obtain good quantitative matching to experimental data. They also suggested that planar 2D simulations may not be suitable for pseudo two-dimensional experimental geometries. They also found that for their force interaction models, a plastic deformation mode of dissipation is superior to spring-dashpot models, while the choice of friction model had little effect.

In an effort to better understand the physical phenomena that control the particle flow in mixed-flow dryers (MFD), Iroba *et al.* [142] developed a two-dimensional simulation model for the grain mass flow in a mixed-flow dryer based on discrete element method (DEM). The model was used to investigate the influence of the side walls and air ducts on solids mass flow by evaluating the residence time distribution (RTD), particle velocity profiles, and particle trajectories. The results obtained show that particles with low velocity move near the wall region, in which wall friction dominates the bulk particle movement. On the other hand, high velocity particles concentrate in the central region where particle-particle forces are dominant. Due to the fact that grains in the MDFs have different vertical velocities, this results in different residence times of every single portion of grains. In conclusion, the comparison between the simulated and experimental results confirms and verifies the DEM calculation ability for predicting the main features of particle flow.

3.0 THERMAL CYCLING OF GRANULAR MATERIALS

3.1 INTRODUCTION

One of the traditional ways to increase the solid fraction of a granular system is the use of mechanical energy. Solid fraction is defined as the fraction of volume occupied by the solid grains rather than the void space. As indicated earlier in Section 2.1.2, mechanical consolidation can increase the solid fraction in a granular bed. We can illustrate that experimentally, as shown in Figure 9, where a polymer material was confined in a container with different weights on top. The voids between the materials decrease with time during the loading process due to the force introduced and the height of the bed shrinks. In Figure 9, we can see that the solid fraction increases with time due to the confining pressure applied on the materials (5.5 kPa and 9 kPa, respectively).

As a result of the applied confining pressure, the materials in the bed start to deform or overlap with time. It can be seen from our study that, in both cases, there is a very rapid change in solid fraction (consolidation) initially, possibly due to mechanical rearrangements, followed by a much slower evolution in density or solid fraction which can be likely attributed to viscoelastic relaxation. So, we see a faster solid fraction increase at the beginning of the experiment (first 2-3 hours), where most of the deformation takes place. After longer hours of the experiment, we see very little increase in the solid fraction with time. In addition, when the applied confining pressure is increased, it results in larger magnitude of the solid fraction increase in the bed.

In the remainder of this chapter, we show how we can produce the same results without the input of any mechanical energy. To accomplish this, we use thermal cycling, which is explained in the following sections. We use experiments and simulations to study the effect of

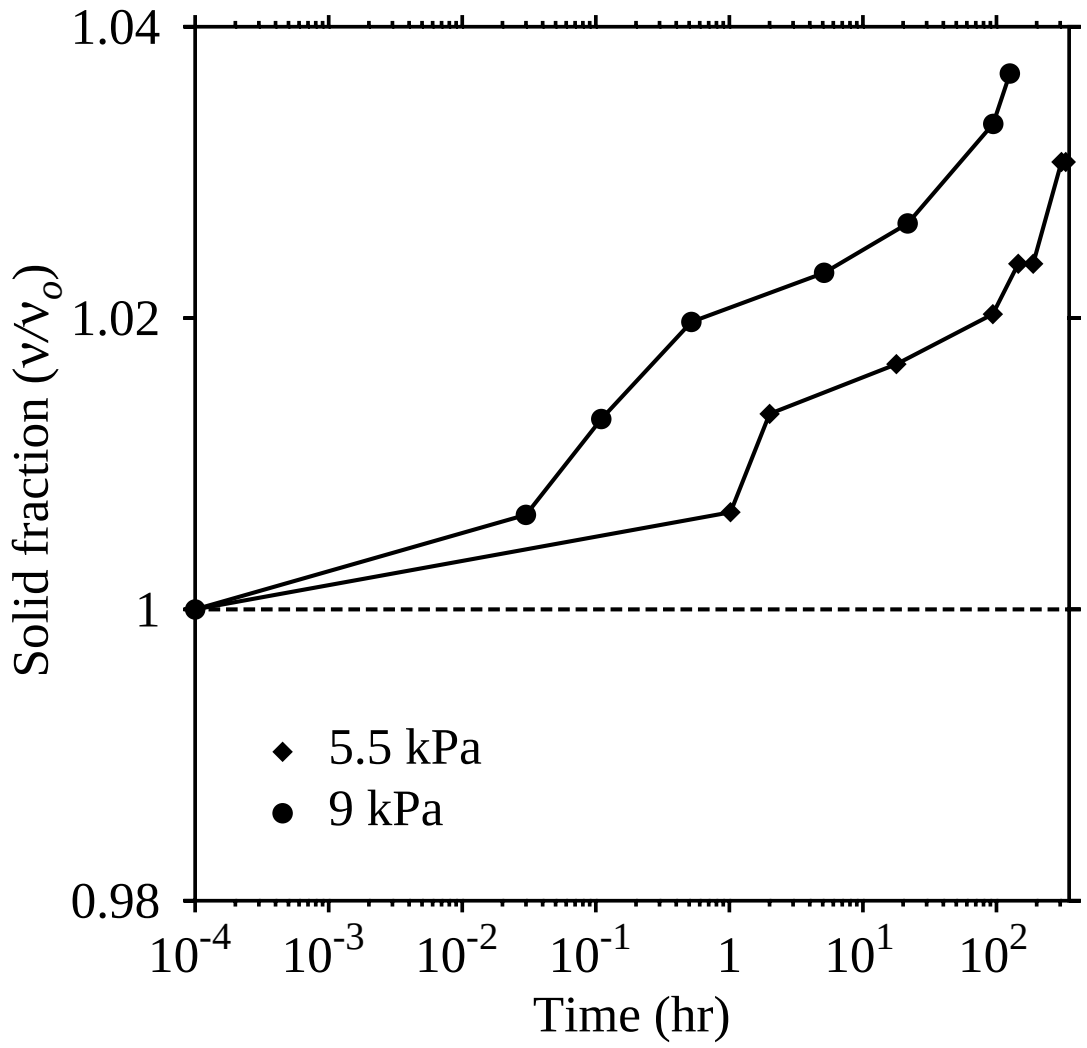

Figure 9: Mechanical consolidation: Solid fraction as a function of time for different confining pressures using polymer materials

confining load on different sizes of packed beds. We show computationally that the packing fraction can be increased using thermal cycling with lateral periodic conditions. Simulations of thermal cycling with side walls were performed in a previous work by Vargas *et al.* [67]. The purpose of this work is to show that consolidation can take place with the absence of the side walls.

3.2 EXPERIMENTAL SET-UP AND PROCEDURES

The experimental setup for our packed bed thermal packing experiment is illustrated in Figure 10. We fill the granular materials very carefully into cylindrical containers made of plastic using a retractable funnel. Then, the samples are slowly placed into a vacuum oven with a clear window door (Fisher Scientific, Model280A) where a picture is taken to establish the initial condition state. The materials in the oven are gradually heated to a preset temperature and held there long enough to ensure a uniform temperature in the packed beds before being gradually cooled down to the initial ambient temperature, where a picture is again taken to reflect a new state which completes a single cycle. In fact, for the long duration experiment, the samples were kept for more than 15 hours during the heating or cooling processes to achieve the thermal equilibrium between the oven and the particles inside the packed beds. This Thermal Cycling process is repeated for as many cycles as needed with a picture taken for the samples at the end of each cycle.

The oven temperature is adjusted by a control knob on the oven. The position of the knob reflects an approximate temperature known from calibrations of the oven prior to the experiments. A thermometer inside the oven was used to determine the target temperature and to ensure that the knob position reflects the desired temperature.

The cycle's pictures are taken using a Nikon D40 camera. Image processing was performed for these pictures to determine the apparent height change. Basically, the images for each type of material (cellulose acetate, steel, etc.) from all cycles were cropped so as to obtain the same dimensions (height and width). The cropped images are processed so that the cropped area is a little bit above the surface of the material. This is because we

want read the image as pixels and count those that are in the empty space. The pixels above the surface of the material give an indication of the change in the bed height during the cycling process, and allow for the determination of the apparent height of the bed. We perform a threshold for the cropped images and calculate the number of pixels of the void space. We qualitatively compare the threshold image with the real one, and in some cases, we manually perform a threshold using the GIMP software to make some adjustments to the image because they were qualitatively different. After that, we divide the apparent height for each cycle by the initial height to normalize it. We then plot the obtained results as a function of the cycle number.

3.3 SOLID FRACTION AND APPARENT HEIGHT RELATIONSHIP

In the previous sections, we discussed the methods used for the simulations and experiments. Here, we will explain how the data collected from those simulations and experiments will be studied. We will test the data in two ways. In the first approach, we will look at the normalized solid fractions obtained from the simulations, whereas in the second one, we will record the normalized apparent height measurements from the experiments. While it is possible to obtain both the solid fraction and the apparent height from the simulations since the data are available, we will concentrate on the solid fraction as it is the focus of our work. In addition, we are simulating transient behavior so the solid fraction at each instant of time is known. The experiments do not include transient behavior, because it is hard to measure the solid volume during heating and cooling processes. Also, for the long duration experiments we measure at steady state only.

Hence, the simulations and the experiments differ in how they are conducted, but this is out of necessity since the simulation of the full approach to cool down would take a very long time. Ultimately, the solid fraction and the apparent height are going to be interrelated. Yet, the simulation and the experiment here should not be considered a one-to-one match. They can be predictive in a qualitative sense but not necessarily in a quantitative one.

Since image processing is employed in our experimental techniques, the apparent height is the only accessible measurement we can analyze for the purpose of this study due to the measurement choice and set-up limitations. Hence, we will introduce a way to relate the solid fraction to the apparent height. For the long duration cycling, the relationship can be formulated in a simple way if we assume that the volume and the area of the solid material are measured at the same room temperature. However, we will be very careful to not assume this unless we know that it is true. We can define our normalized solid fraction as follows:

$$[\frac{\nu}{\nu_o}] = \left[\frac{V_{solid}/V_{bed}}{V_{solid_o}/V_{bed_o}}\right] \tag{3.1}$$

At the end of each cooling cycle, both the oven and the material inside were cooled down (more than 15 hours) to room temperature. So, temperature does not play a role in our analysis because we are always taking measurements at the same bed temperature. This allows for $V_{solid} = V_{solid_o}$ and Equation 3.1 can be reduced to

$$[\frac{\nu}{\nu_o}] = \left[\frac{V_{bed_o}}{V_{bed}}\right] = \left[\frac{h_o}{h}\right] \tag{3.2}$$

Hence, we can conclude that the solid fraction is inversely proportional to the apparent height for the long duration thermal cycling trials.

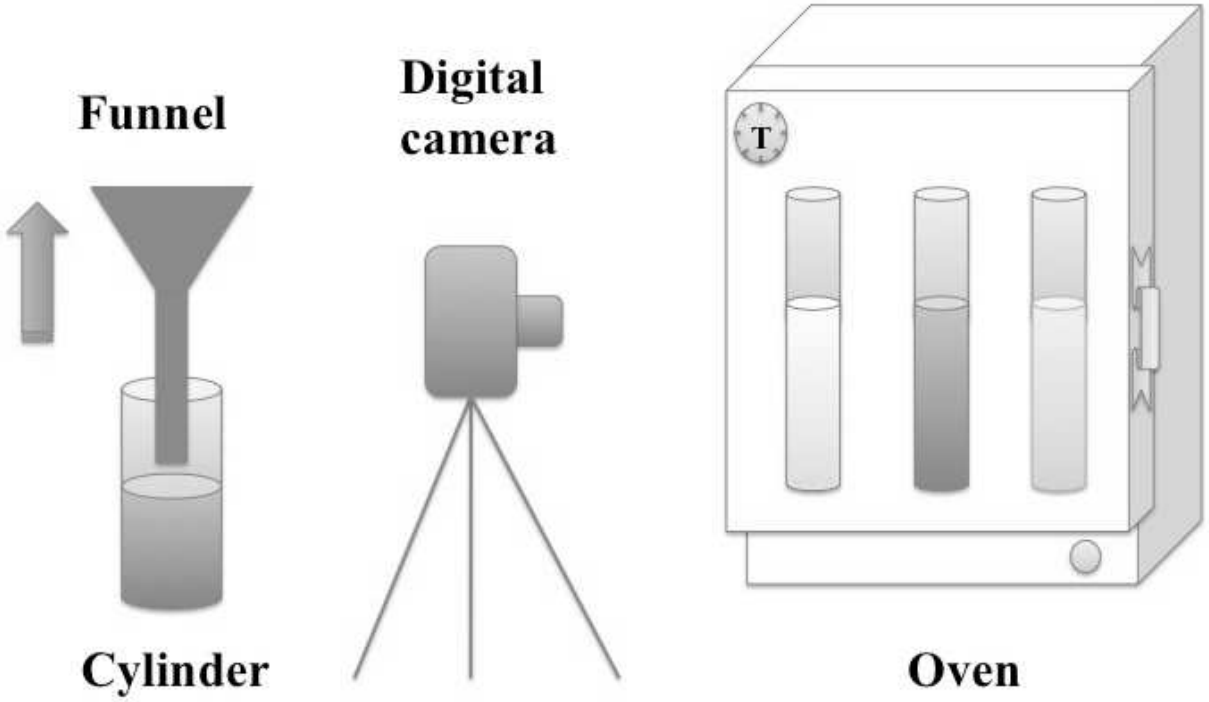

Figure 10: Experimental setup of the packed bed thermal packing experiment

3.4 THERMAL CYCLING RESULTS AND DISCUSSION

In thermal cycling, we can increase the granular packing (solid fraction) simply by raising and then lowering the temperature. In the heating process, the particles undergo thermal expansion which could lead to a rearrangement or settling. This configuration change is not reversible upon cooling. To illustrate how this can be achieved, we used the Thermal Particle Dynamic (TPD) simulations along with experimental studies. In the simulations, we tested models for two-dimensional (2D) and three-dimensional (3D) packed beds bounded by top and bottom walls. The beds are laterally periodic which is the significant factor in this work. In other words, the bed's sides do not have walls. The heating and cooling is applied to the top wall only. Moreover, the top wall is moveable but the bottom wall is fixed. An initial condition for the simulations is obtained by perturbing a 2D or a 3D lattice and allow the particles to settle onto the bottom wall under the action of gravity. The thermal simulation starts with a bed of particles at low temperature which undergoes a step change (increase) in temperature at the top wall (heating step). During the heating process, the thermal and mechanical response of the particles is monitored in time until the bed reaches a certain state, depending on how long we want to cycle for. At this point, and for the same amount of time of the previous step, the system is given another step change (decrease) in temperature to allow the particles bed to cool down (cooling step). This thermal cycling process is repeated as many times as needed.

3.4.1 System Geometry

In this section, we study how the confining load can impact the solid fraction and the apparent height of a packed bed. For the simulations used in this work, the mass of the top wall particles are adjusted by changing their densities as a means of controlling the amount of weight or force applied on the top particles. To find out the effect of confining load on consolidation, we ran several 2D and 3D simulations using a "soft" material. The "soft" material is a hypothetical material that has properties similar to Cellulose Acetate with thermal conductivity typical of a metal. We used "soft" material to allow for the

simulation to run faster. The time-step is inversely proportional with Young's modulus as shown in Equation 2.6. So, the stiffer the material is, the smaller the time-step is (makes the simulation very slow). However, we make Young's modulus small enough to keep our strain on the individual particle relatively small (about 0.1%). If we make it too small, then the overlap becomes big and our contact mechanics will fail and nothing is accurate in the simulation. Table 1 shows a list of the material properties used in our simulations and experiments.

Two 2D simulations were investigated. In the first simulation, all particles including those on the top wall share a uniform density, as shown in Figure 11(Left), which in this work we term "no confining load". In the second simulation shown in Figure 11(Right), the density of the top wall particles was 1000 times greater than the rest of the bed particles. We call this configuration "1000x confining load". The 2D simulation results indicate that during the thermal cycling process both the apparent height and the solid fraction show no dramatic change as the cycle number increases. For both confining loads, Figure 12 shows very small increase in bed height (about 0.1%). Also, the solid fraction increase is very similar in both confining load cases and it doesn't exceed 0.1%, as shown in Figure 13. The fact that the maximum number of interactions between a particle and its neighbors in a 2D lattice is limited to eight possible interactions indicates that the particle rearrangements are very limited for the 2D case since there isn't much room for the particles to move about during the expansion and contraction of the bed. So, the bed's apparent height for both cases of the confining load simulations indicates a small increase in the total volume of the bed. We can conclude that thermal cycling for a 2D simulation significantly limits consolidation due to the type of interaction between each particle and its neighbor which limits particle mobility.

Table 1: Parameters of different material properties

Parameter	**Soft**	**CA**	**Steel**
Young's modulus (GPa)	0.085	1.5	193
Density (Kg/m^3)	1200	1300	7900
Poisson ratio	0.33	0.43	0.29
Conductivity (W/mK)	300	0.20	15.0
Coefficient of thermal expansion ($1/K$)	7.3×10^{-5}	7.3×10^{-5}	12.5×10^{-6}
Coefficient of friction	0.30	0.30	0.30
Heat capacity (J/KgK)	900	1400	477

CA $\equiv$ Cellulose Acetate

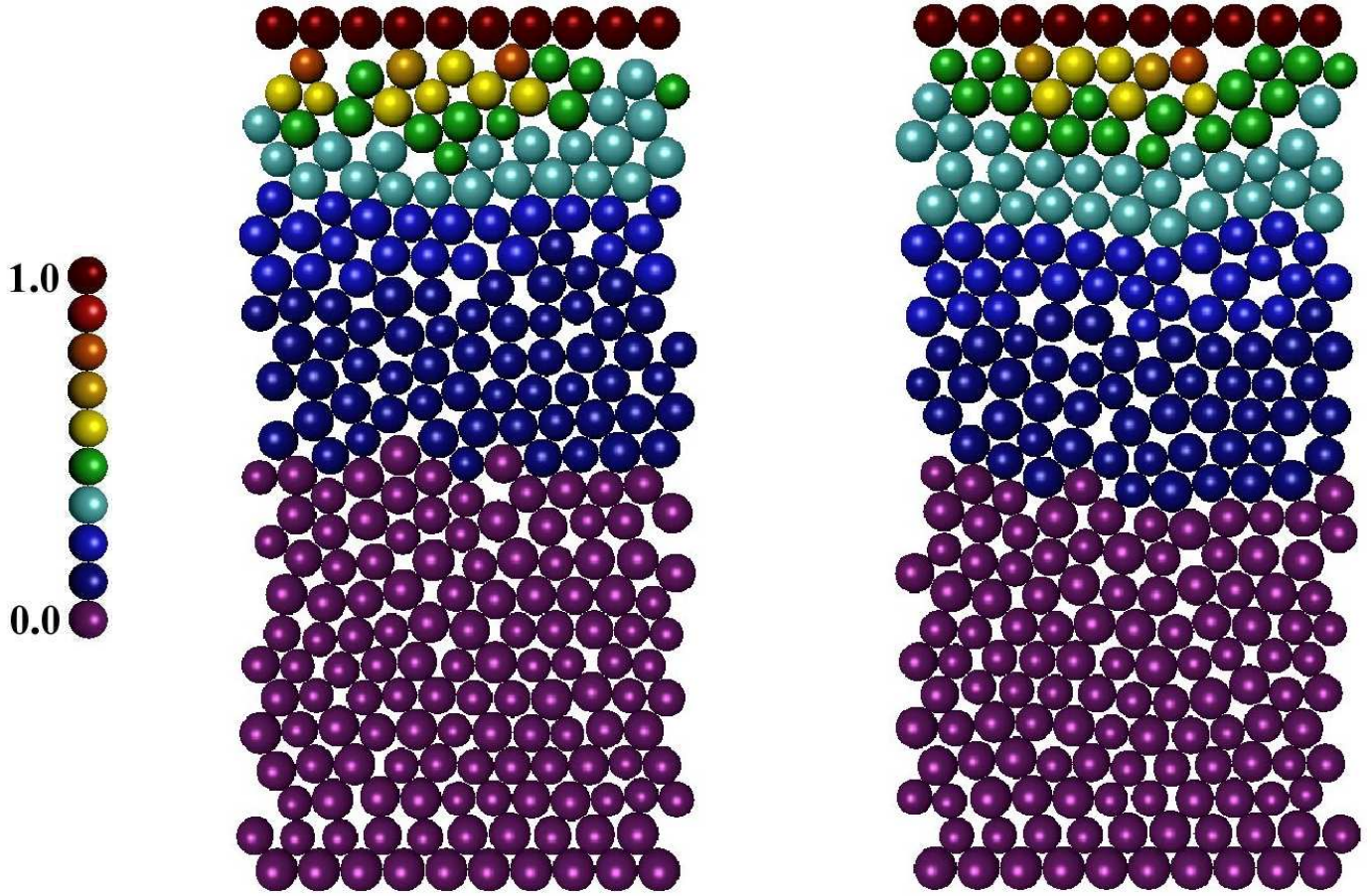

Figure 11: Snapshot of the different confining load simulations in 2D during the heating cycle. Left: No confining loads. Right: 1000x confining load. The scale shown is a representation of the dimensionless temperatures

Using the same confining load settings described for the 2D simulations, we examined the change in the solid fraction and apparent height in 3D simulations. In the 3D simulations, the number of particles touching a single particle increases in comparison with the 2D cases since there is now an extra dimension for the particles to settle in. In other words, the number of interactions between a particle and its neighbors can be as high as 32 in a 3D bed. This indicates that more interactions can take place between the particles and it should allow more room for the particles to rearrange during the thermal cycling process.

Figure 14 shows the confining load configurations for both the "no confining load" and the "1000x confining load" for the 3D simulations. The results clearly indicate that the higher confining load case has more particles at higher temperatures when compared to the no load case due to the increase in the density of the top wall particles. Additionally, the interaction with the neighboring particles is increased in the 3D simulations which allows for more mobility for the particles. In Figure 15, we can see an immediate consolidation in the "1000x confining load" case where the apparent height shows about 1% decrease around the third cycle number. Since the purpose of our simulation is not to test for bed consolidation at higher top wall densities, we decided to stop at the third cycle for the "1000x confining load" case as this scenario does not reflect a real case for our experimental granular materials or other natural phenomena.

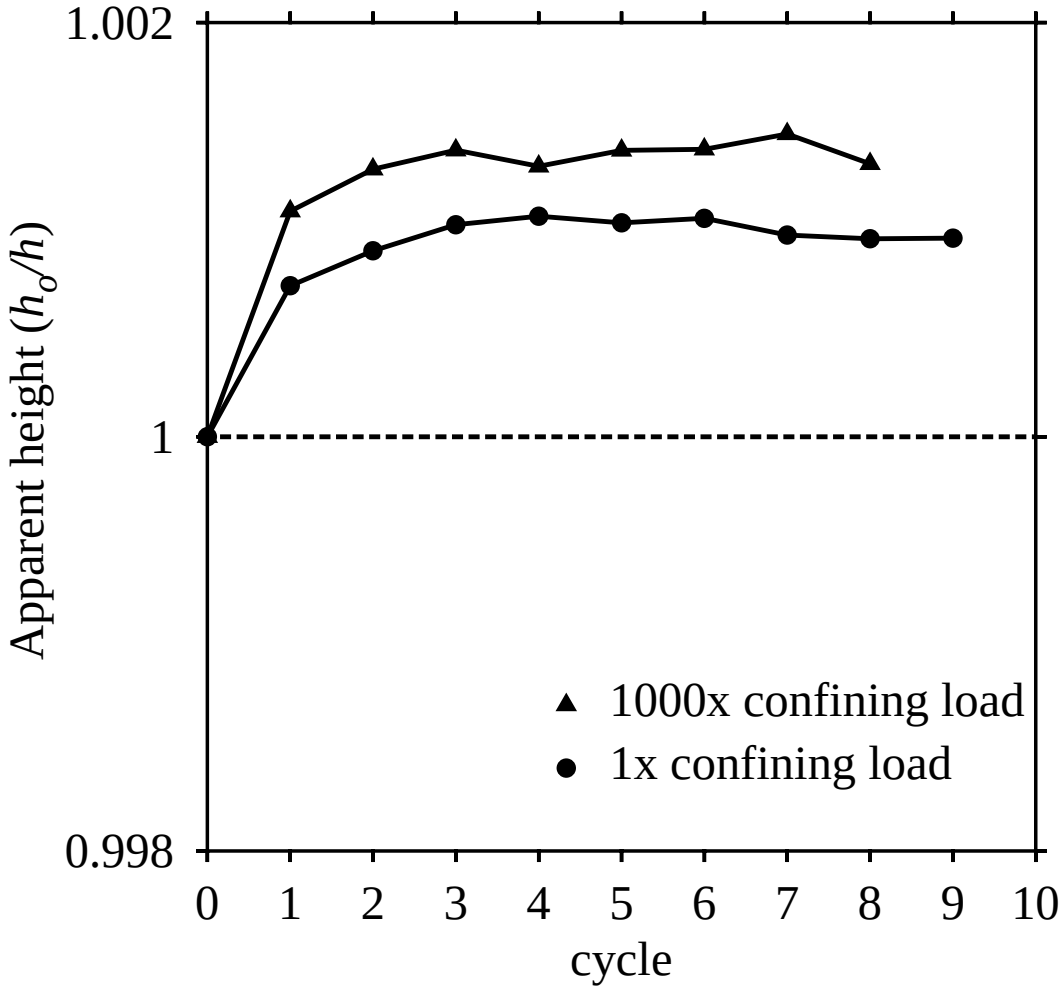

Figure 12: Apparent height as a function of the cycle number for the simulations in 2D

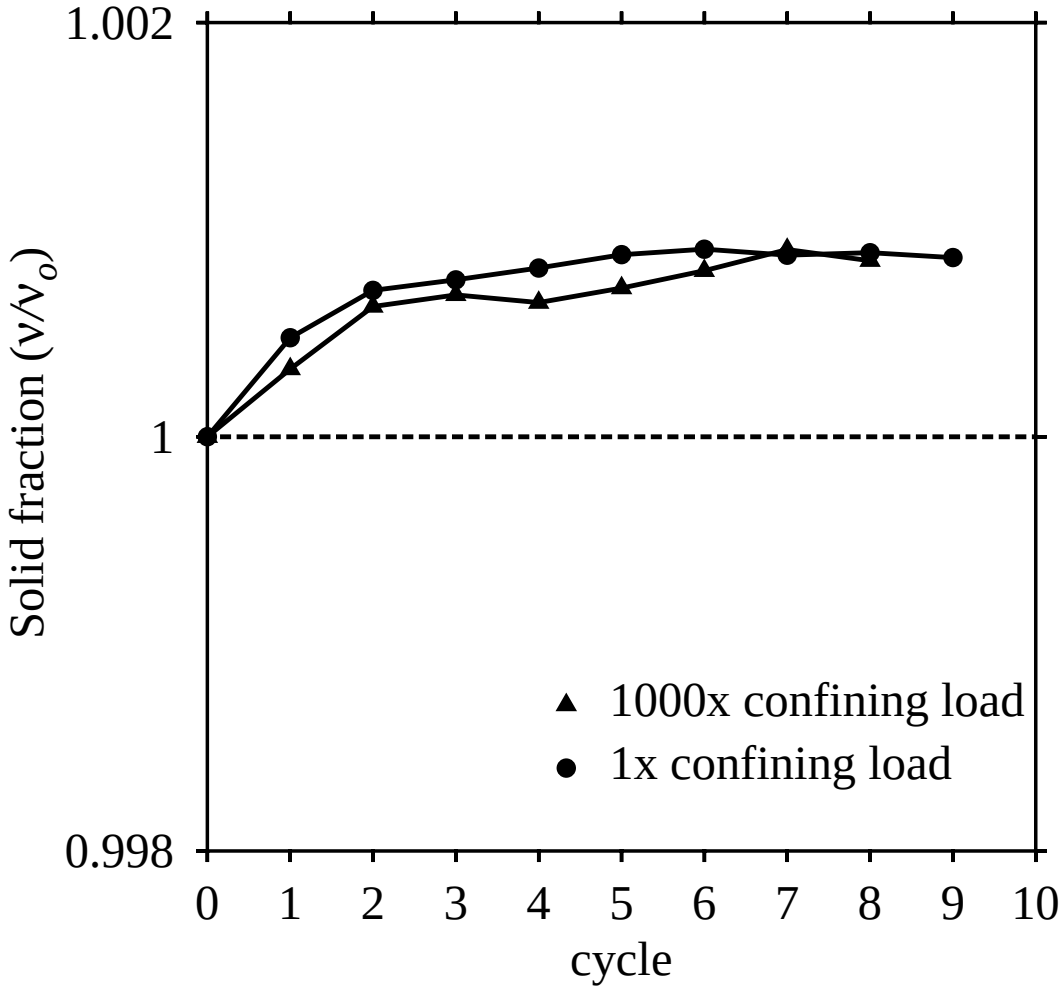

Figure 13: Solid fraction as a function of the cycle number for the simulations in 2D

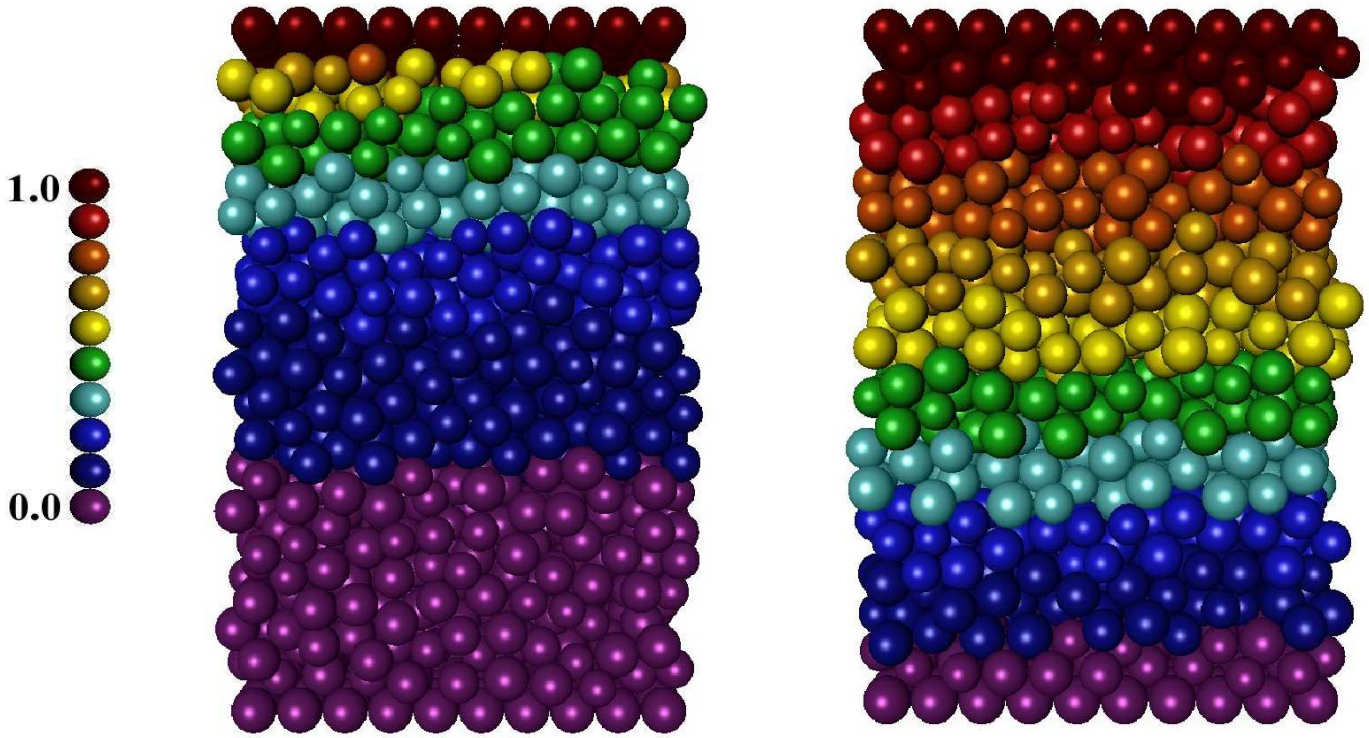

Figure 14: Snapshot of the different confining load simulations in 3D during the heating cycle. Left: No confining load. Right: 1000x confining load. The scale shown is a representation of the dimensionless temperatures

For the "no confining load" case, the bed initially expands during the first cycle then it starts to consolidate along with the remaining cycles. To illustrate, the mean temperature of the bed ramps up initially during the first cycle until it reaches a steady state condition and the bed expands. This expansion results in change in the bed configuration and particles rearrange upon cooling to form a more stable configuration. Hence, starting from the second cycle, we see the bed starts to consolidate. The solid fraction in both confining load cases increases with the increase of the cycle number as shown in Figure 16 and consolidation takes place.

From the simulation results, we were able to show consolidation for our packed beds with no wall effect. In other words, we showed that we can increase the solid fraction using periodic boundary conditions for the sides of the bed. The main reason for the increase in the solid fraction is the thermal expansion effect for the particles that resulted in rearrangements in the particles configuration.

3.4.2 Particle Mobility

In the experimental work, we studied the particle movements in different packed beds qualitatively and quantitatively and compared them with the simulation results. Also, we investigated the compaction of different granular materials in packed beds. We used steel and cellulose acetate in our experiments and the parameters for those materials are listed in Table 1. In the experiments, plastic cylinders were used to hold the granular materials inside an insulated oven with a window door. The cylinders were carefully and slowly placed inside the oven to avoid any type of vibration or perturbation to the materials. The thermal cycling process was performed by simply switching the oven's on/off button. A picture of the granular materials inside the oven was taken after the end of each cycle for image processing analysis. We performed two types of experiments with different thermal cycling evolution time. In the first one, each heating and cooling cycle took more than 15 hours to allow the particles and the surroundings (oven) to reach a steady state. This is to ensure that a uniform temperature of the particles inside the cylinders and the oven is reached before the new half-cycle starts. In contrast, the second experiment was for a shorter time (one hour or

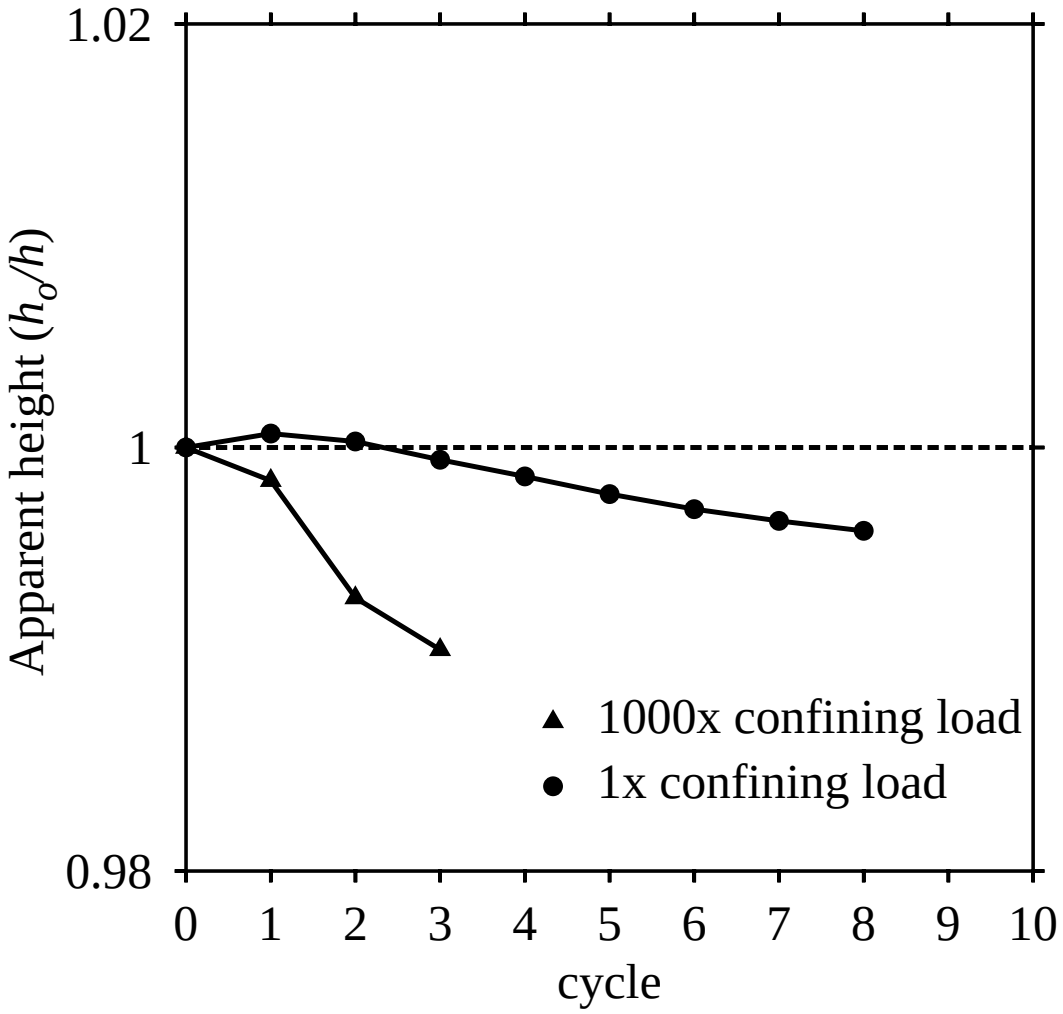

Figure 15: Apparent height as a function of the cycle number for the simulations in 3-D

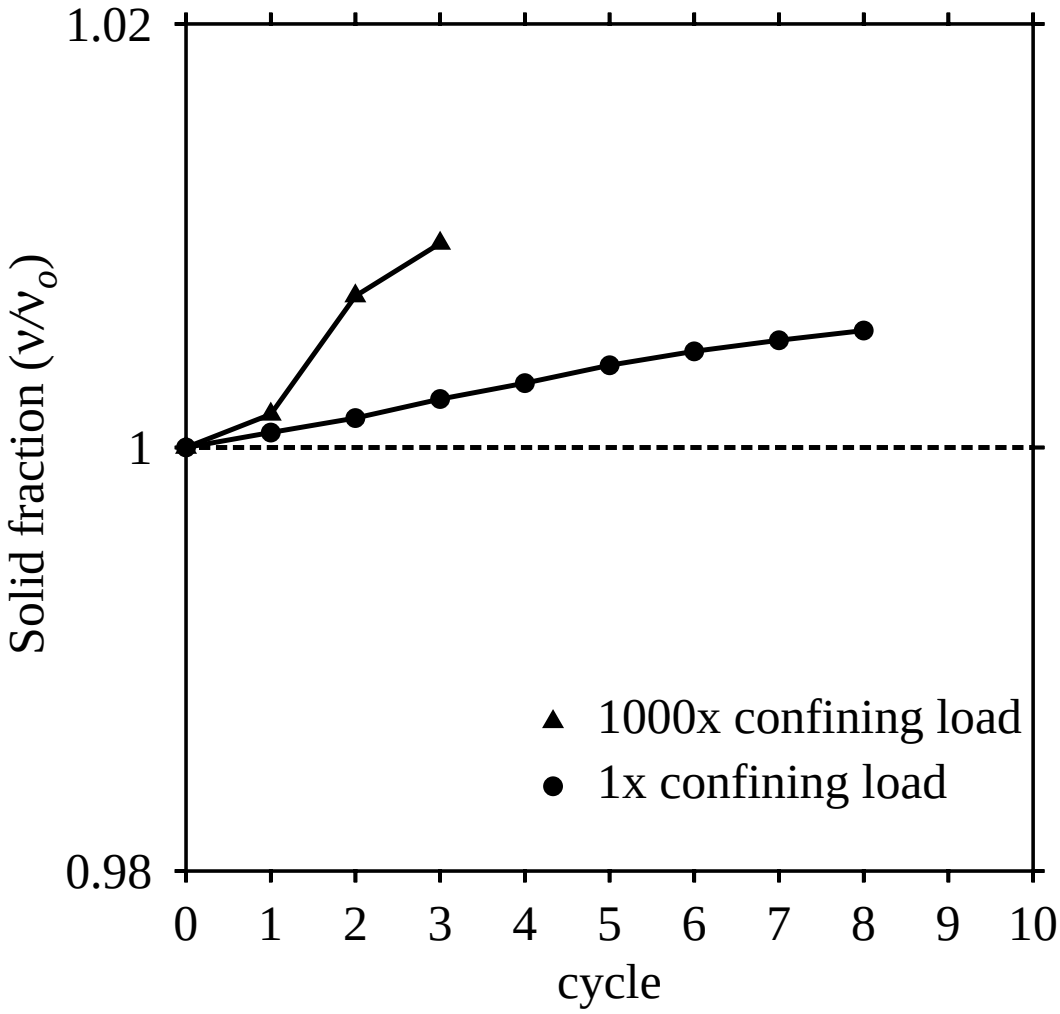

Figure 16: Solid fraction as a function of the cycle number for the simulations in 3-D

less) in which the particles don't reach a steady state temperature during the thermal cycling process in an attempt to mimic the simulation procedures. However, the mean temperature of the bed gradually reaches a steady state after the first two cycles. We will discuss those two types of experiments in Section 3.4.3.

Although it was very hard to see the rearrangements of the particles inside the cylinders with the naked eye, we were able to qualitatively show that this change in configuration occurs using image processing. We used image processing to process and combine about 15 images (or cycles) that were taken for steel materials undergoing thermal cycling to show the particle movements during these cycles.

Figure 17 on right shows the streaklines, or wiggling motion, of all the particles inside the bed at the end of the 15th cycle. The white clouds around the black dots represent the amount of wiggling that each particle attained during the entire process. The particles in the bottom half of the cylinder exhibit a limited amount of wiggling action during the cycling processes, which indicates very small movements of the particles. On the other hand, the particles that smear at the top are the ones that actually represent the rearrangement that causes the bed eventually to settle and consolidate.

These experimental results were compared to the simulation results as illustrated in Figure 18. In the simulation, we see the same sort of behavior observed in the experiments where the particles at the bottom of Figure 18(Left) are essentially just wiggling in place, but for the particles at the top, we do in fact see motion of some particles. Moreover, some particles have relatively large net motion especially at the top as shown in Figure 18(Right).

Figure 19 shows quantitative measurements from both simulations and experiments where the mobility of the particles at the top of the bed is greater than that at the bottom. The simulation results for different cycles in figure 19(Left) show smooth lines for the cycles due to the fact that we are considering the full three-dimensional set of particles and there are no lateral walls in the simulation. So, clearly the side walls are not influencing the particle movements, whereas, in the experiments, as shown in Figure 19(Right), the lines are much noisier because we are only seeing the particles near the wall (two-dimensional) and the wall is influencing the particle movements. Hence, these wall particles are not representative of the whole bed.

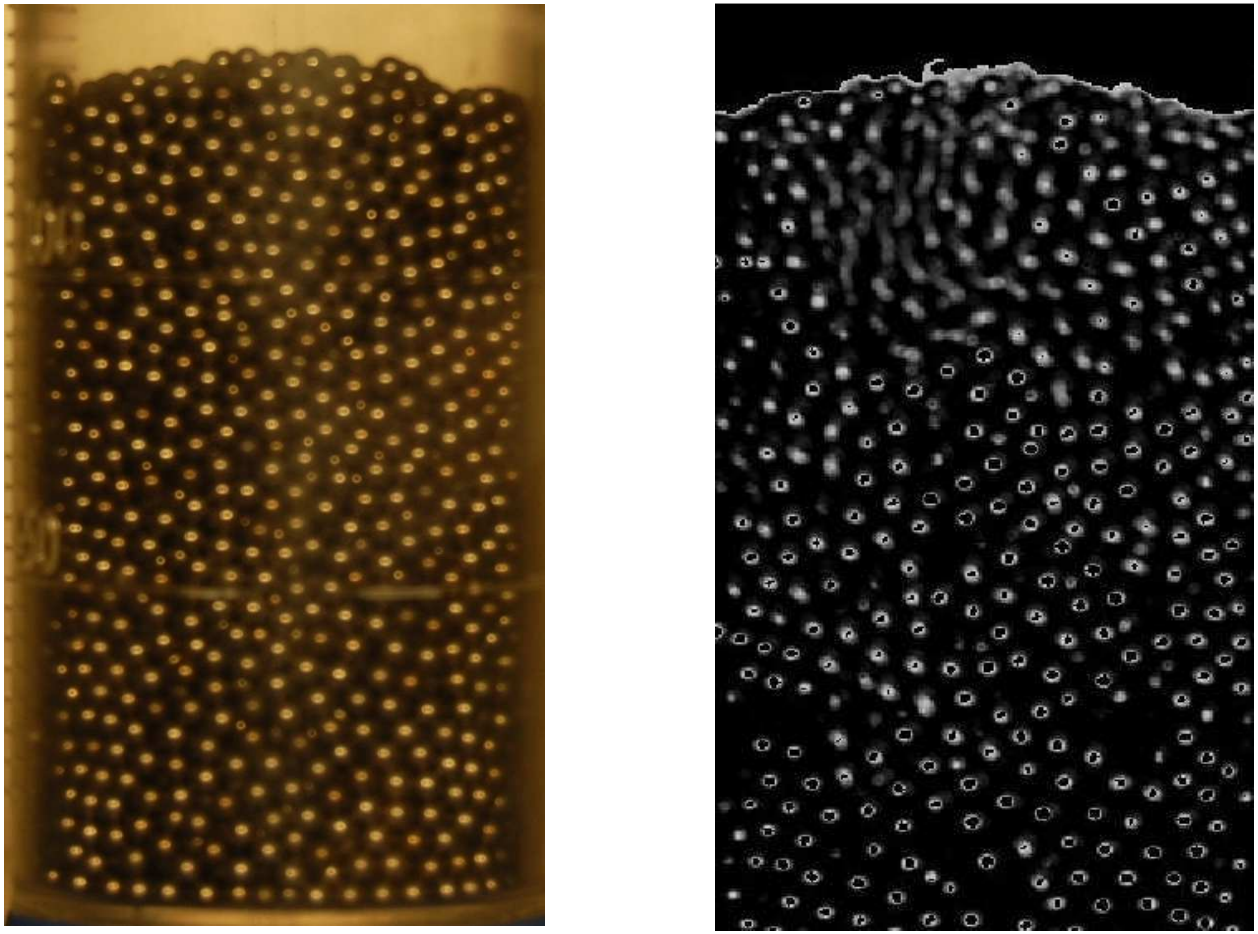

Figure 17: Left: An image of the initial condition for steel before image processing. Right: An analyzed image of the streaklines for steel material undergoing experimental thermal cycling

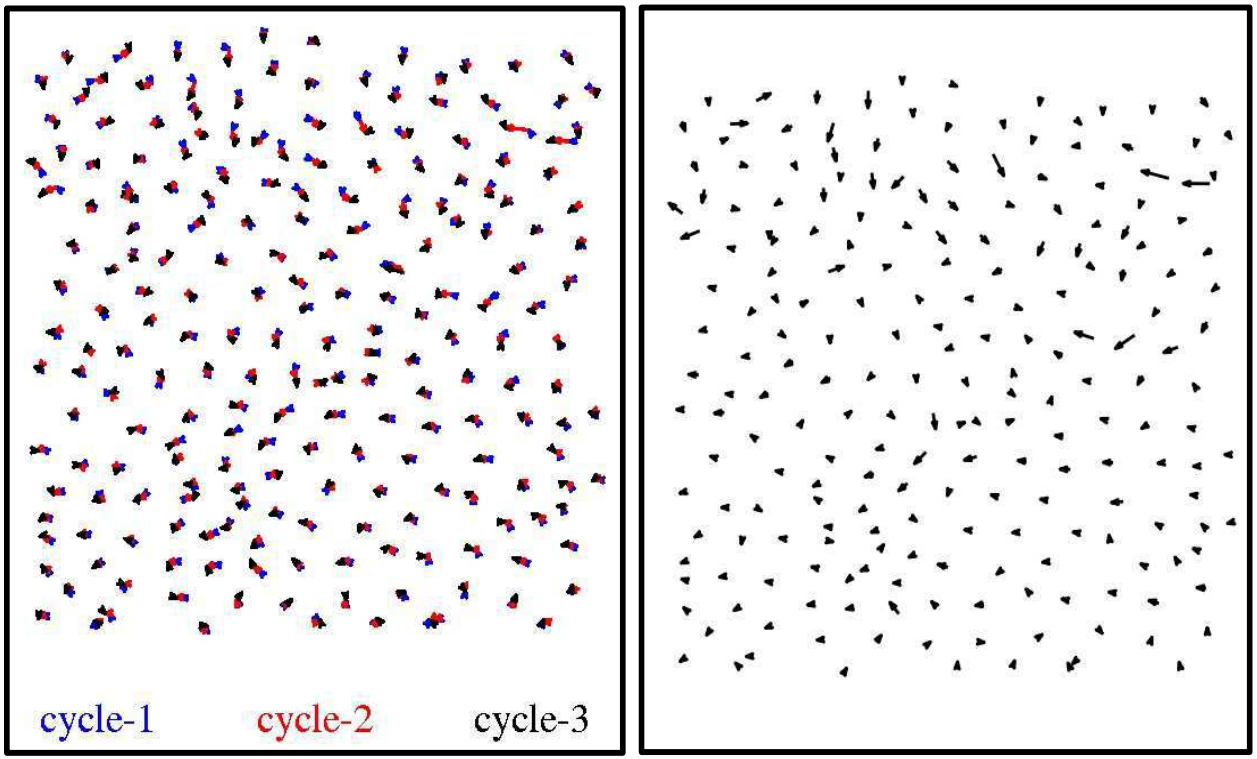

Figure 18: Streaklines for soft material from simulation. Left: Individual distances that particles moved at each cycle. Right: Cumulative distances of the individual distances of the particles at the end of the last cycle.

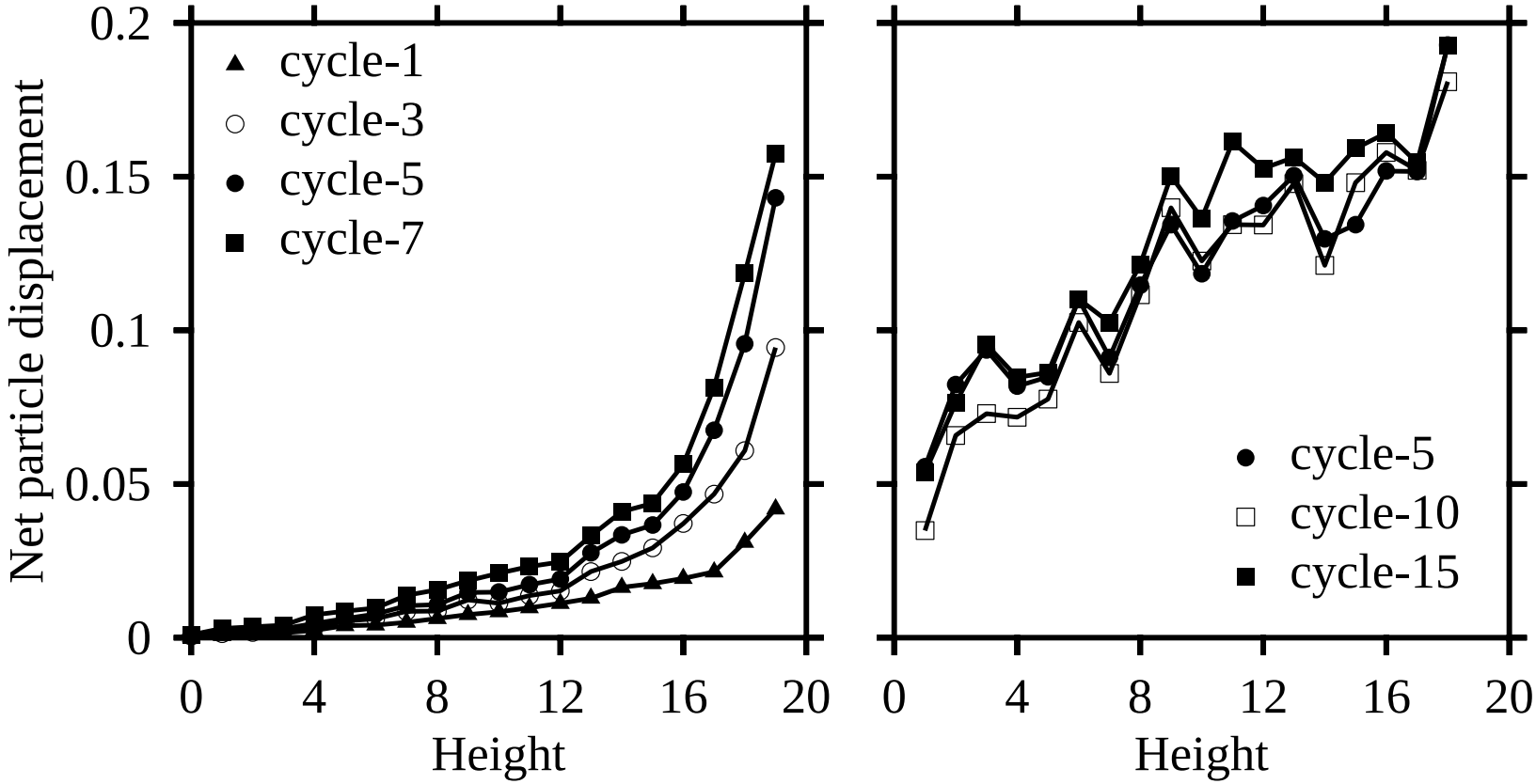

Figure 19: Quantitative results of the particle mobility in the packed beds. Left: Simulation. Right: Experiment

3.4.3 Comparison to Experiment

In this section, we investigated the consolidation that takes place for packed beds during the thermal cycling process. We have tested mono-disperse materials consisting of steel and cellulose acetate. As explained in Section 3.3, we constructed a relationship between the solid fraction and the apparent height to represent our compaction results since the apparent height of a particular bed can easily be measured experimentally. With the assumption that all temperature measurements were always taken at the same bed temperature, we can say that the solid fraction is the reciprocal of the apparent height. This assumption is only valid when each cycle (heating or cooling step) is run for a very long time. To illustrate, we keep the oven under the heating cycle for more than 15 hours until the temperature of the bed is the same as the temperature of the oven (steady state), and then we do the same thing during the cooling process. By the end of the first cycle (cooling), the bed apparent height is no longer a function of temperature since we let the bed equilibrate for a very long time until it reaches ambient temperature. Hence, we can measure the solid fraction of the bed based on the apparent height information.

The results in Figure 20 show an increase in the solid fraction for both steel and cellulose acetate. Steel and cellulose acetate are essentially showing similar increase in the solid fraction. We believe that the difference between the thermal expansion of the grains and the container could cause the change in solid fraction. However, our simulations - which do not have walls - show the same trend although with a smaller change in packing. This indicates that the thermal expansion of the walls may increase the degree of packing but it is not necessary to achieve a change in packing fraction. In fact, the expansion and contraction of the grains alone is enough to achieve bed compaction. The process is cycled at $\Delta T = 40°C$ to make sure that the cellulose acetate glass transition temperature, which is about $76°C$, is not exceeded.

On the other hand, in order to directly compare with the simulation, we decided to run an experiment with a shorter time evolution for the cycles, where the bed does not equilibrate at half cycles to the set point of temperature. For this experiment, we operated the thermal cycling procedures at $\Delta T = 40°C$. In this case, the bed does not get heated or cooled all

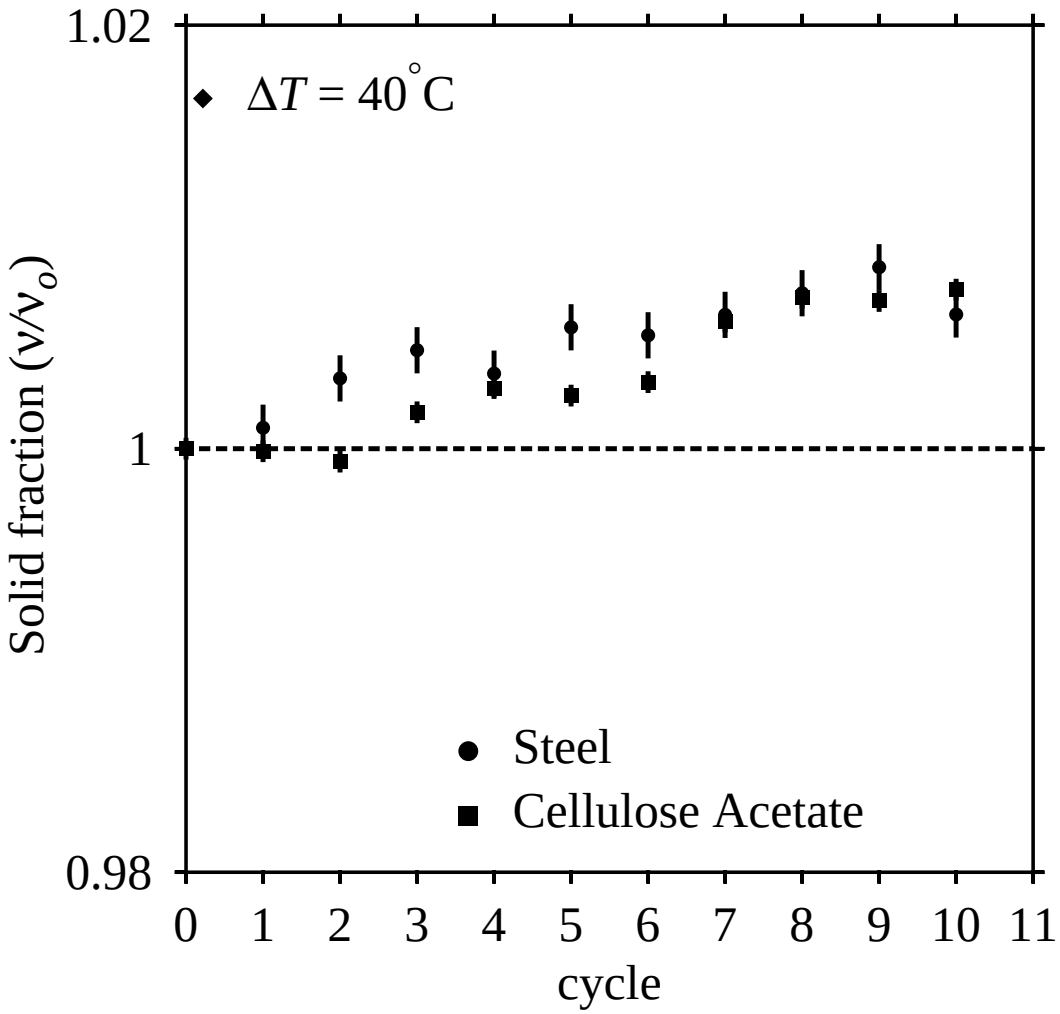

Figure 20: Change in solid fraction for steel and cellulose acetate with long time evolution thermal cycling at $\Delta T = 40°C$

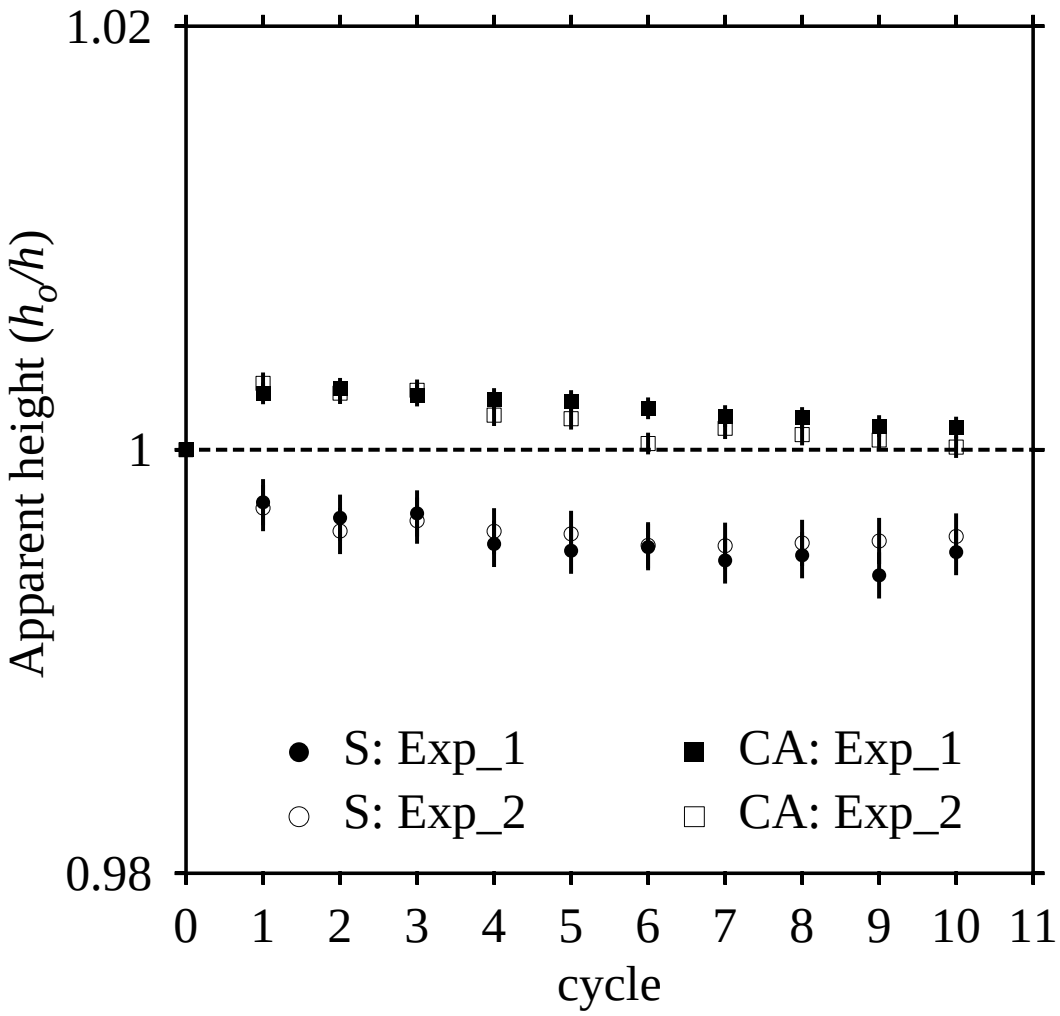

Figure 21: Change in apparent height for steel and cellulose acetate with short time evolution thermal cycling (about 1 hour) at $\Delta T = 40°C$

the way to the steady state temperature at the end of each half cycle. Hence, we will not be able to show the results in terms of the solid fraction. Instead, we will be using the apparent height as a measure of the compaction to show our results.

Figure 21 illustrates how the steel compacts immediately as its apparent height decreases rapidly after the initial cycle. The cellulose acetate apparent height expands during the first cycle, where the total volume of the bed increases, then starts to decrease in the following cycles. The reason it expands first is that the bed temperature has not reached a steady state yet. So, as it is ramping up to a steady state temperature, we see the bed starts to contract and consolidation is expected to occur for later cycles. The data points in Figure 21 represent the results of the experiment for two different trials in order to show the reproducibility of the results, and the vertical error bars display one standard deviation in either direction. These vertical error bars are representative of the measurement error that we obtain by analyzing one image five times.

In Figure 22, we can see how the mean temperature of the bed starts expanding during the first two cycles, and then it becomes steady along with the increase of the cycle numbers. This indicates that consolidations start to take place when the bed reaches a steady state mean temperature.

3.4.4 Thermal Cycling for Large Bed Sizes

The simulations discussed in Section 3.4.1 were performed for small bed sizes. We are interested to investigate more realistic bed sizes (larger ones), such as those existing in industrial processes, to simulate some natural phenomena such as dunes, beach sand, and the formation of lunar regolith. We determined the extent of what we would consider to be a large bed by measuring computationally the effective thermal diffusivity of the smaller beds, and use penetration theory to estimate how large the bed should be to be effectively infinitely large yet still be manageable computationally. Lateral periodic conditions are used in the large bed simulation with vertical heating from the top wall particles that have essentially no confining load. Figure 23 shows a snapshot of the large bed simulation during the heating cycle.

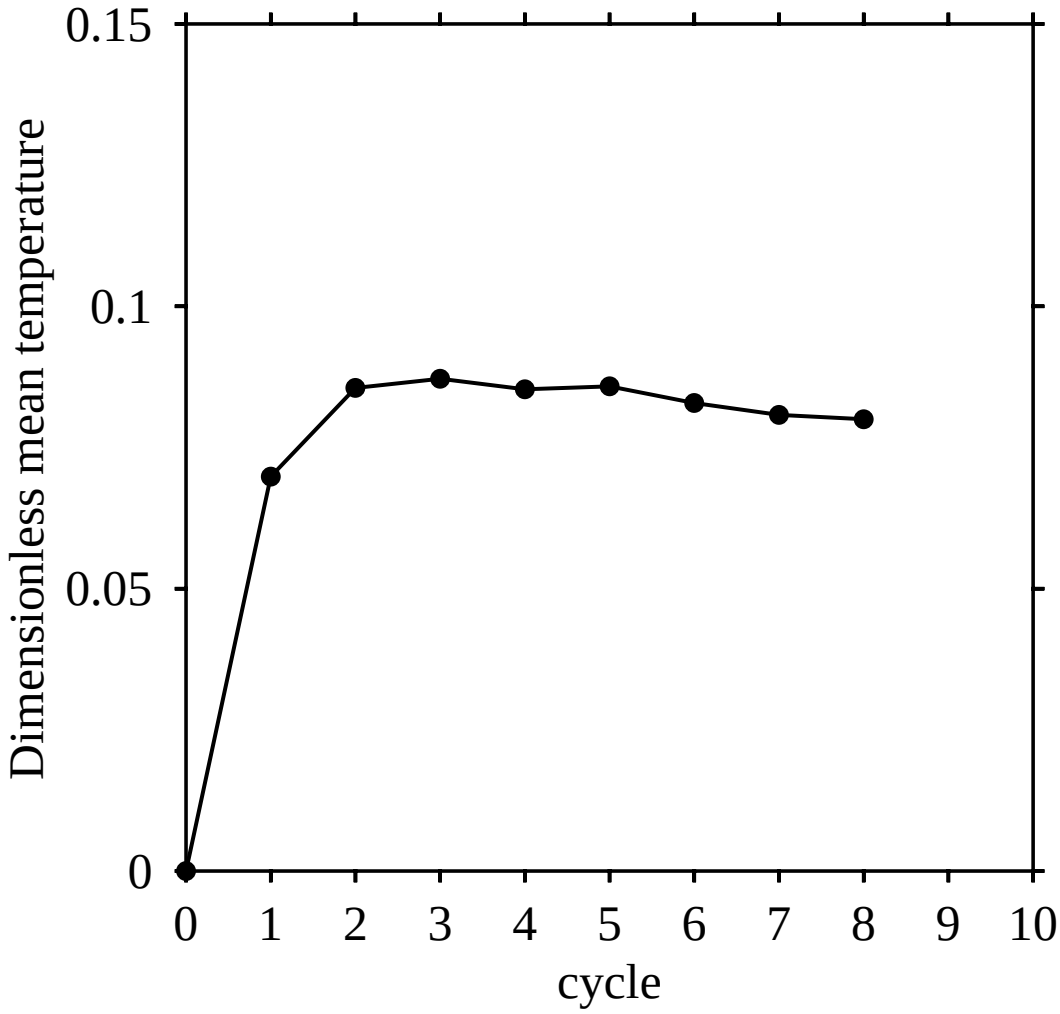

Figure 22: Dimensionless mean temperature as a function of the cycle number

The results from the large bed simulation have a similar trend to those observed for the small bed simulations and short time experiments. The solid fraction increases with the increase in number of cycles, as shown in Figure 24. It takes a fairly large number of cycles to show a change in solid fraction of about 0.5%, which indicates that consolidation can occur over a period of long time. In Figure 25, the apparent height for the large bed shows a similar qualitative trend to that shown in Figure 15 and Figure 21 even though the heating and cooling in the simulation and experiment are not performed in the same fashion, and the bed sizes are not the same. The bed height increases in the early cycles as the mean temperature of the bed reaches a steady state, then the bed starts to consolidate as the number of cycles increases. Again, a very small compaction resulted after a long period of thermal cycling time even in the absence of confining side walls.

3.4.4.1 Unsteady Conduction Problem In transient conduction, temperature is a function of both time and spatial coordinates. If we assume constant thermal conductivity, no heat generation, and negligible temperature variations in the x and z directions, the governing equation for the transient heat conduction problem is according to Fourier's equation:

$$\frac{\partial T}{\partial t} = \alpha_T \frac{\partial^2 T}{\partial y^2} \tag{3.3}$$

where α_T is the thermal diffusivity of the material. In the present case, we use the constant surface temperature boundary condition approach to determine the temperature response in the bed in order to estimate the bed height in our simulation. We fit the temperature response from the analytical solution with that from the small size bed simulation by changing the thermal diffusivity value (α_T). Once we obtain the best fit, the corresponding value of α_T is taken to estimate the large bed size using the penetration theory.

We consider different constant surface temperature boundary condition at the top and bottom with unequal surface temperatures. The separation of variables method is used to find the solution for the temperature response of the small bed. Then, we fit, using the method of Residual Sum of the Squared (RSS), the bed temperature response in order to obtain the thermal diffusivity (α) of our bed. We then use that thermal diffusivity and

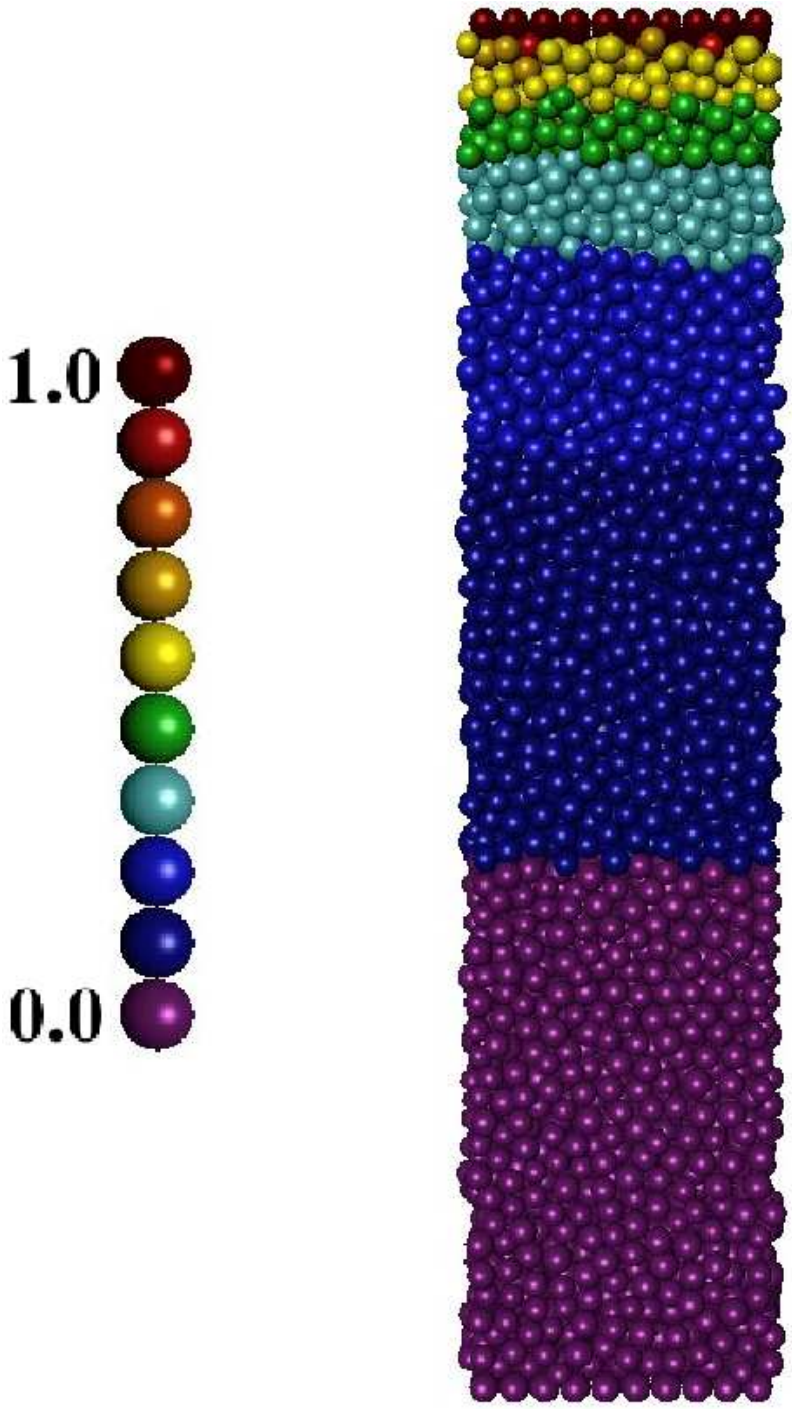

Figure 23: Snapshot of the large bed simulation domain with the vertical heating from the top wall during thermal cycling process. The scale shown is a representation of the dimensionless temperatures

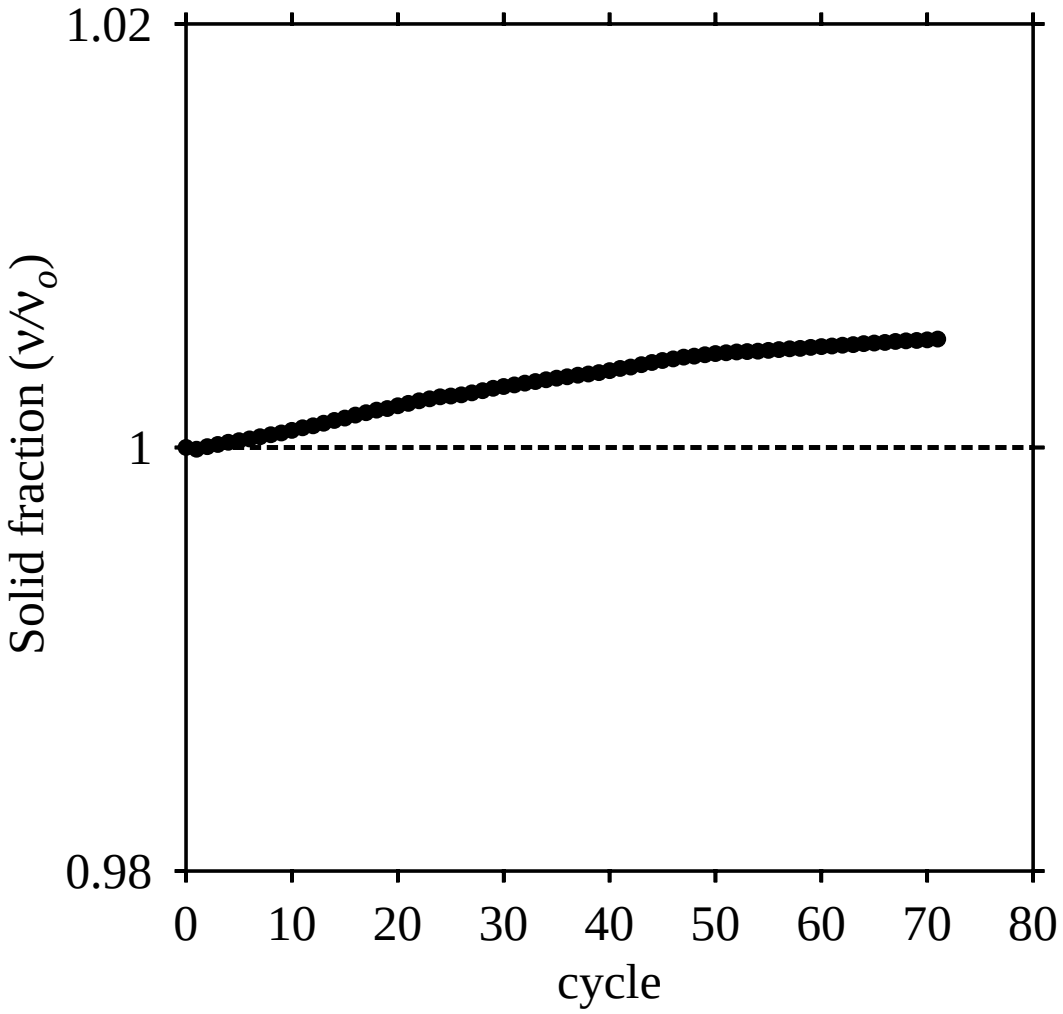

Figure 24: Solid fraction for the large bed as a function of the cycle number in 3D simulation

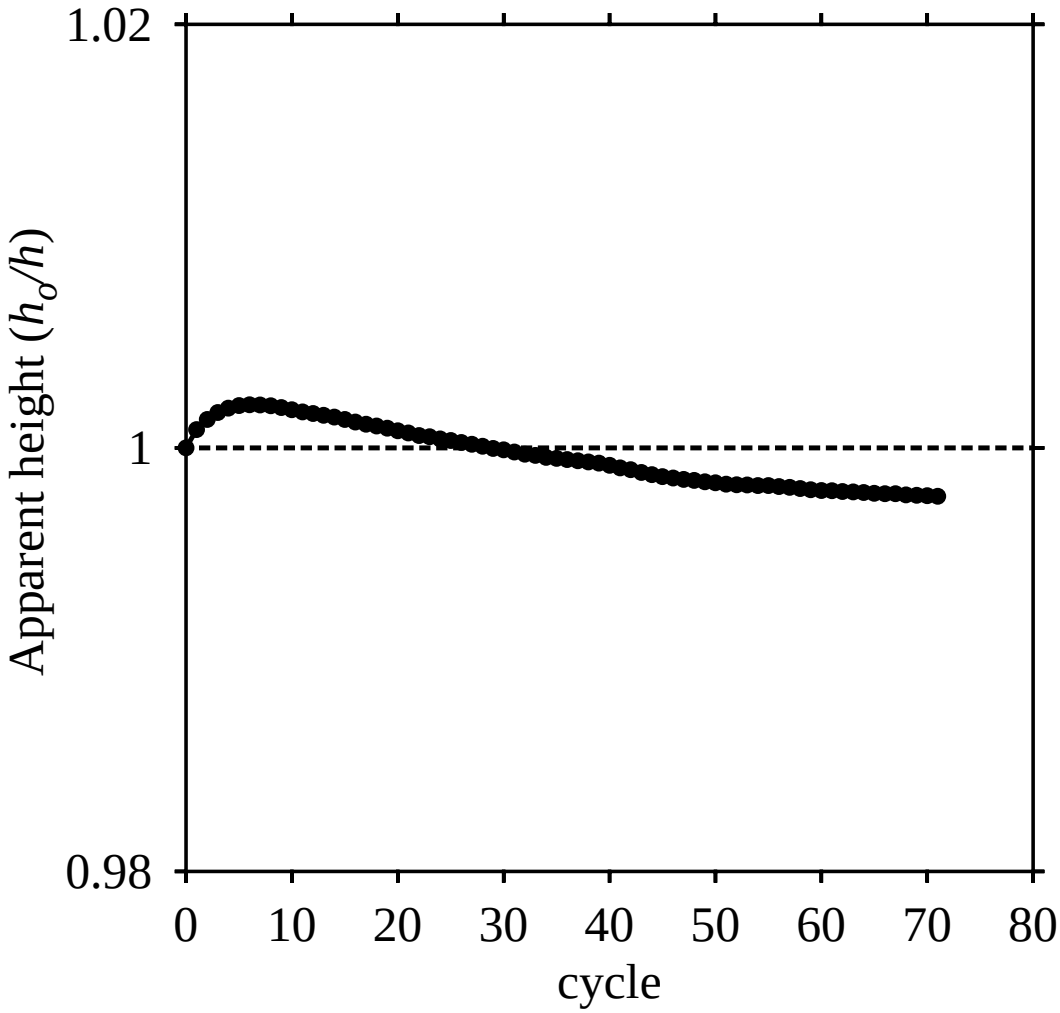

Figure 25: Apparent height for the large bed as a function of the cycle number in 3D simulation

penetration theory in order to estimate the size of a bed that would allow us to assume a semi-infinite temperature response for our large bed. Here we define a dimensionless temperature (Θ) on both boundaries with homogenous boundary conditions to obtain an eigenvalue problem. This is accomplished by reducing the problem to the superposition of a steady and transient problem as follows:

$$T(y,t) = T_1(y) + T_2(y,t) \tag{3.4}$$

where temperatures T_1 and T_2 represent the steady and unsteady parts, respectively. Since the bed is initially at a uniform temperature T_o, the governing differential equation for $T(y,t)$ is solved subject to the following initial condition:

$$t = 0: \qquad T(y,0) = T_o \tag{3.5}$$

The top side of the bed is suddenly raised to temperature T_s at time zero and held at that value. The appropriate two boundary conditions are then:

$$y = 0: \qquad T(0,t) = T_o \ , \qquad y = L: \qquad T(L,t) = T_s \tag{3.6}$$

Solving the steady state part of the governing equation ($\alpha_T \frac{\partial^2 T}{\partial y^2} = 0$) with the steady state boundary conditions results in the following:

$$T_1(y) = (T_s - T_o)\frac{y}{L} + T_o \tag{3.7}$$

Equation 3.7 can be written in dimensionless parameters as follow

$$\Theta_1(y) = \xi \tag{3.8}$$

where $\Theta_1 = (T - T_o)/(T_s - T_o)$ is the dimensionless temperature, and $\xi = y/L$ is the dimensionless length. Now, we substitute Equation 3.4 into the governing Equation 3.3 and we get

$$\frac{\partial T_2}{\partial t} = \alpha_T \frac{\partial^2 T_2}{\partial y^2} \tag{3.9}$$

In order to get homogeneous boundary conditions for the transient (unsteady) part, the initial condition is derived as:

$$t = 0 : \qquad T_2(y, 0) = -\frac{y}{L}(T_s - T_o) \tag{3.10}$$

Now it is convenient to use dimensionless variables to solve the transient part of the governing equation. So we let

$$\xi = \frac{x}{L} \ , \qquad \tau = \frac{\alpha_T t}{L^2} \tag{3.11}$$

Hence, our unsteady dimensionless Equation 3.9 becomes:

$$\frac{\partial T_2}{\partial \tau} = \frac{\partial^2 T_2}{\partial \xi^2} \tag{3.12}$$

where the corresponding homogenous boundary condition can be stated as

$$T_2(0, \tau) = 0 \ , \qquad T_2(1, \tau) = 0 \tag{3.13}$$

The initial condition remains the same as stated in Equation 3.10. Using the separation of variables method, we can solve both the spatial and the temporal parts of the unsteady eigenvalue problem. The final expression for the transient part (T_2) should be

$$\frac{T_2(\xi, \tau)}{T_s - T_o} = 2 \sum_{n=1}^{\infty} \frac{cos(n\pi) sin(n\pi\xi)}{n\pi} e^{-n^2\pi^2\tau} \tag{3.14}$$

The full solution of the problem can be expressed by combining the steady state solution Equation 3.7 and the transient solution Equation 3.14 to get

$$\Theta(\xi, \tau) = \xi + 2 \sum_{n=1}^{\infty} \frac{cos(n\pi) sin(n\pi\xi)}{n\pi} e^{-n^2\pi^2\tau} \tag{3.15}$$

where $\xi = y/L$ is the dimensionless length, and $\tau = \alpha_T t/L^2$ is the dimensionless time. In Equation 3.15, different τ values are used so that we can fit our temperature response with that obtained from the small size simulation results. The thermal diffusivity value (α_T) of the bed with the best temperature fit is selected to estimate the new simulation bed height using the concept of penetration theory for a semi-infinite bed. For a semi-infinite bed, the

expected temperature profile should be a function of time as heat penetrates into the bed. We can arbitrarily define a penetration depth that is a function of both time t and thermal diffusivity α_T, where the penetration increases with the increase in α_T at a given time. For the temperature profile in a semi-infinite bed to be a function of single variable, distance into the bed should be scaled to the penetration depth as follow:

$$\eta = \frac{L/2}{2\sqrt{\alpha_T t}} \tag{3.16}$$

where η is a dimensionless spatial coordinate called similarity variable, $L/2$ represents the penetration length half way into the bed (we use L as the bed depth), and t is the simulation time at the end of the heating cycle. The dimensionless temperature response in a semi-infinite bed with a step change in surface temperature can be represented by Equation 3.17, which allow us to know how far the temperature penetration can occur into the bed, and that the temperature should be almost zero at half depth.

$$\Theta = erfc\ \frac{L/2}{2\sqrt{\alpha_T t}} \tag{3.17}$$

The α_T values that gave the best fit, using the method of Residual Sum of the Squared (RSS), was determined to be $1.14\times10^{-6} m^2/s$. This method provides a reasonable simulation depth of the bed which yields realistic results yet be manageable computationally for the simulation of many natural phenomena such as lunar regolith formation.

3.5 CONCLUSIONS

In this chapter, we studied the behavior of granular material undergoing thermal cycling. We have demonstrated that the geometry of the particle bed has a major impact on the change in solid fraction and the apparent height. The 2D and 3D simulations are qualitatively different whereas the two types of confining loads are quantitatively different. We reported quantitative and qualitative measurements of the mobility of particle undergoing thermal cycling process both in simulations and experiments. In order to simulate some natural phenomena, a reasonable simulation depth of the bed, that will yield results yet still be manageable computationally, was determined. Penetration theory was used to estimate the required bed height. We have showed that TPD technique is a great tool for simulating granular packings with thermal expansion. It offers insights into the behavior of granular media undergoing thermal cycling. It was concluded that during thermal cycling, the thermal expansion of just the granular material can be responsible for achieving consolidation for small and large beds and without the presence of confining walls. Lateral periodic conditions were used for all simulations in this work.

4.0 FLOW OF GRANULAR MATERIALS

4.1 INTRODUCTION

The knowledge of flows of granular materials has increased significantly over recent years due to the major contributions from experiments, numerical simulations, and theory by many researchers. A granular solid can flow like fluid under the correct conditions [7]. The first recorded mention of granular flows was by the famous poet and natural philosopher in ancient Rome, Lucretius (ca. 9855 B.C.) who wrote "One can scoop up poppy seeds with a ladle as easily as if they were water and, when dipping the ladle, the seeds flow in a continuous stream" [160]. Earlier studies in the area of granular flow were focused on laboratory experiments, where the results are macroscopic and used to validate continuum theories or support continuum modeling [90]. However, the information to capture the microscopic properties of granular flow were not possible to obtain via experimental techniques. This issue led researchers to rely on computational modeling of particulate flows as an alternative or supplement to experiments. DEM simulations are capable of modeling highly complex systems by providing and analyzing both macroscopic and microscopic characteristics of a granular system. DEM validation is necessary in order for this technique to be widely accepted by industry.

Many researchers used DEM simulations in their work but they lack validation with physical tests. In this Chapter, we investigate a DEM validation study using detailed comparison of experimental and simulation results in a horizontally-aligned annular shear cell. In particular, we compare results that employ a number of differing parameter values and contact mechanics force forms. In both experiments and simulations, we measure three different profiles: solid fraction profiles, tangential velocity profiles, and granular temperature

distributions. We comment on the level of computational fidelity (robustness of the observations) necessary to capture both qualitative and quantitative aspects of the experimental flow.

4.2 EXPERIMENTAL SETUP AND PROCEDURES

4.2.1 Granular Shear Cell

The geometry of interest in this study, as shown in Figure 26, is a horizontally-aligned annular shear cell where the direction of gravity is into the page with a thickness in the gravity direction roughly equal to one particle diameter. It has an aluminum frame with the bottom surface (base) made from anodized aluminum such that the granules roll on it and the top confining surface (lid) are made from a transparent smooth Plexiglas so that the dynamic behavior of the granular flow can be observed. In this study, we used an anodized aluminum base rather than a Plexiglass base, to mitigate the large build-up of static electric charge that occurs during the trial runs between the cellulose acetate polymer beads and the top and bottom surfaces. More details on predictive explanation for the charging of granular materials in collisional flows can be found in [161]. The granular shear cell (GSC) used for the study of granular flow properties, was fabricated with an outer stationary ring and an inner rotating wheel with a prescribed roughness. The radii of the inner rotating wheel and outer stationary rim are 8.573 cm (3.375 in.) and 14.288 cm (5.625 in.), respectively. Thus, the gap, which is the distance between the moving wheel and outer rim, is approximately 5.715 cm (2.25 in.).

The moving wheel is attached to a 1 / 16 hp motor capable of achieving constant rotational speeds of approximately 53 – 280 rpm, which corresponds to linear velocities of 0.55 – 2.89 m / s. The granules are made of cellulose acetate - grade 3 balls (from Engineering Laboratories Inc.) with Rockwell R hardness and 33 MPa yield strength. The diameter of the spherical granules in the base case is 0.485 cm (0.191 in.). The shear gap in the base case is filled with an area solid fraction of 0.71, which means that approximately 71% of the

overall gap area (when viewed from above) is filled with the granules during operation. While the Granular Shear Cell (GSC) was built for a monolayer of granules, the spacing between the Plexiglas lid and the anodized aluminum base is 0.794 cm (0.313 in.), which provides for a slight gap such that the granules (0.485 cm (0.191 in.) in diameter) are not compressed between the base and the lid. Extensive details on the dimensions and parameters of the shear cell were reported in the work of Jasti and Higgs [13]. A high-speed camera was used to record the GSC trials.

In literature the roughness factor (R) is interpreted as (1) The fraction of lateral momentum transferred to the granular flow by the walls [150] and (2) The fractional of granules that fit exactly between the cylindrical wall disks [151]. The roughness factor can be interpreted qualitatively, as with the first definition, or it can be defined quantitatively as with the second definition. We define it quantitatively based on Jenkins and Richmann's description (2) above, so that the roughness factor is the fraction of a particle's diameter which can fit between adjacent particles along the wheel's outer edge. More details can be found in [13]. Accommodation of particles at greater separation than d_p or a smooth surface might be accomplished using the interpretation in (1) above.

In our work, the inner rotating wheel is given a macroscopic roughness factor R (see Figure 27) by affixing granules which create protruding hemispheres about the wheel's periphery. The roughness factor R, similar but not identical to that of Jenkins and Richman [151], varies as $0 \leq \mathrm{R} \leq 1$, where $\mathrm{R} = 0$ corresponds to a fairly smooth surface and $\mathrm{R} = 1$ corresponds to a very rough surface. On the inner wheel, $\mathrm{R} = 0$ corresponds to a wheel with protruding hemispheres positioned adjacent to each other, whereas R=1 corresponds to the hemispheres positioned such that a gap of exactly one granule diameter d_p exists between consecutive hemispheres. This geometry is especially useful for validating Particle Dynamics simulations as the proper method for handling smooth-walled boundary conditions has been a point of concern in the literature [162]. Moreover, the method for generating the well-defined boundary can be exactly mimicked in both the experiment and simulation, that is, we can "glue" hemispheres to the moving surface in both instances.

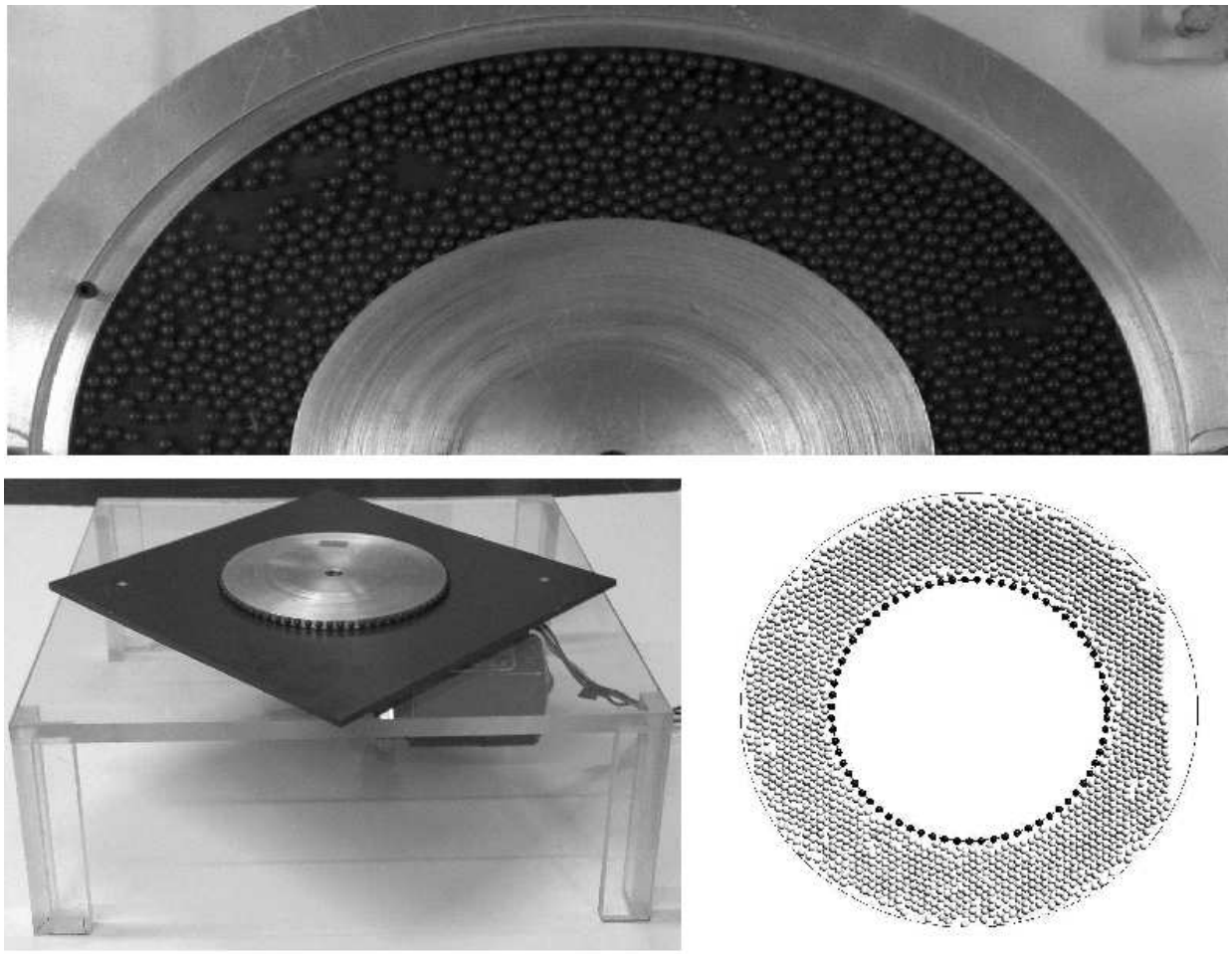

Figure 26: (Top) Section of the experimental rig with the top Plexiglas lid on and the particles spread over the gap between the inner and outer rings. (Bottom-left) An angle-view photo of experimental rig with the anodized aluminum base taken before rotation of inner ring so that the roughening hemispheres are visible. (Bottom-right) A snapshot of the computational analog of the experiment.

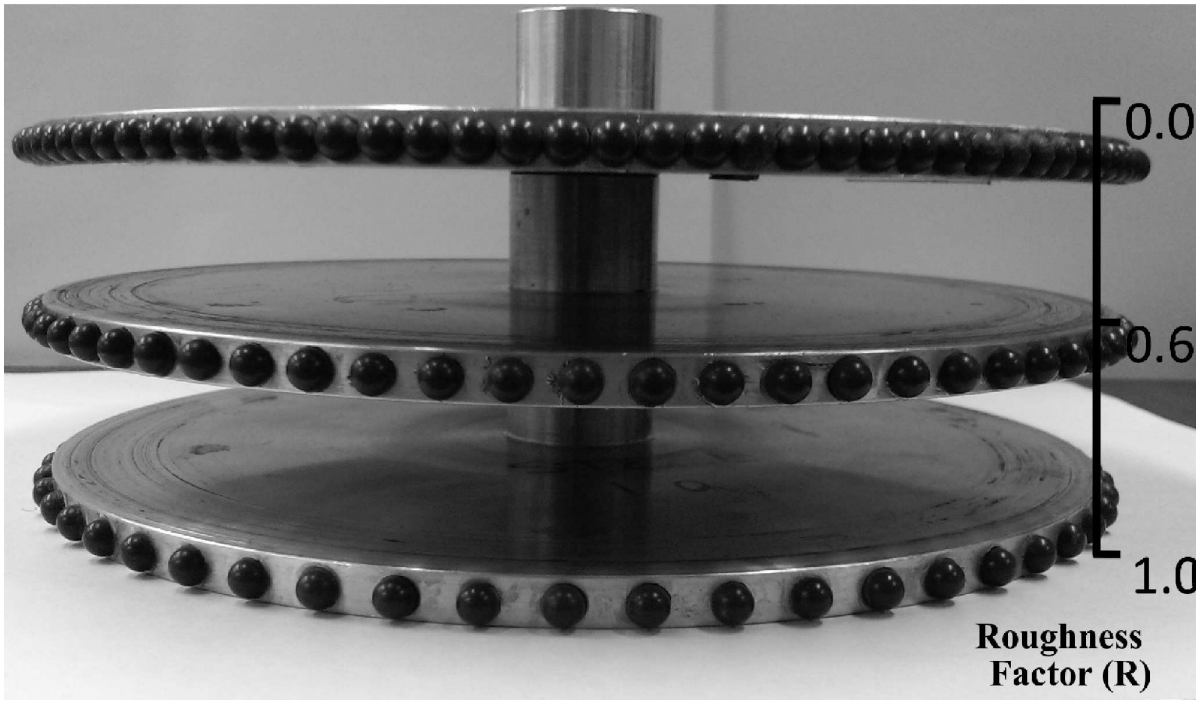

Figure 27: Side-view photo showing a range of roughened inner rings with associated values of the roughness parameter overlaid.

A digital particle tracking velocimetry (DPTV) data retrieval scheme was used to track the position of each GSC particle. A high-speed digital video camera filmed the colliding granules during the operation of the GSC. This produced a series of images, represented by the image shown in Figure 28(top-left), where a light spot is formed on each particle from the reflection of a light source.

Image processing is used to threshold the images. During this process, each particle's light spot is displayed as white, while all non- particle space (background) is displayed as black, as shown in Figure 28(top-right). Following the completion of this process, we obtains the location of each particle's centroid from their respective white spots, and tracks the motion of the centroids between consecutive frames to obtain particle velocities. Each data point was obtained as the average of 8 trials, each of which was filmed at a minimum frame rate of 1000 fps and involved analysis of all the particles within the frame of interest (inside the solid white lines shown in Figure 28(bottom)) for 450 sets of frames. These procedures serve to minimize errors associated with the white spots of the particles being off-center, as well as errors associated with insufficient frame rate or sampling [143]. In previous work from our collaborators, it was addressed that even though we are not sure that the white spot is on the centroids, this has little to no effect on the analysis. It basically has to do with the fact that the light source is hitting all the particles at the same angle. More details can be found in [17].

The local flow properties from the GSC were obtained by averaging discrete kinematic data of individual granules within the polar rectangle, which is outlined by the thick white line in Figure 28(bottom) and divided into 6 radial bins, as shown by dashed lines. In this segmentation, bin 1 is adjacent to the moving inner wheel and bin 6 is adjacent to the stationary outer wall. Each bin was approximately two particle diameters wide. The local flow properties of tangential velocity, local solid fraction, and granular temperature were then plotted as a function of normalized bin radius ($(r_i - r_w)/(r_o - r_w)$) according to the following relations. For the solid fraction in radial bin i (i.e., at position r_i), ν_i, is given as

$$\nu_i = \frac{N_i \pi d_p^2/4}{A_i}, \tag{4.1}$$

where N_i is the number of particles in bin i, d_p is the particle diameter, and A_i is the bin area. Similarly, the average tangential velocity, V_{T_i}, and granular temperature, T_i, are evaluated using

$$V_{T_i} = \frac{1}{N_i} \sum_{j=1}^{N_i} v_{T_j}, \tag{4.2}$$

$$T_i = \frac{1}{N_i} \sum_{j=1}^{N_i} \frac{1}{3} \left[\left(v_{T_j} - V_{T_i} \right)^2 + \left(v_{R_j} - V_{R_i} \right)^2 \right], \tag{4.3}$$

where v_{T_j} and v_{R_j} denote the particle (as opposed to the average) tangential and radial velocity of particle j, respectively. Note that when discussing the results, we normalize both V_{T_i} and T_i with the linear speed of the inner wheel and its square, respectively, and normalize the radial position r_i with its maximum value r_o as $((r_i - r_w)/(r_o - r_w))$ such that a normalized position of 0 corresponds to the inner, moving wheel, while 1 corresponds to the outer, stationary surface. Also, while molecular gas theory suggests the factor 1/2 should be used for calculating the granular temperature in two-dimensional flows, here we use 1/3 as traditionally seen in granular temperature relations. Error bars are shown on experimental results based on the standard deviation of the multiple trial measurements.

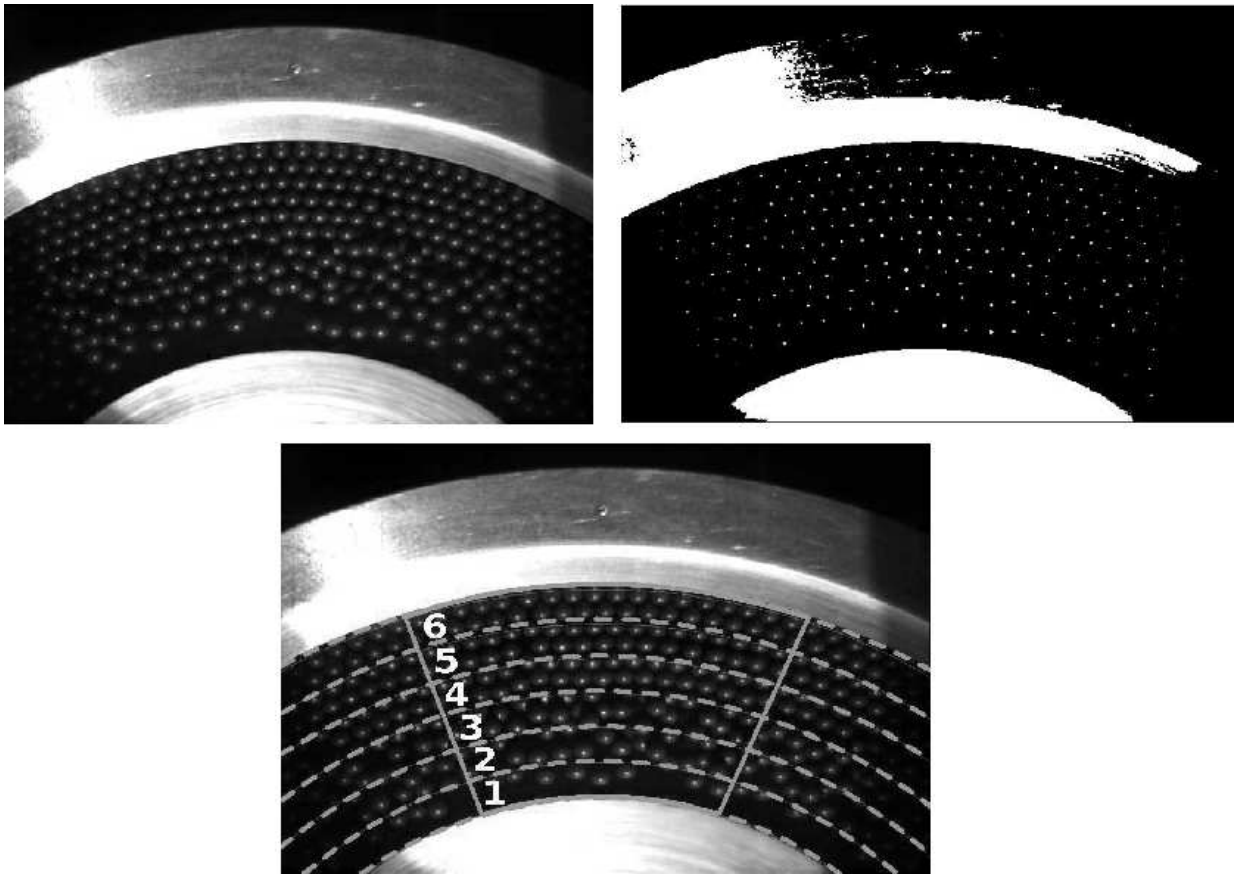

Figure 28: GSC DPTV region of interest. (Top-left) Image obtained from high speed video of the GSC. (Top-right) This shows the same image on left after thresholding has been performed. The particles appear as white, while background space is black. (Bottom) This shows the bin segmented region of interest, where data is obtained during DPTV within the polar rectangle outlined by the thick solid white line, and tabulated within six evenly divided bins across the annular gap. Bin 1 is adjacent to the rotating wheel, while bin 6 is adjacent to the stationary outer wall.

4.2.2 Drop Tests

Coefficient of restitution (COR) is a collision parameter defined as a fractional value of the ratio of post-collision to pre-collision relative velocity between two colliding objects. Hence, COR is related to kinetic energy, where an object with a COR value of one represents a perfectly elastic collision, while an object with a COR value of less than one represents an inelastic collision. At a COR value of zero, the objects effectively stop at the collision representing a perfectly inelastic collision. In order to measure the coefficient of restitution (COR) between test materials, a drop test apparatus was designed and developed. Figure 29 shows a photograph and annotated diagram of the drop test apparatus, where the labeled components (A-G) are defined as a Plexiglas casing (G), air hose and pump (E and F, respectively), base plate and plate holder (A and B, respectively), granule being tested (D), and device for holding the granule (C). The casing provides holes that fix the holding device in place at different heights. The suction force to the holding apparatus is provided by the air hose and pump, which is turned on to hold a granule in place, and then switched off to allow the granule to drop from rest. This type of set-up minimizes spin during the drop. The base plate, with which the granule collides during each trial, is secured in place at the bottom of the apparatus by a holder. Consequently, a coefficient of restitution (COR) can be obtained between the granule and plate materials. The same high speed digital video camera used for the GSC trials is utilized here to record each drop test trial.

For the experimental coefficient of restitution testing, the COR between the material of the granules filling the GSC's annular gap and each of the wheel surface materials was determined. Using the drop test apparatus from Figure 29, Cellulose Acetate granules were each dropped on an S7 tool steel plate (McMaster-Carr part number:88815K219), with Rockwell C22-C23 hardness, to experimentally determine the COR for these collisions. Typically, the material type of the granules and the plate should be the same. However, due to the unavailability of the Cellulose Acetate plate material, the S7 tool steel material is used instead. For each collision, the granules were dropped from nine different fixed heights with eight trials performed for each height using the high speed digital camera.

At the instant the granule collides with the plate, the COR between the two colliding materials is given by

$$COR = \frac{v_{R_P} - v_{R_G}}{v_{I_G} - v_{I_P}} \tag{4.4}$$

where v_{R_P}, v_{R_G}, v_{I_G}, and v_{I_P} represent the rebound velocity of the plate, the rebound velocity of the granule, the impact velocity of the granule, and the impact velocity of the plate, respectively. Since the falling granules are striking a stationary plate, the velocity of the plate remains constant at zero. This reduces Equation 4.4 to the following:

$$COR = \frac{-v_{R_G}}{v_{I_G}} = \frac{-v_R}{v_I} \tag{4.5}$$

where the rebound and impact velocity of the granule are given by v_R and v_I, respectively, and the subscript "G" is dropped in Equation 4.5 since both values now refer to those of the granule. The rebound and impact velocity of the granule can be represented using kinematics as

$$v_I = -\sqrt{2gH_I} \tag{4.6}$$

$$v_R = \sqrt{2gH_R} \tag{4.7}$$

where g is the gravitational acceleration, H_I is the initial drop height, and H_R is the maximum rebound height. Substituting Equations 4.6 and 4.7 into Equation 4.5 yields an expression for the COR in terms of the initial drop height and the maximum rebound height of the granule as follows:

$$COR = \sqrt{\frac{H_R}{H_I}} \tag{4.8}$$

An image processing technique using a high speed camera was developed and used to determine the COR between the granule and plate, by first obtaining the maximum rebound height of the granule during each trial. Since the initial drop height is known, the COR can be calculated using Equation 4.8. We performed six trials for each of the different nine fixed heights, where these trials are captured at either 1000 frames/sec or 3000 frames/sec,

which is really high for COR tests. Although the COR can be calculated using Equation 4.5 by directly obtaining impact and rebound velocities from the high speed image data, sensitivity analyses showed that being even half a pixel off when manually obtaining the location of the granule can cause differences in velocities that lead to fluctuations in the calculated COR values of up to 20%. On the other hand, these same analyses showed the height based approach to be much more robust as the fluctuations in the COR values were less than 1% when obtaining the rebound height from the high speed images.

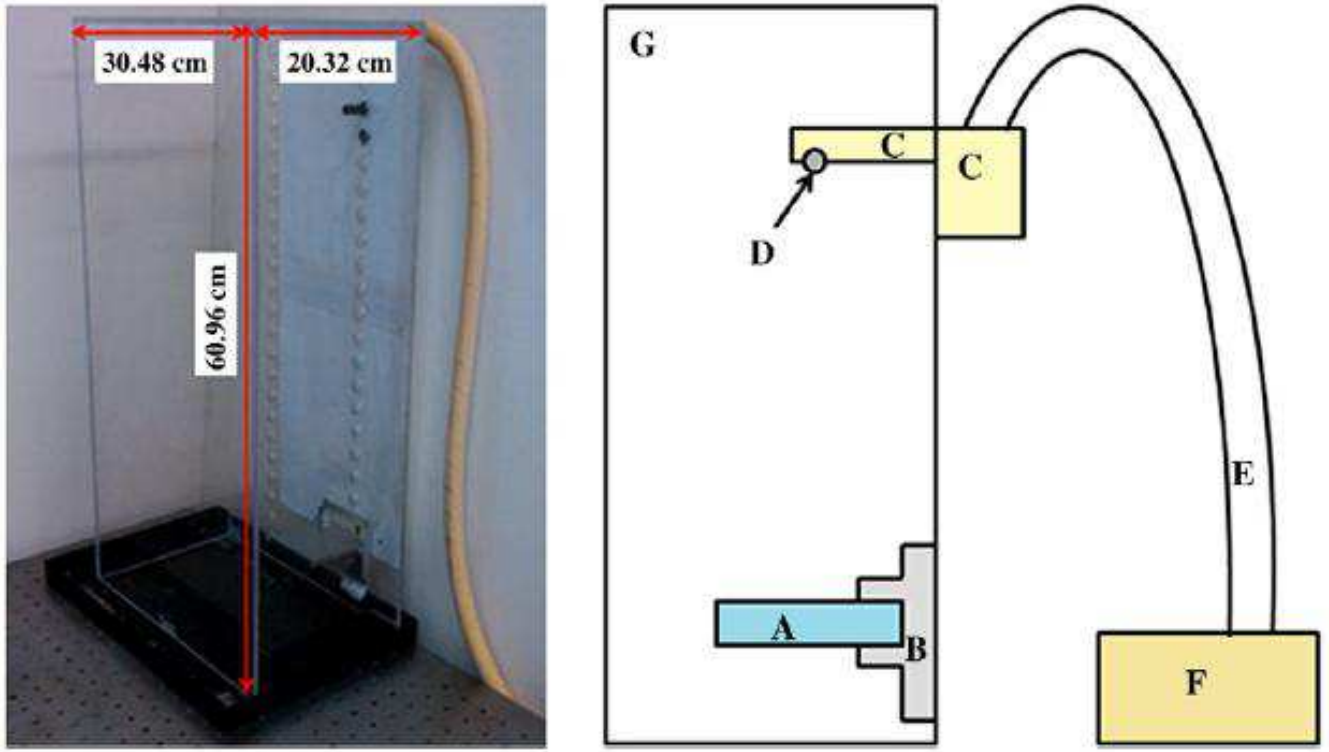

Figure 29: Left: Photograph of drop test apparatus with dimensions of the Plexiglas casing included. Right: Schematic side view of the drop test apparatus where the labels correspond to the major components. A: Plate, B: Plate holder, C: Apparatus for holding granules, D: Granule, E: Air hose, F: Air pump for proving suction, G: Plexiglas casing.

4.3 PARTICLE DYNAMICS AND MODELS

Particle dynamics simulations, known as Discrete Element Method (DEM), capture the macroscopic behavior of a particulate system where every particle is tracked individually to determine its trajectory. The global flow of the granular material is then determined by the time evolution of the particles trajectories. The particle trajectories are governed by Newton's equations of motion for every particle [27]. In a granular flow, the particles experience forces and torques due to interparticle interactions (e.g., collisions, contacts, or cohesive interactions) as well as interactions between the system and the particles (e.g., gravitational forces). This section outlines the basics of the technique as well as discussing the variety of force models and material properties used in our validation tests. As discussed previously, collisional force models range from pragmatic linear "spring and dashpot" techniques to rigorously derived contact mechanics-inspired routines [106] and we consider both ends of this spectrum in our work. Thorough descriptions of normal and tangential interaction laws were presented in Section 2.3.2, therefore only the specific models we employed will be reviewed here.

As each model is described, we will introduce the distinguishing notation used in the latter sections to denote the use of each respective model (a table of this notation is also included in Table 2). As previously discussed in Section 2.3.2, the spring-dashpot and plastic force models differ primarily in their model of energy dissipation. For the spring-dashpot model, a damping term that is proportional to the relative normal velocity between particles is linearly added to the repulsive force from Equation 2.7. The formulation for the damping term suggested by Oden and Martins [111] is chosen due to the fact that it qualitatively reproduces the experimentally observed dependence of the coefficient of restitution on impact velocity for many engineering materials. The combination of the repulsive force and this dissipation term yields what we will refer to as our *spring-dashpot* model which will be denoted with an uppercase **S**. In contrast, in our *plastic* model denoted with an uppercase **P**, dissipation is assumed to arise from the plastic deformation of the center of the contact spot. In this work, as previously discussed, the yield force, F_y, is treated in the same manner as β from the spring-dashpot model.

Table 2: Model Variations Notation

Model variation	**Option 1**	**Option 2**
Normal force model	Plastic [**P**]	Spring-dashpot [**S**]
Friction force model	Non-linear [**N**]	Linear [**L**]
Material properties	Match literature [**A**]	match experiment [**E**]
System geometry	True two dimensional [**2D**]	Exactly as experiment [**3D**]

We report results both from values of the damping parameters chosen to match the literature values of the material of interest (Cellulose acetate), denoted with **A**, as well as results where the damping parameters were obtained by fitting results to experimental drop tests, denoted with **E**. The drop tests use a vacuum release technique to drop particles in a draft-proof tower onto plates that should be of the same bulk material (Cellulose acetate). However, it should be noted that our experimental values were obtained by using a plate constructed from stainless steel rather than cellulose acetate due to the unavailability of the latter material. This suggests that our experimental results are not completely accurate and hence we performed two types of fitting (matching literature (A), and matching experiment (E)) for more thorough analysis. In Figure 30(Left), the parameter that was fit is the damping parameter of the spring dash-pot model to match literature vales of the plastic model. When matching experiment (Figure 30(Right)), the yield stress (for the plastic model) and the damping parameter (for the spring dash-pot) were fitted to the experimental values. For each model, we had only one parameter that was used for the fitting.

To better explain how the fit is done, we used the residual sum of squares (RSS) method, which is a measure of the discrepancy between the data and an estimation model. A small RSS indicates a tight fit of the model to the data. For Figure 30(Left), we use the RSS method to fit the spring dash-pot model to the plastic one. From Table 3, the best fit is when the damping parameter is chosen to be 0.000925 [kg/m s] (lowest RSS values of 0.0065) as our optimal value. Although this value may not be the global minimum, our results show that they are insensitive to choices near that global minimum. Hence, we chose

Table 3: RSS values of fitting the spring dash-pot model to the plastic model for matching literature

Damping coefficient (β) [kg/m s]	**RSS**
0.000525	0.0788
0.000925	0.0065
0.001425	0.0358

the damping parameter with value of 0.000925 [kg/m s] in all of our simulations that are related to matching literature values. When matching experiment (30(Right)), we matched both plastic and spring dash-pot models to the values from the experiment. The fitting is performed for both models (see Tables 4 and 5) and we chose the value of 0.000585 [kg/m s] (lowest RSS values of 0.0019) as our damping parameter for the spring dash-pot model. For the plastic model, the optimal value for the yield stress is chosen as 40 MPa (lowest RSS values of 0.0166). Again, our results here are insensitive to small perturbation around the global minimum value (optimal value).

Table 4: RSS values of fitting the spring dash-pot model to the experiment values for matching experiment

Damping coefficient (β) [kg/m s]	**RSS**
0.00045	0.0081
0.000585	0.0019
0.00065	0.0036

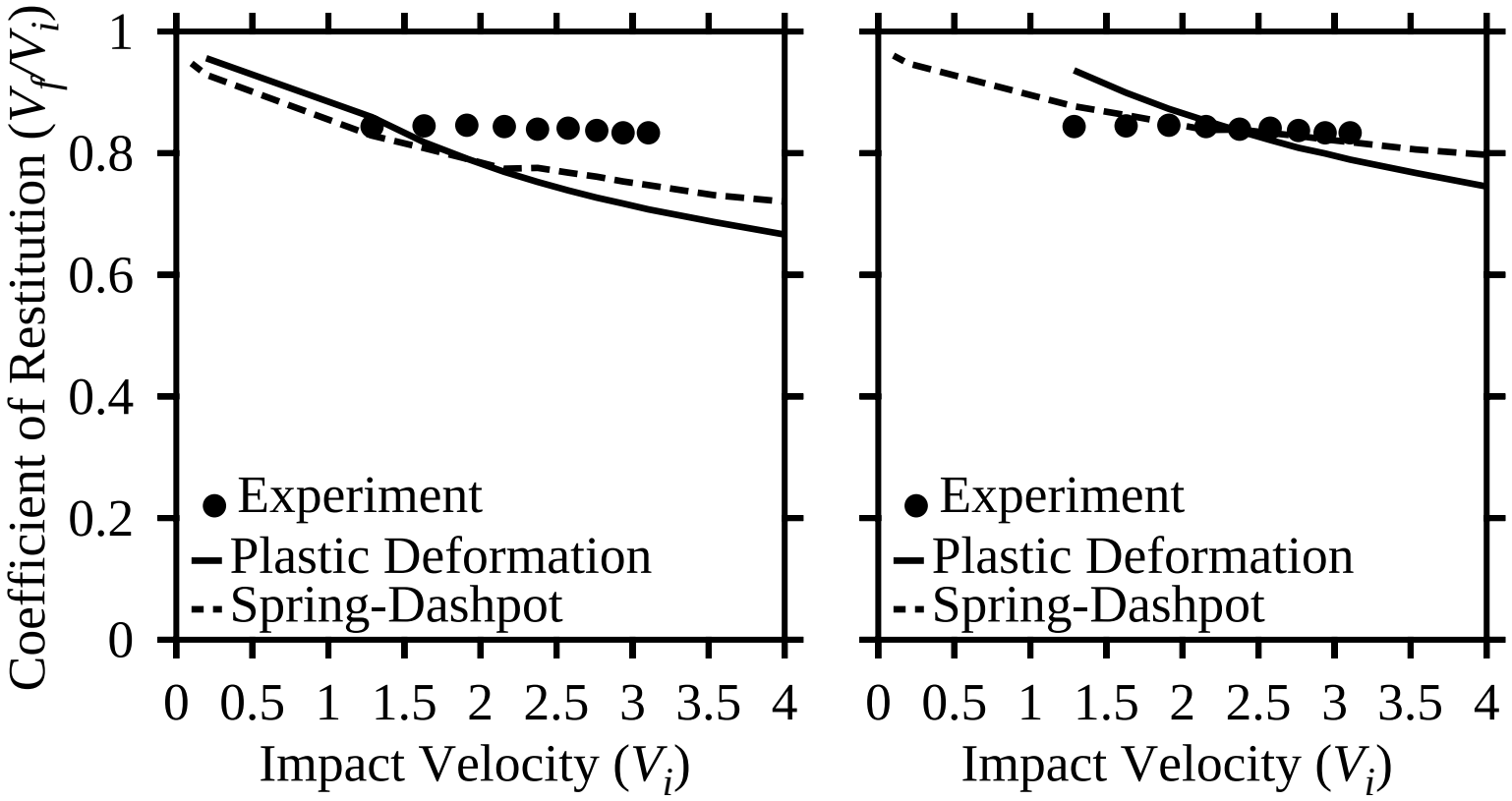

Figure 30: The ratio of relative final rebound to relative initial impact velocity (Coefficient of restitution): variation from drop tests of experimental materials (bullets) and for the plastic and spring-dashpot normal force models, with fitted damping parameters. (Left) Matching literature values. (Right) Matching Experimental values. Note that the plate material type used for the drop test is different from the beads used in this work.

Table 5: RSS values of fitting the plastic model to the experiment values for matching experiment

Yield stress [MPa]	**RSS**
37	0.0237
40	0.0166
45	0.0386

The initial height of the drops are varied to bracket the range of impact velocities relevant to the annular shear apparatus and high speed video is used to extract the coefficient of restitution from the experiments. Results from the fitted simulations and experiments are included in Figure 30.

As discussed in Section 2.3.2, in the simpler of our two friction models, the linear model denoted by an uppercase **L**, the tangential stiffness, k_t, is assumed to be constant, k_{t_o}. For this simple model, a discontinuity must be imposed in order to limit the tangential force to the Amonton's Law limit. For the more involved *nonlinear* friction force model, denoted with an uppercase **N**, two history dependent terms are included. In order to mimic an annular region of microslip at the contact edge and smoothly obey the Amonton's Law limit, the frictional stiffness, k_t, is assumed to be given by the nonlinear expressions determined following the procedure given in [91]. In both the linear and nonlinear case, the (initial/constant) tangential stiffness, k_{t_o}, is related to the normal stiffness k_n by requiring that the rate change of displacement with loading should be similar for tangential versus normal interaction so that their ratio is given according to Equation 2.20 [106].

4.3.1 Computational Geometry

We examined two separate system geometry cases. We have simulated both a true two-dimensional geometry, denoted as **2D**, as well as a geometry that exactly matched the

dimensions of the physical apparatus, where the granular shear cell has a somewhat arbitrary head space above the particles (i.e., extra space between the top and bottom plates), denoted as **3D**. In addition, we have used particle asymmetry (non-spherical shape particles) in our simulations. In other words, we have matched the particle mean size and size distribution width to the values quoted by the sphere manufacturer. In order to model particle asymmetry we have used the standard multi-particle technique [112] that has been used for adapting the use of spheres to model non-spherical shapes. In particular, we use a two particle cluster in place of each true experimental "sphere", where the center of mass mismatch between particles of the cluster is chosen to match the degree of asphericity quoted by the particle manufacturer.

4.4 RESULTS AND DISCUSSION

In this section, we present the local granular flow properties of velocity, granular temperature, and solid fraction profiles as a function of three major parameters: inner wheel rotation rate, inner wheel roughness factor and total solid fraction. As mentioned earlier, the data points represent the average of eight trials. The horizontal error bars, which are representative of the error in either GSC experimental or simulation results shown in this work, display the standard deviation of these eight trials.

4.4.1 Base Case

The "base case" of the experiment is taken as a rotation rate of 240RPM, a roughness factor of 0.6, and a total solid fraction of 0.71. Based on this case, we compare the effects of the variations in the different model parameters discussed in the previous section. In this validation study, we compare three independent experimental measurements of the local granular flow properties: solid fraction profile, tangential velocity profile, and granular temperature distribution. It should be noted that the solid faction will often exceed the maximum areal theoretical packing for a true two-dimensional geometry in both simulations

Table 6: DEM simulation parameters

Parameters	**Matching literature**	**Matching experiment**
Particle diameter [mm]	4.85 ± 0.0762	4.85 ± 0.0762
Density $[Kg/m^3]$	1280	1280
Young's modulus (E_i) [GPa]	1.5	1.5
Yield stress [MPa]	33	40
Poisson ratio(σ)	0.43	0.43
Friction coefficient (μ)	0.30	0.30
Damping coefficient (β) [kg/m s]	0.000925	0.000585

and experiments. This is because the height between the top and bottom surfaces of the GSC is slightly greater than the diameter of the cellulose acetate granules. Therefore, as in the three-dimensional geometry, some "overlap" of particles takes place within the voids between particles by occupying slightly different heights in the head space. Different simulations are performed for the base case study for different parameters. Horizontal error bar are shown for all the simulation results based on the standard deviation of the multiple trial measurements. These horizontal error bars are representative of the error for all of the simulation results shown in this chapter. Table 6 includes the parameters used in the DEM simulations. In order to quantify the comparison of the fits of all base case simulation results, we use the method of Residual Sum of the Squared (RSS) which is explained in Section 4.4.2 below.

Figure 31 shows a comparison of the different normal force models used for the base case for the three local flow properties: solid fraction, tangential velocity, and granular temperature profiles. Despite the fact that the plastic model shows a better fit when compared to the spring-dashpot model for the solid fraction profile, both models give reasonable results. While the spring-dashpot model under-predicts the tangential velocity profile, it provides good agreement for the granular temperature profile. On the other hand, the plastic model

gives a reasonable agrement for the tangential velocity profile, yet, it overpredicts the results for the granular temperature profile. In short, both force models had some sort of shortcoming in predicting one of the three local granular flow properties in the base case comparison studies. For the tangential velocity and granular temperature profiles, the sharp corners indicate the shift from the contact region to the kinetic region, where the particles are closer to the inner rotating wheel. For the Solid fraction profile, the sharp corners indicate that the maximum solid fraction actually exceed the theoretical maximum packing in 2D. The fact that the granular shear cell (GSC) design leaves a small amount of space in the third dimension, this gives the potential for granules to overlap into the third dimension, resulting in increases in the 2D solid fractions being calculated. Overlapping granules tend to be most prevalent where the shift from the kinetic to the contact region occurs (near normalized bin radius 0.6) explaining the spike in solid fraction at this location.

In Figure 32, we compare the results for the local granular flow properties for different tangential force models. For both plastic and spring-dashpot models, the choice of friction model seems to have no significant impact on the measured results of the solid fraction, velocity, and granular temperature profiles. In fact, the linear and non-linear frictional force model results overlay one another across all the three profiles. This observation may be due to the fact that the easily discriminatory region of our results corresponds to a portion of the flow where very high speed collisions occur. This likely causes frictional forces in that region to quickly reach the sliding limit so that the details of *attaining* that force are unimportant.

Next, we compare the solid fraction , velocity, and granular temperature profiles for the base case using different dissipation fitting parameters as indicated in Figure 33. We fit the damping parameter to the literature values obtained from the beads manufacturer as one option, whereas in the second option, we fit the damping parameter to the experimental values. No major variations were observed in the solid fraction profile results for all types of force models and all types of the damping parameters. For the tangential velocity profile, fitting the damping parameter to the experimental values for the plastic model improves the agreement with the literature values and shows almost an exact match to the experiment results. On the other hand, varying the fitting parameter for the spring-dashpot model has no significant impact on the tangential velocity results. Surprisingly, almost the opposite

behavior is observed when the granular temperature profile results are considered. For the plastic model, there is essentially no difference in the granular temperature profile results when using damping parameters fit to the experimental or those obtained by fitting to the literature values. However, fitting the damping parameter to the literature values for the spring-dashpot model improves the results for the granular temperature profile so that they lie within the error bars of the experimental values.

Last, in Figure 34, we vary the system characteristics for the base case using two types of geometry: two-dimensional and three-dimensional. Even though the simulation results for the solid fraction profile in the true two-dimensional geometry shows a decent match to our experimental results, we clearly observe that the tangential velocity profile for the two-dimensional case is *qualitatively* wrong. Hence, the choice of the system geometry is very critical as there is a significant slip at the immobile outer wheel. The three-dimensional results suggest an acceptable granular temperature profile, however, the results are under-predicted for the tangential velocity profile.

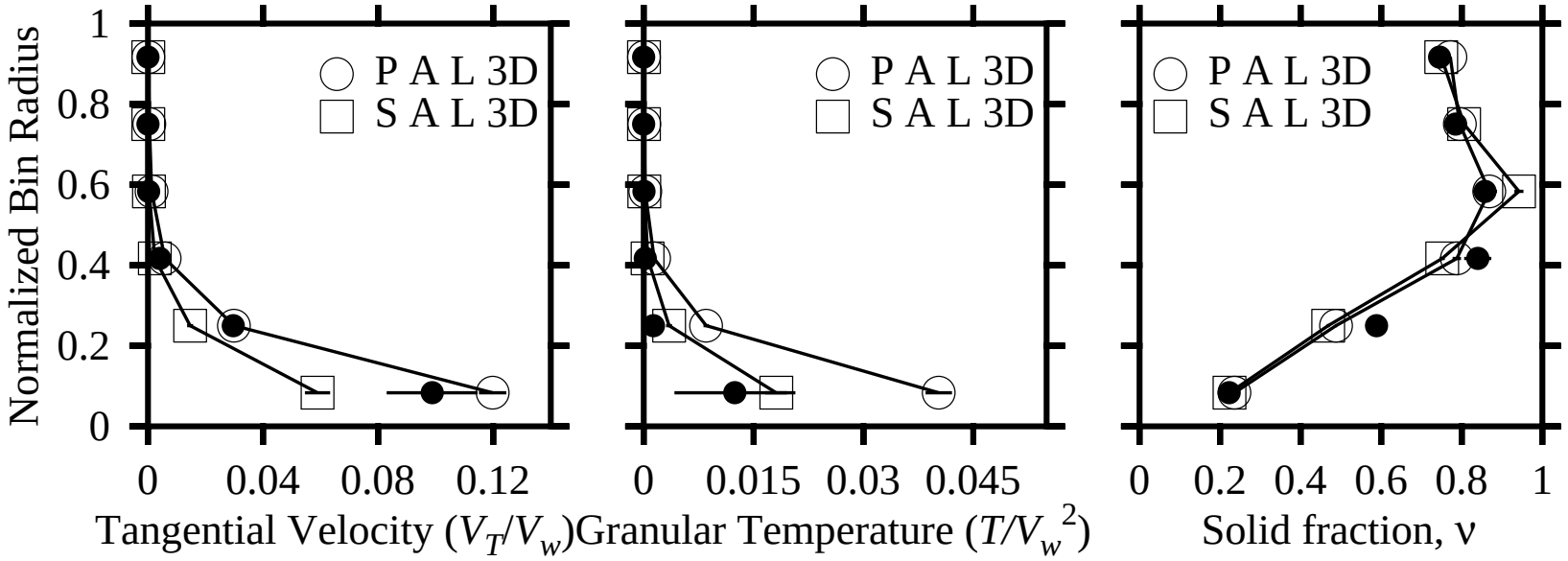

Figure 31: Comparison of experimental (solid bullets) and computational results when varying the normal force model.

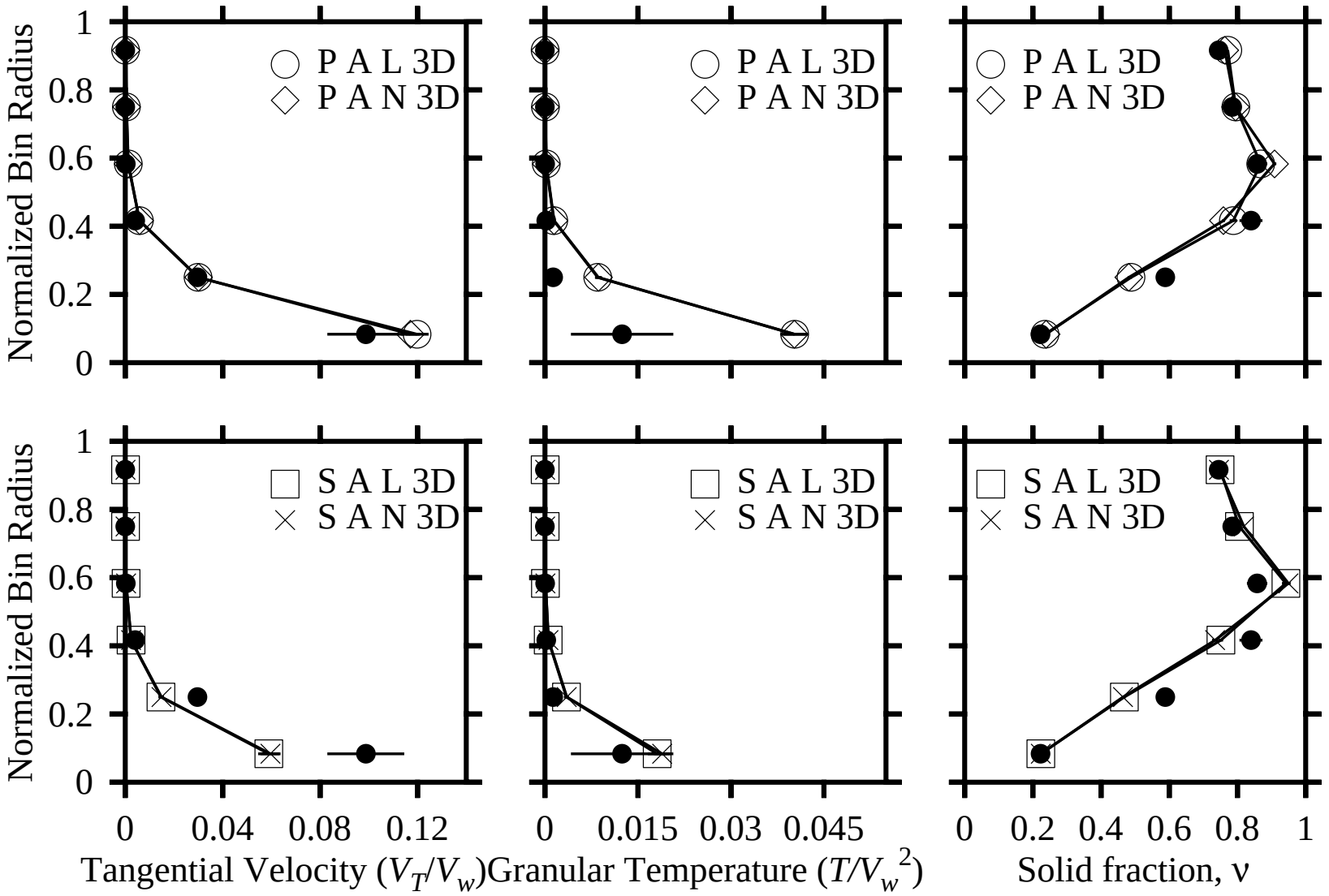

Figure 32: Comparison of experimental (solid bullets) and computational results when varying the tangential force model.

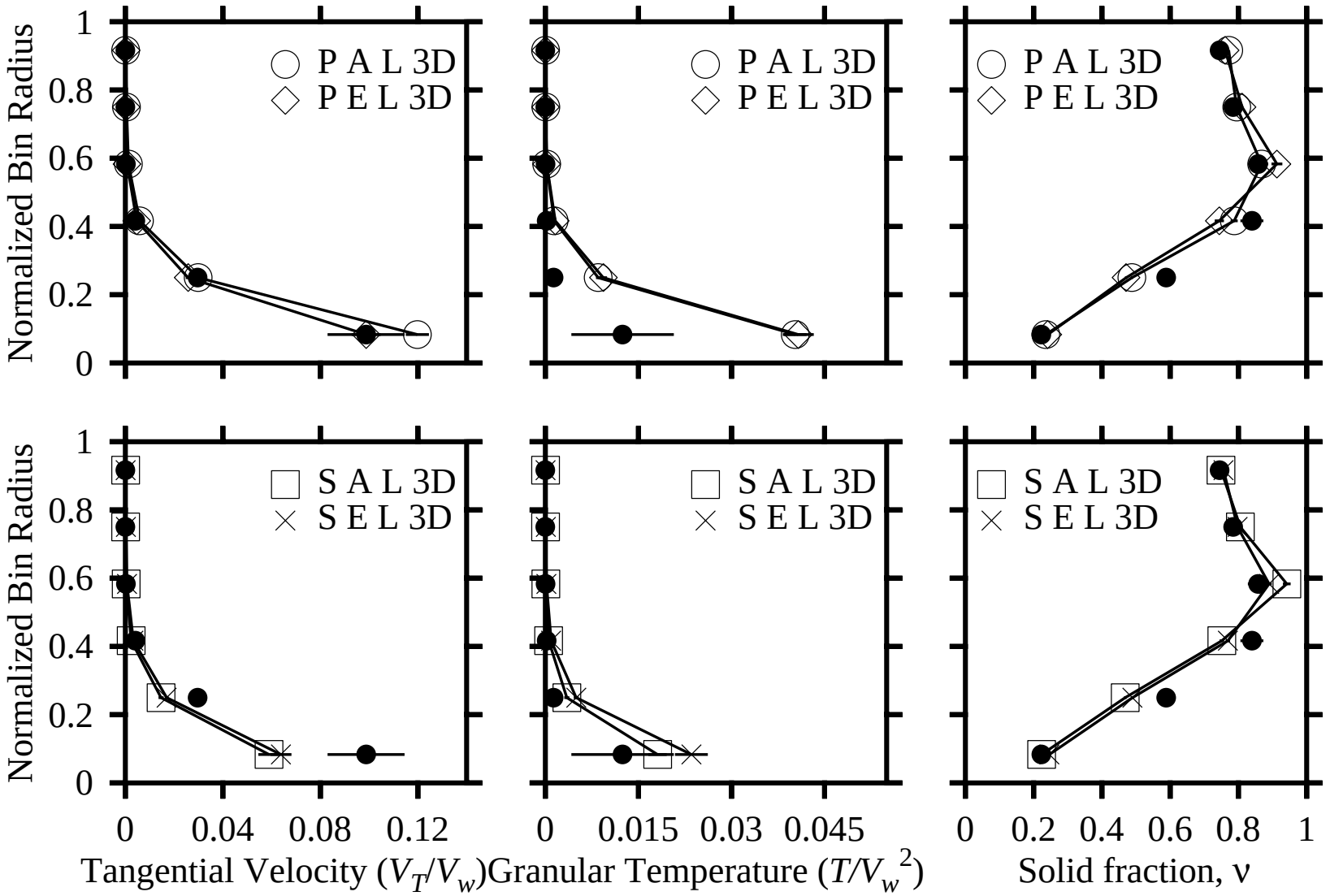

Figure 33: Comparison of experimental (solid bullets) and computational results when matching the dissipation fitting parameter to literature values (**A**) and to experimental ones (**E**).

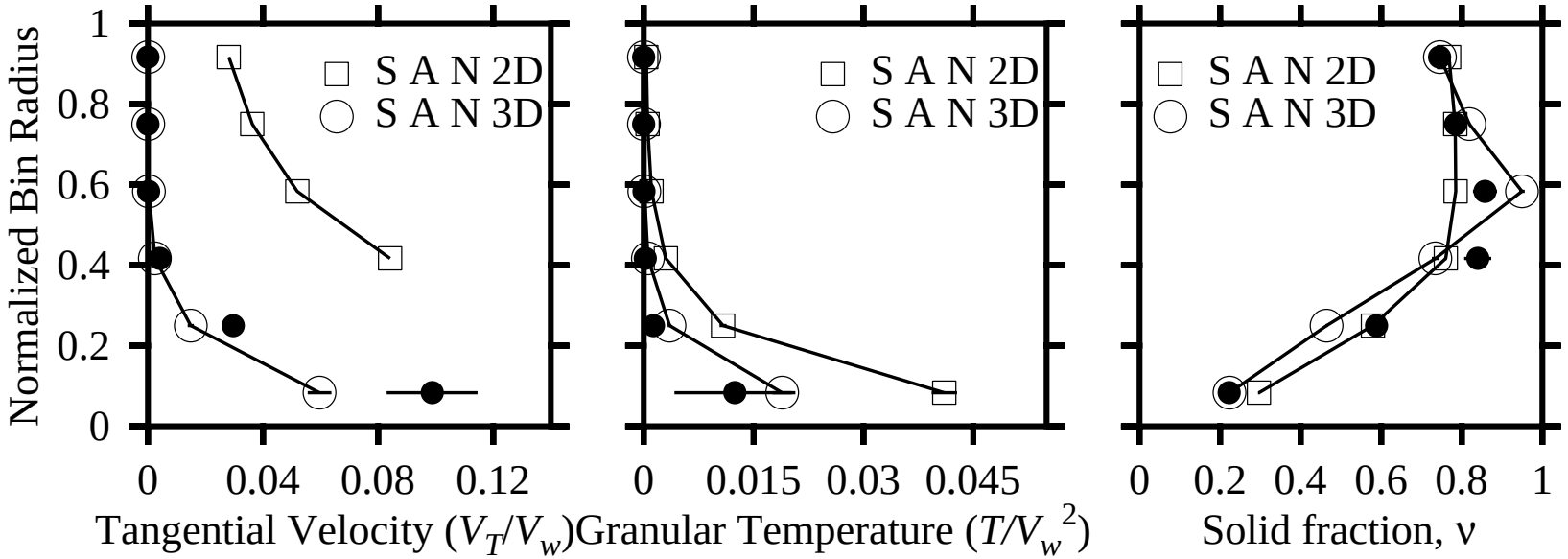

Figure 34: Comparison of experimental (solid bullets) and computational results when varying the system geometry.

4.4.2 Parametric Study

The objective of this parametric study is to examine the robustness of our DEM validation models with the experiments by changing different parameters such as the rotation rate, inner wheel roughness and the solid fraction for all the three different profiles. Our parametric study consist of testing the robustness of the fit obtained for the base case studies. We choose the "best fit" model from our computational results for the base case and compare its predictions with results from experiments that vary rotation rate (Ω), roughness factor (R), and global solid fraction (ν). For each of the two different normal force models, we choose the "best fit" model and perform a parametric study for each model.

Hence, we need to choose from each of the force models a "best fit" model to compare it with the experiments and perform two parametric studies. In order to quantify our results to estimate the best fit model, we utilized the method of Residual Sum of the Squared (RSS) which is a measure of the discrepancy between the data and an estimation model according to the following notation:

$$RSS = \sum_{i=1}^{n} \frac{1}{\sigma_i^2} \left[\left(y_i - y_{sim(i)} \right)^2 \right]. \tag{4.9}$$

where σ_i is the standard deviation for each data point from the experiments trials, y_i is i^th value of the variable to be predicted, and $y_{sim(i)}$ is the corresponding computational predicted value. A small RSS indicates a tight fit of the model to the data. The results are reported in Table 7, where we normalized the RSS values with the best fit model for the three granular flow properties (velocity, solid fraction, and granular temperature profiles) to simplify the evaluation of the data according to the following:

$$Normalized \quad RSS = \frac{RSS - RSS_{best}}{RSS_{worst} - RSS_{best}}. \tag{4.10}$$

Then, we sum the normalized RSS values that we obtain from each granular flow property as a total for the three granular flow profiles. The smaller the sum of the normalized RSS, the better is the fit. According to Table 7, we choose (**S A L 3D**) and (**P A L 3D**) as our "best fit" models for the spring-dashpot and the plastic force models, respectively.

Table 7: Normalized RSS values for the base case computational models

Plastic model		**Spring-dashpot model**	
P A L 3D	1.45	S A L 3D	0.68
P A N 3D	1.95	S A N 3D	1.07
P E L 3D	1.65	S E L 3D	1.24
P E N 3D	1.82	S E N 3D	1.73

In Figure 35, we show a parametric study varying the roughness and rotation rate of the inner wheel for the best case model **S A L 3D**. The base case model for the variation in the roughness factor shows a reasonable agreement for roughness factor R=0 in the tangential velocity and granular temperature profiles, whereas for roughness factor R=1, the agreement is not quite as good for both the tangential velocity and granular temperature profiles. For roughness factor R=0.6, we see a deviation case, where it has a decent match in the granular temperature profile but significantly underpredicts in the tangential velocity profile. The base case model gave good agreement for the effect of varying roughness on the solid fraction profile with an exception for the lower limit of the roughness factor (R=0). For the variation in rotation rate, we show good agreement in both the granular temperature and solid fraction profiles for all rotation rates, but the tangential velocity profile is underpredicted. In addition, the change in rotation rate still has a relatively small effect on the three profiles.

In Figure 36, we show a parametric study of how changes in the total solid fraction for the best case model **S A L 3D** affect the three granular flow distribution profiles. We obtained a reasonable qualitative and quantitative agreement for the base case model for the granular temperature profile. In the tangential velocity profile, the base case model shows a small underprediction for the lower solid fraction ν=0.4 and ν=0.55, with still more underprediction for solid fraction ν=0.71. The results for the higher total solids fraction trials (i.e., $\nu = 0.55$ and $\nu = 0.71$) yield reasonable agreement between experiment and simulation; however, the lower total solids fraction trial (ν=0.4) displays a large discrepancy between

simulation and experiment. Our hypothesis is that the differing measurement techniques for the experiment versus the simulation causes this discrepancy. Recall that, while the simulation data averages over the entire granular shear cell, the experimental measurements focus on a wedge-shaped sector and implicitly assumes that the flow is rotationally invariant. As a test of this hypothesis/assumption, we compare the experimentally measured total solids fraction to the known (i.e., input) value by calculating the area-averaged solids fraction from the measurements shown in Figure 36. In both the higher solids fractions cases this calculation yields a value in close agreement with the known value $\nu_{calc} = 0.56$ versus $\nu_{input} = 0.55$; and $\nu_{calc} = 0.70$ versus $\nu_{input} = 0.71$. In the lower solids fraction case, however, we calculate a substantially higher solids fraction of $\nu_{calc} = 0.50$ versus the known input value of $\nu_{input} = 0.40$. From this result we can conclude that the experimental flow is not rotationally invariant and that the measurement region (and time) is chosen at a "dense" portion of the flow, hence our differing measurement technique for the simulation will result in a profile that is strongly shifted to lower values of ν.

In Figure 37, we show a parametric study varying the roughness and rotation rate of the inner wheel for the best case model **P A L 3D**. For the variation of the roughness factor, the model closely captures the trend and values of two roughness factors (R=0.6 and R=1) in the tangential velocity and solid fraction profiles, however, it fails to do so for the roughness factor of R=0. For the granular temperature profile, all roughness factors results are over predicted when compared to the experiment ones. The dependency on the change in roughness factor seems to be important and has more effect for all of the three profiles.

For the variation of the rotation rate shown in Figure 37, we show that the model closely captures the trend and the values in both tangential velocity and solid fraction profiles but overpredicts the granular temperature profile following the behavior explained earlier for the best case model in Figure 31. Also, we see that the change in the rotation rate have a small effect on all the three distributions, which indicates a weak dependency on the rotation rates used in this study.

Figure 38 shows a parametric study of how changes in the total solid fraction for the best case model **P A L 3D** affects the three granular flow distribution profiles. For the tangential velocity profile, we captured the trend and the values reasonably well (quantitatively and qualitatively). In the solid fraction profile, the agreement is quite good for the higher solid fraction ν=0.55 and ν=0.71, yet it was underpredicted for the lower solid fraction ν=0.4. For the granular temperature distribution, our best case model does not match well with the change in the total solid fraction. We should notice that this discrepancy in the granular temperature profile increases with the increase of the change in the total solid fraction.

The results we obtained from our parametric study for both case models **S A L 3D** and **P A L 3D** were analyzed using the residual sum of squares (RSS) method explained earlier. We are interested to find which case model gives a better fit to the experimental results when varying the roughness, rotation rate, and solid fractions. Table 8 shows the normalized RSS values for varying the roughness of **S A L 3D** and **P A L 3D** computational models. Here, case model **S A L 3D** provides the best fit for roughness values R=0.0 and R=1.0. For roughness value R=0.6, case model **P A L 3D** shows the best fit. Normalized RSS values for varying the rotation rate of **S A L 3D** and **P A L 3D** computational models are shown in Table 9, where case model **S A L 3D** gives the best fit across all the three rotation rates. Finally, we show in Table 10 the normalized RSS values for varying the solid fraction of **S A L 3D** and **P A L 3D** computational models. Here, case model **S A L 3D** shows the best fit for solid fraction $\nu = 0.55$, whereas case model **P A L 3D** shows the best fit for solid fractions $\nu = 0.4$ and $\nu = 0.71$.

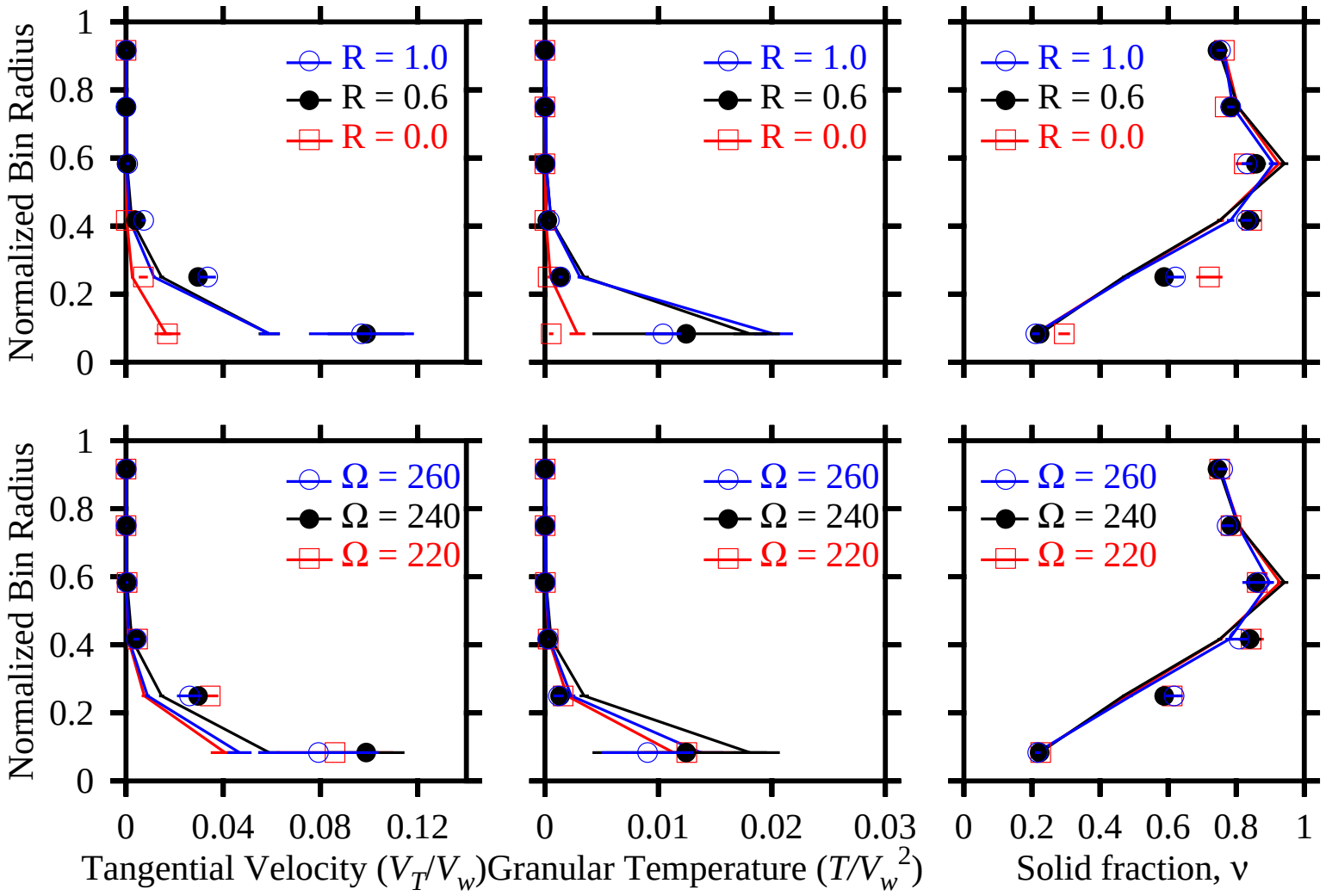

Figure 35: Parametric study varying the inner wheel rotation rate as well as the inner wheel roughness factor. Experimental values are shown as symbols, while the results from the best case model (**S A L 3D**) are shown as lines.

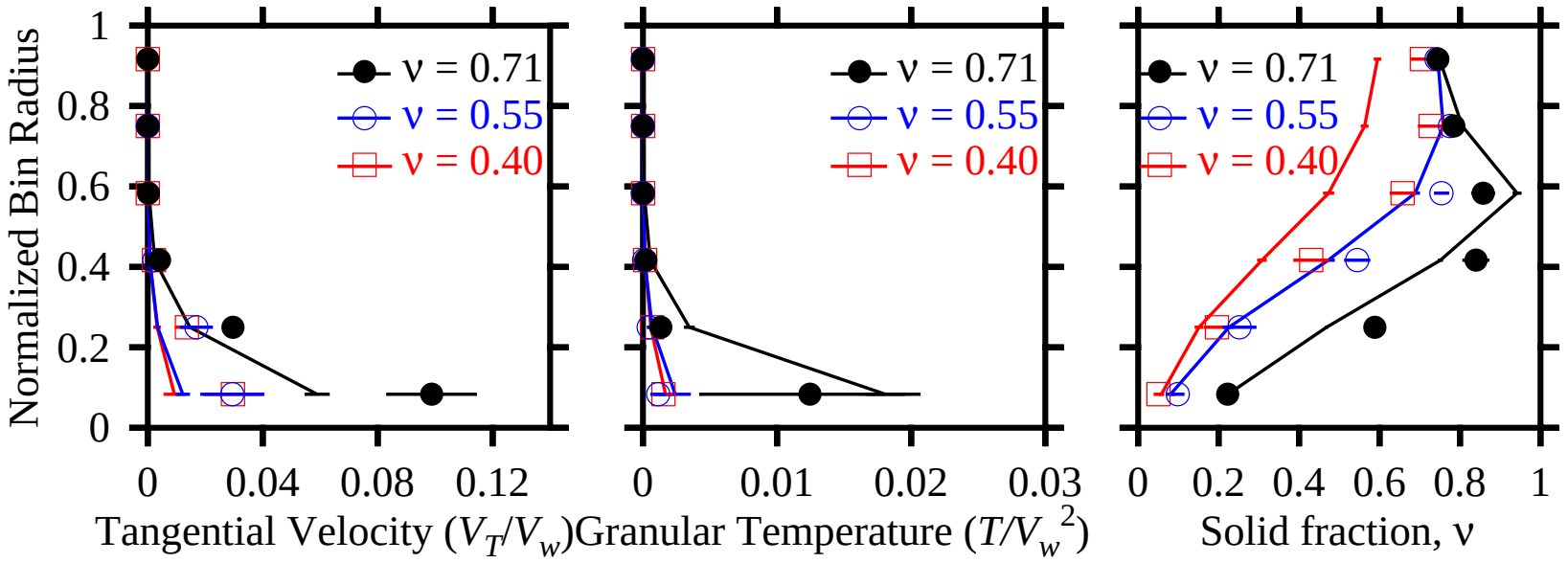

Figure 36: Parametric study varying the total solid fraction. Experimental values are shown as symbols, while the results from the best case model (**S A L 3D**) are shown as lines.

Table 8: Normalized RSS values for varying the roughness of **S A L 3D** and **P A L 3D** computational models

Roughness	**S A L 3D**	**P A L 3D**
R=0.0	0.94	3.00
R=0.6	0.19	0.01
R=1.0	0.46	0.54

Randomly chosen high speed images of the GSC are displayed in Figure 39 for different total (global) solid fraction values. These images display the packing behavior of the granules at ν values of 0.4, 0.55, and 0.71. In the top-left of Figure 39, the annular gap does not show any distinct contact region formation at ν= 0.4, where an obvious spacing exists throughout the particles filling the annular gap. As the solid fraction is increased to ν=0.55 (Figure 39 top-right), a contact region begins to form near the outer wheel, and a few tightly, almost fully packed rows of particles against the outer stationary wheel are obtained. This leads to a formation of two distinct regions within the flow: a kinetic and a contact regions. The bottom of Figure 39 displays a substantial increase in the amount of particles present in the contact region compared to the particles in the kinetic region. No significant changes in the number of particles are observed in the kinetic region during the trial runs.

Table 9: Normalized RSS values for varying the rotation rate of **S A L 3D** and **P A L 3D** computational models

Rotation Rate (Ω)	**S A L 3D**	**P A L 3D**
Ω=220	0.97	1.01
Ω=240	0.64	2.00
Ω=260	0.13	0.41

Table 10: Normalized RSS values for varying the solid fraction of **S A L 3D** and **P A L 3D** computational models

Solid Fraction (ν)	**S A L 3D**	**P A L 3D**
ν=0.40	1.00	0.97
ν=0.55	0.03	2.11
ν=0.71	0.32	0.04

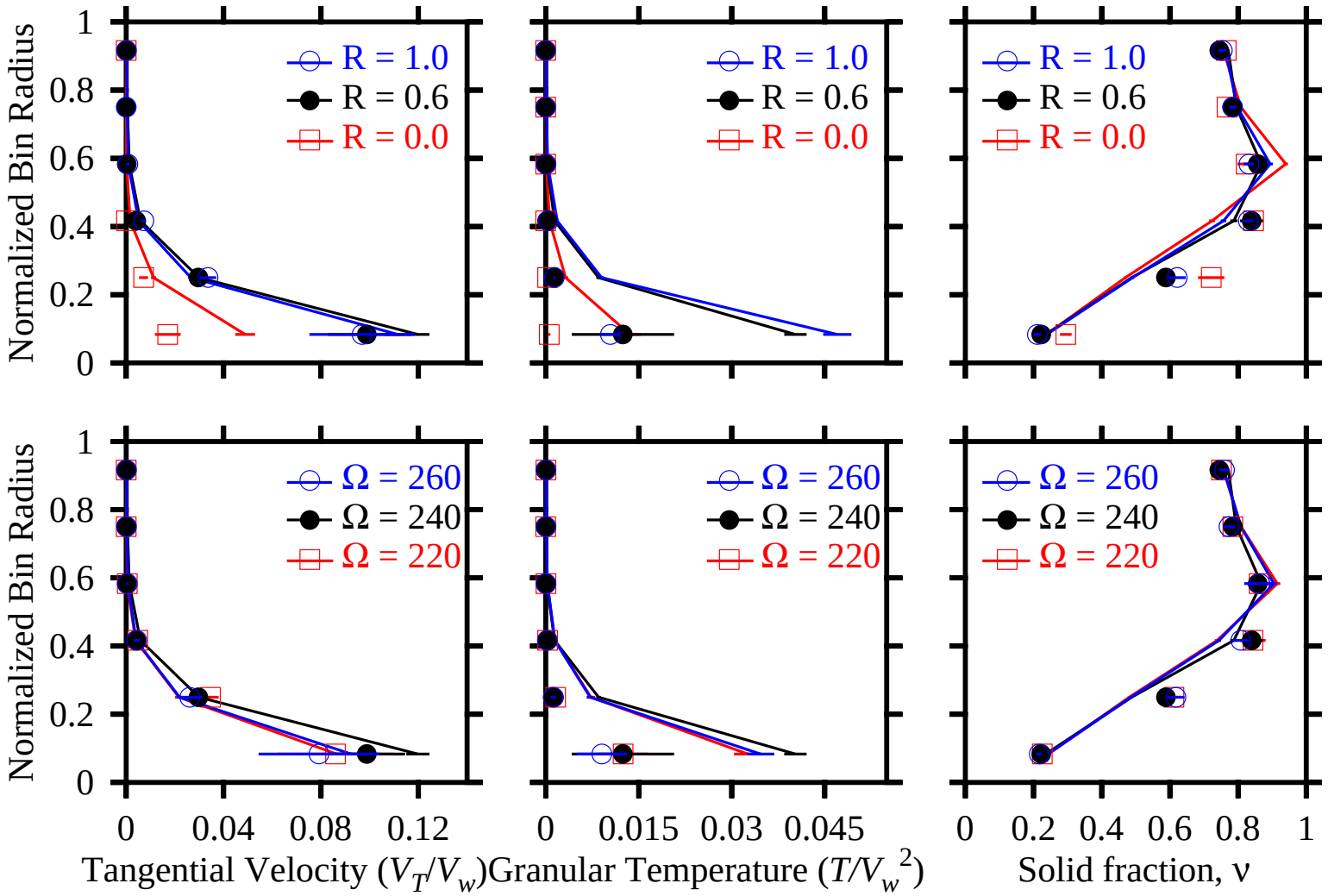

Figure 37: Parametric study varying the inner wheel rotation rate as well as the inner wheel roughness factor. Experimental values are shown as symbols, while the results from the best case model (**P A L 3D**) are shown as lines.

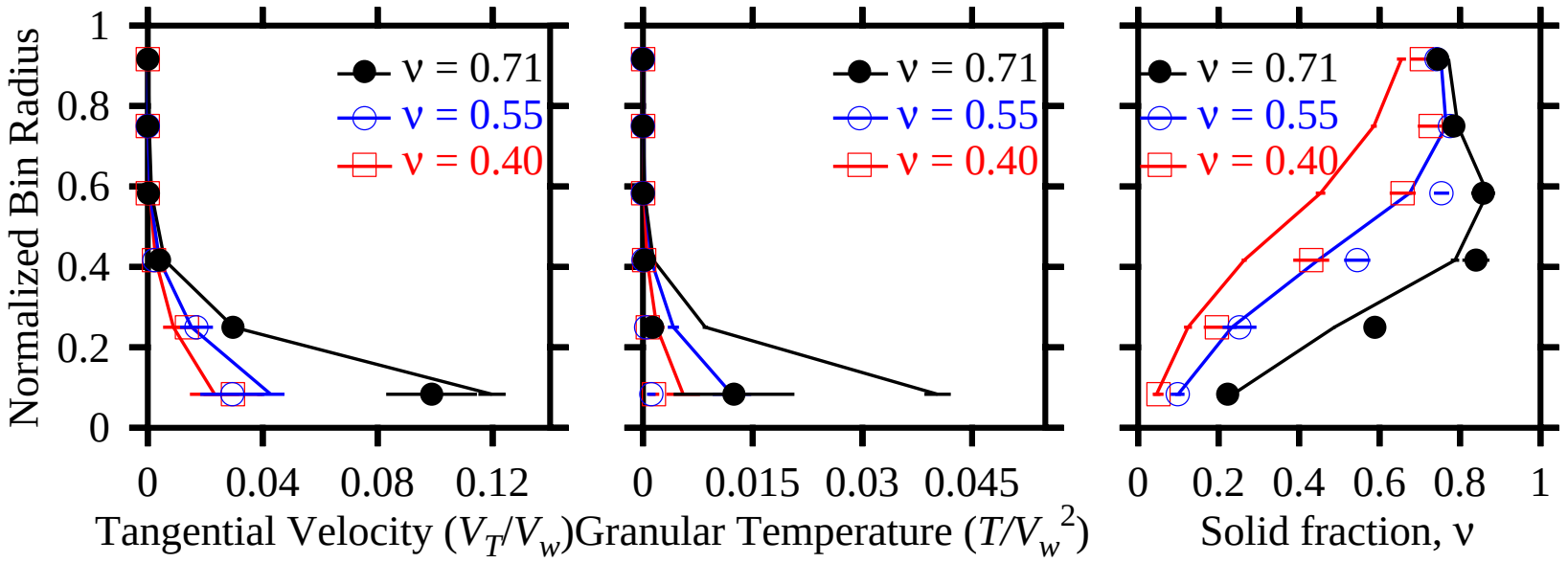

Figure 38: Parametric study varying the total solid fraction. Experimental values are shown as symbols, while the results from the best case model (**P A L 3D**) are shown as lines.

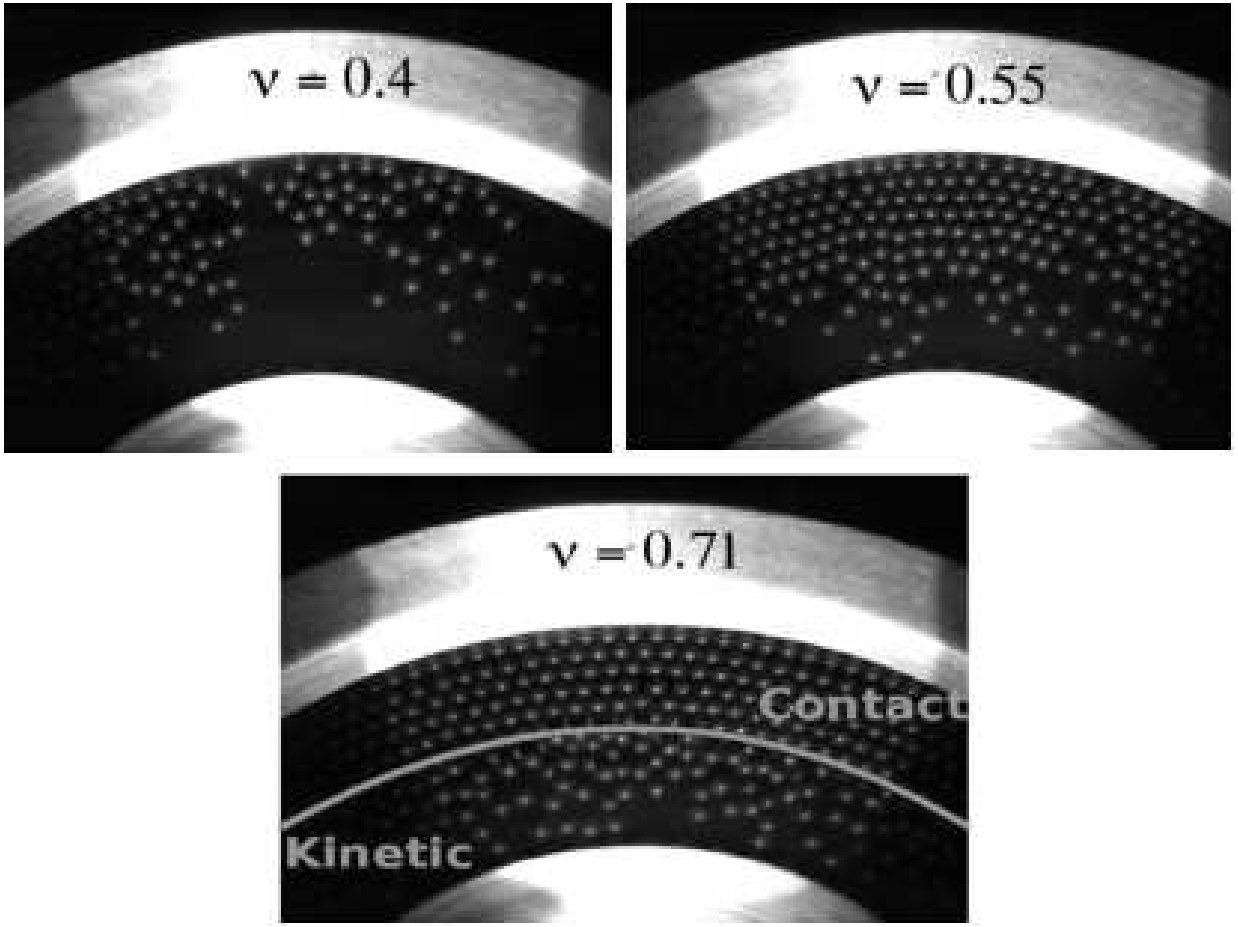

Figure 39: High speed video images of the GSC during trial runs. These images were taken at several different total solid fraction values. Top-left: 0.4, Top-right: 0.55, Bottom: 0.71. The images were randomly selected from trial runs at each of the global solid fraction values listed.

4.5 CONCLUSIONS

In this chapter, we validate our computational method DEM with experimental results obtained using a horizontally-aligned annular shear cell. Three different profiles were measured: solid fraction, tangential velocity, and granular temperature profiles. Both normal force models, plastic and spring-dashpot models, with linear friction parameter and damping parameter matching the literature values were chosen as best case model. However, the plastic model **P A L 3D** always shows over predictions for the granular temperature profile, whereas the spring-dashpot model **S A L 3D** gives a lower predictions in the tangential velocity profile. It was shown that the choice of system geometry is very critical for obtaining an accurate results, particularly for the tangential velocity profile. In addition, it was seen that the choice of frictional force model has insignificant effect across all the profiles and all base case models. Finally, a parametric study was performed for both best case models to test the robustness of their ability to capture both quantitative and qualitative aspects of the experimental flow.

In contrast to what was found in a previous study [8] for stainless steel particles in the GSC, we found that the spring dash-pot model is the most accurate when we use polymeric beads. This could be rationalized based on the fact that the yield velocity for the polymer beads is much higher that the yield velocity for the metal beads. Therefore, we would anticipate that the mode of dissipation is in fact more likely to be viscoelastic in nature for this type of material. However, to our knowledge this is the first evidence that the choice of the most accurate normal force model is actually material dependent.

5.0 SUMMARY AND OUTLOOK

Granular materials are commonplace in our daily life, impacting many of our industries. Over the years, many experiments and models by different researchers have been used to gain more insight into the behavior of granular materials. Most of the work presented in this dissertation was carried out using DEM simulation techniques: Particle Dynamics (PD) and Thermal Particle Dynamics (TPD). PD is based on following each particle's positions, velocities, angular velocities, orientations and temperatures and updating them each time step according to (particle-particle or wall-particle) interactions. TPD is based on the traditional PD technique, where the mechanical and transport properties of granular systems are determined using this technique. Experiments are conducted, when applicable, so that the simulation results can be validated against them.

In this Chapter, we summarize our contributions in each of the topics reported in this dissertation (Sections 5.1 and 5.2), and outline possible directions for future work in Section 5.3.

5.1 CONSOLIDATION OF GRANULAR MATERIAL

In this dissertation, we studied the behavior of granular material under varying conditions. In Chapter 3, we investigated the modeling of consolidation of granular material undergoing heat transfer with lateral periodic conditions. We explored the dynamics associated with the slow compaction of granular materials subjected to thermal cycling. Granular compaction is defined as the increase in the packing fraction of a granular medium due to some perturbation process. Although it has been shown that the thermal expansion of the wall

might increase the degree of compaction attained, in this work we showed that the expansion and contraction of the particles alone is sufficient to achieve bed compaction. This was demonstrated by using unconfined walls (i.e., lateral periodic boundary conditions) in our simulations. We can conclude that in unconsolidated granular media, a systematic and controllable increase in granular packing can be induced by simply raising and then lowering the temperature, without the input of any mechanical energy. In addition, thermal cycling can be an alternative to tapping or vibration as a mean to induce densification.

In this work, the experiments and simulations only considered the behavior of pure materials. It would be interesting to investigate how a mixture of granular materials would behave under thermal cycling. Some preliminary experiments were conducted to understand this behavior and the results are shown in Figure 40. The solid fraction is measured at long time evolution thermal cycling whereas the apparent height is measured at short time evolution thermal cycling, both at $\Delta T = 40°C$. A similar study would aid in clarifying the behavior of a mixture of materials during the thermal cycling process.

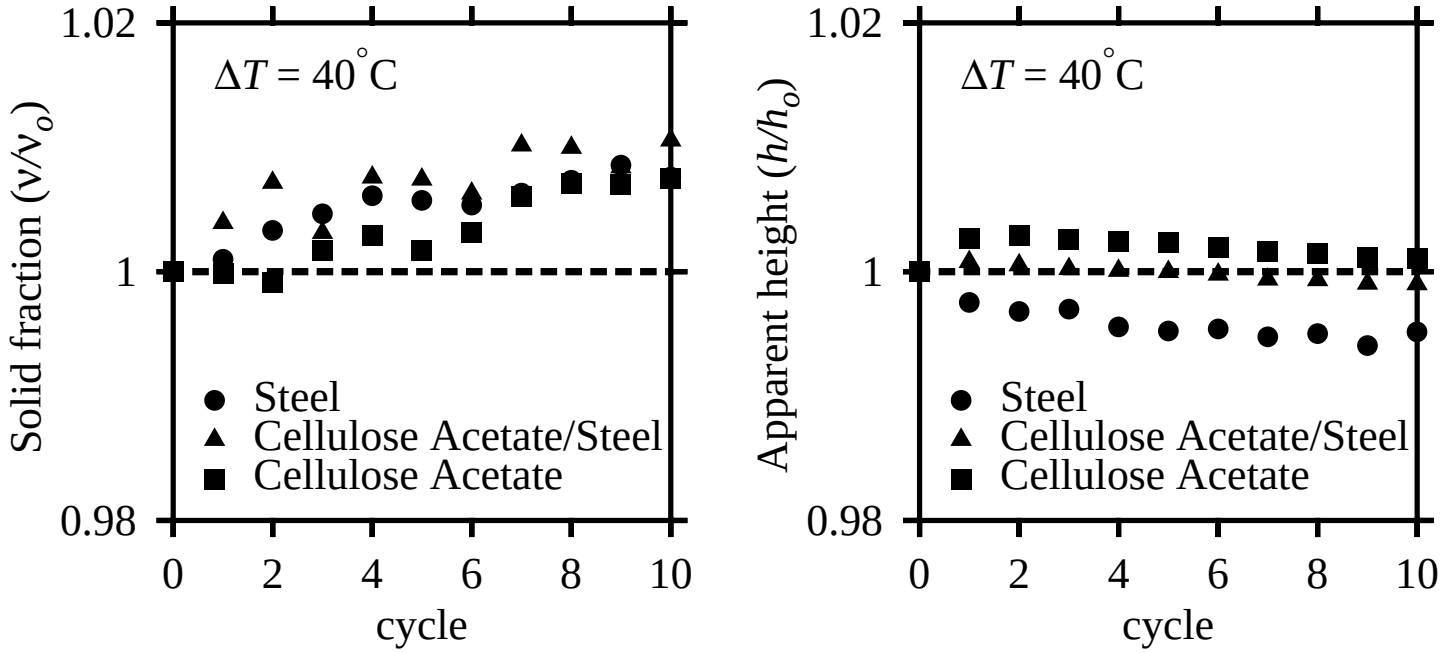

Figure 40: Solid fraction (left) during long periods of thermal cycling and apparent height (right) during short periods of thermal cycling for a pure and mixture of materials at $\Delta T = 40°C$

5.2 FLOW OF GRANULAR MATERIAL

We described a detailed comparison of experimental and simulation results of granular flow in an annular shear cell in Chapter 4. The work reported allows for better understanding of the interaction between rough driving surfaces and granular flows. For the experiments, a two-dimensional annular shear cell with sets of different interchangeable driving wheels was used along with a digital particle tracking velocimetry (DPTV) to report the solid fraction distributions, tangential velocity profiles, and granular temperature profiles.

The driving wheels of the shear cell are built with quantifiable roughness factors. It was noticed that static electricity could have an impact on the experimental results. For the simulations, we used DEM with different contact mechanics force laws, particle geometry, and material properties employed to reproduce the solid fraction, tangential velocity, and granular temperature data and compare them with the experimental values. DEM is eminently suited to study most of the difficult aspects of granular flows. It is considered as the gold standard for comparison to continuum level theories of granular material flows. The validation results indicate that the choice of normal force model (i.e., mode of dissipation, plastic and spring-dashpot models) is not critical as long as the damping parameter is chosen to match the literature values.

In addition, the choice of frictional force models did not show any significant difference across all profiles. However, it was shown that the system geometry is important in order to obtain accurate results. Finally, the results of a sensitivity analysis on the wheel rotation rates and the wheel roughness are reported. It was concluded that case model **S A L 3D** is the best case model to use for our validation study with experimental results. This indicates that a spring dash-pot mode of dissipation is superior to plastic deformation in our study.

5.3 THERMOELASTIC CONTACT INSTABILITY

Building upon the discussion from Chapter 3, there have been some research studies that focused on the thermo-mechanical coupling through the boundary conditions between two dissimilar materials in contact. In this section, we will introduce this idea with some preliminary results.

5.3.1 The Model

Figure 41 shows a schematic of a system where two different materials are built into perfectly conducting rigid walls each maintained at different temperature (T). The materials with different lengths (L) have a small gap (g) between their free end faces initially when the temperature everywhere is at room temperature.

With the assumption of constant thermal conductivity and no heat source exists, the governing equation for the one-dimensional transient heat conduction of the two materials, shown in Figure 41, can be expressed as

$$\frac{\partial T}{\partial t} = \alpha_T \frac{\partial^2 T}{\partial x^2} \tag{5.1}$$

Finite difference methods are simple and efficient techniques for solving ordinary or partial differential equations. In our case, solving the partial differential equations numerically requires that we divide the time into small segments Δt and replace all the derivatives with their finite difference analogs, such that time is now a discrete variable and not a continuous one. We used the finite difference method to make our governing Equation 5.1 dimensionless and then we discretized it along with any other equations, when needed, that arise from the existing boundary conditions. To illustrate, for the left boundary of the material on the left and for the right boundary of the material on the right (see Figure 41), the temperature should be specified and known. Therefore, no additional discretization equations are required. On the other hand, the other two boundaries at the tips (contact spot) of the two materials require an integration of the dimensionless governing equation after applying the appropriate boundary conditions, i.e., the heat flux expressions.

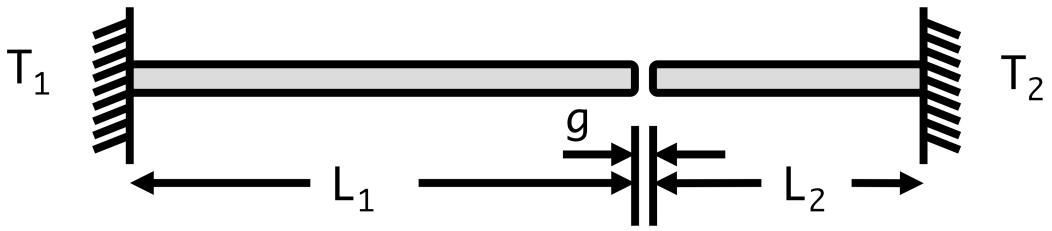

Figure 41: Schematic of the system of two different materials in thermoelastic contact

In Figure 41, the heat flux expression at the contact spot for the left rod can be described as

$$at \;\; x = L_1, \qquad -k\frac{\partial T_1}{\partial x} = H_c(T_1 - T_2) \tag{5.2}$$

where $H_c = 1/R_c$ represents the contact conductance, and R_c is the resistance at the contact spot. A similar expression can be obtained for the right rod. The boundary condition at the contact spot can be described as a nonlinear one since the contact conductance term is a function of gap (g), which is also a function of temperature. The equations that describe the contact and separation are

$$Contact: \;\; g \leq 0, \qquad R_c = R_0 e^{-E^* g/P_{char}} \tag{5.3}$$

$$Separation: \;\; g > 0, \qquad R_c = R_0 - \frac{g}{k_{air}} \tag{5.4}$$

where R_0 is the initial zero gap resistance, E is Young's modulus, P_{char} is the characteristic pressure, and k_{air} is the conductivity of air.

5.3.2 Simulations

We constructed dimensionless groups for all the parameters that have an influence on our system. The dimensionless groups represent the materials and gap properties. We used a finite difference approach and developed a C program to simulate the transient behavior of

the system. According to Figure 42, our preliminary results show an oscillatory behavior for the gap/overlap and the tip temperatures for steel and aluminum materials during the separation and contact processes. This behavior depends on the parameters values chosen for each material and the gap in between. Also, we show additional results with the choice of polymers instead of metals in Figure 43.

When associated with thermal boundary conditions, the thermo-mechanical coupling of dissimilar materials in contact can lead to interesting phenomena. Instability in the temperature at the contact point of two dissimilar materials can occur for a range of different parameters such as material properties, length, gap, etc. Using a finite difference method with dimensionless parameters, we plan to perform a stability analysis of the one-dimensional heat conduction problem to identify the region with the most oscillatory behavior in the temperature profile. An analysis approach is used to identify the instability region for a host of material properties and physical dimensions. It is assumed that the contact resistance between the end points of the dissimilar materials is a function of the gap or the contact pressure. We believe that a combination of unique material properties is the key to obtain an oscillatory temperature profile. Experiments with our choice of materials are planned to validate the observations from the numerical analysis.

We desire to extend the investigation in Section 5.3.1 for different contact spot geometries such as contacts between spheres, and contacts between rough surfaces. We are also interested in knowing how the thermoelastic contact can impact the contact conductance in particle beds. We plan to incorporate the contact conductance concept based on actual physics to better describe the contact mechanics between two different materials. The previous work [88] was based on an ad-hoc approach where the contact conductance was fitted to experimental data but here we propose to use a more realistic contact approach.

5.3.3 Experiments

Experimental investigations are proposed to validate the results from our mathematical model. The suggested model should give us a good indication about the proper choice of material and physical dimensions that should be used in the experiments. The next step is

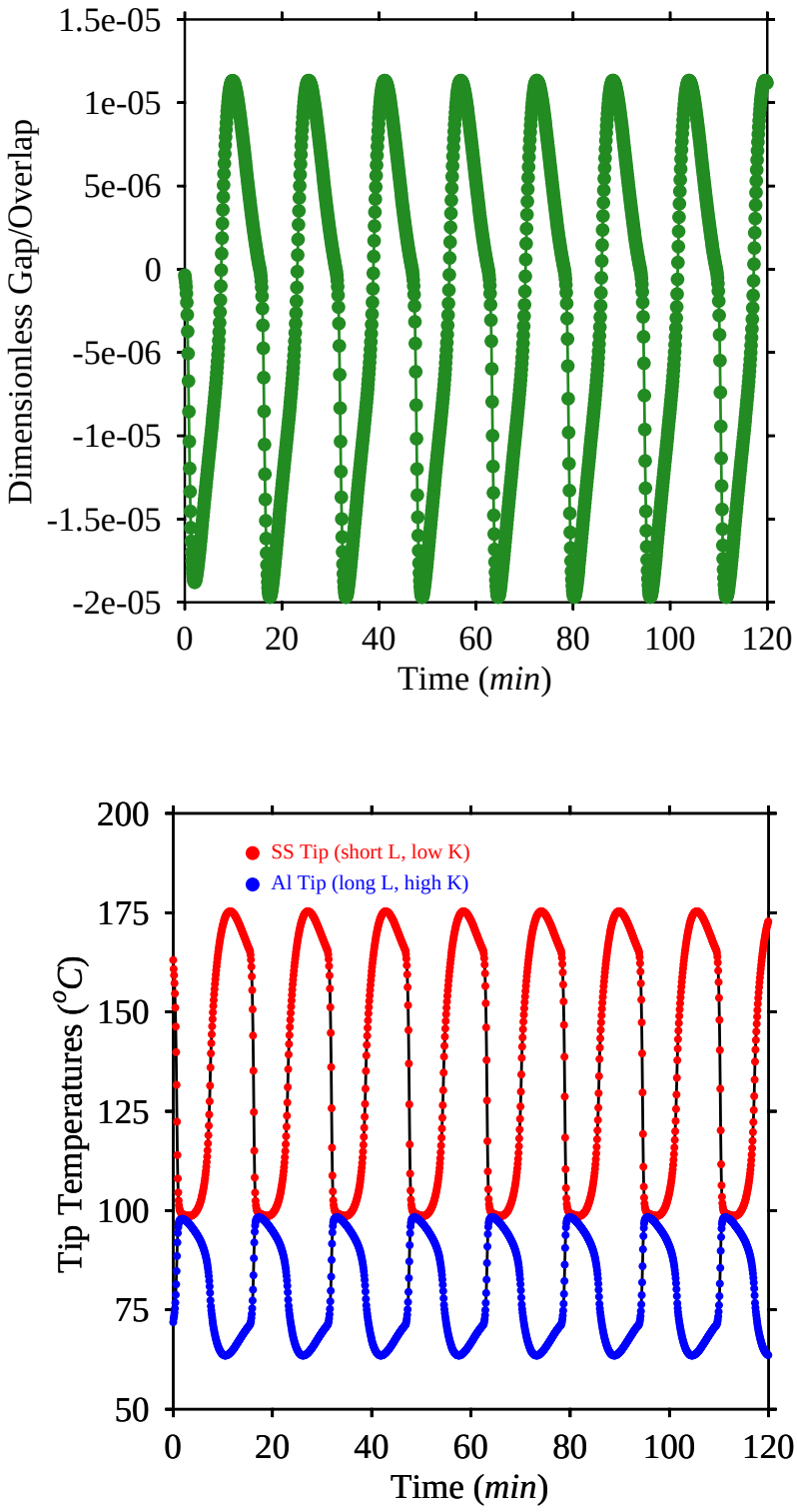

Figure 42: Oscillatory behavior for dissimilar materials of metal type. Top: Gap/Overlap. Bottom: Tip temperatures

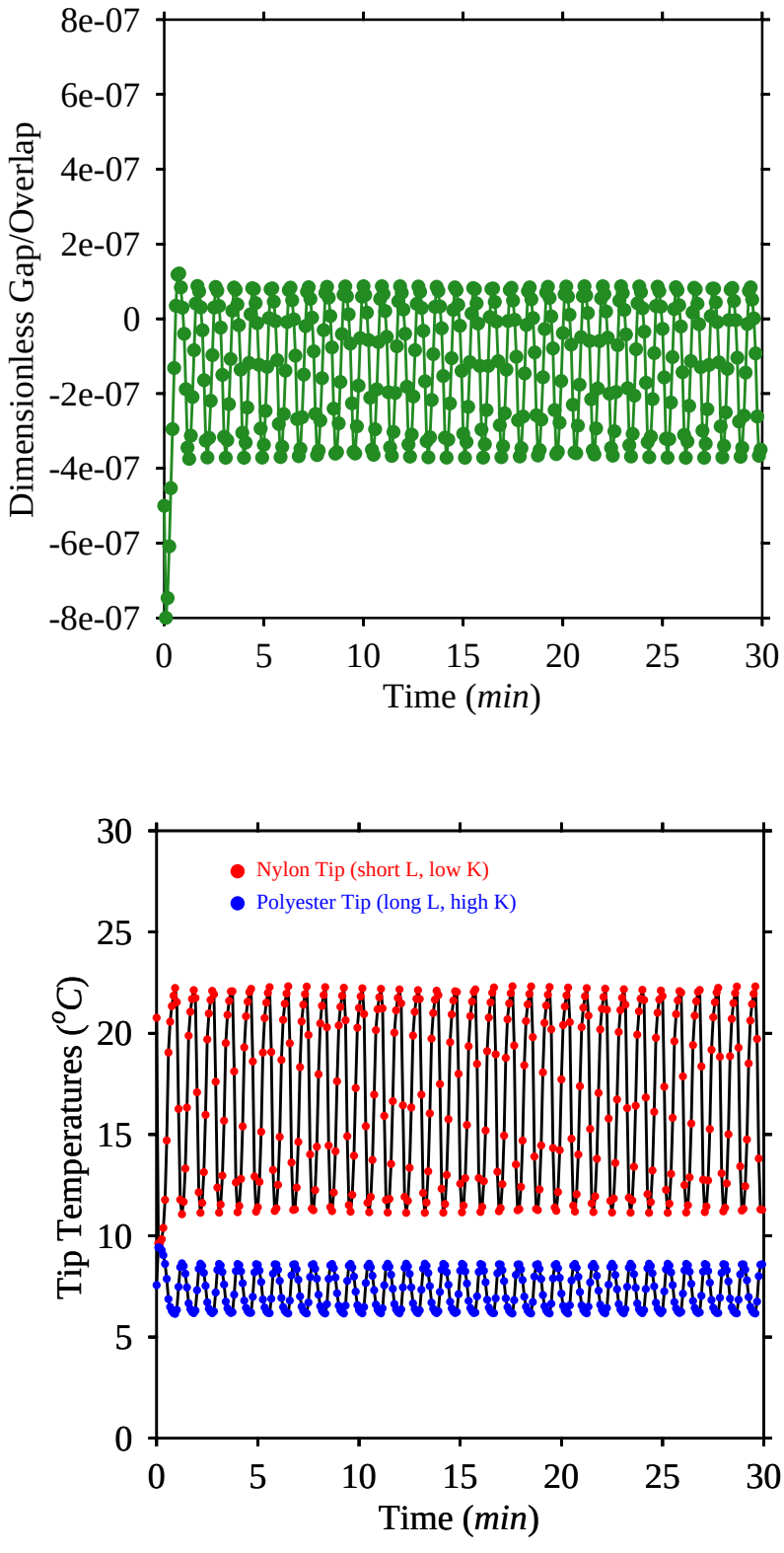

Figure 43: Oscillatory behavior for dissimilar materials of polymer type. Top: Gap/Overlap. Bottom: Tip temperatures

to be able to build an experimental set up that will allow us to measure the temperature of the contact spot. Figure 44 shows a preliminary sketch of the experimental set up. It shows two dissimilar materials (blocks or slabs) with a very small gap in between, where one side is kept cold (around $0°C$) using a cup of ice water, and the other side is heated via a digital heating tape device. The ice water should be stirred frequently to ensure that the material surface is exposed to a uniform temperature. We are interested in measuring the temperatures of the two materials at the interface.

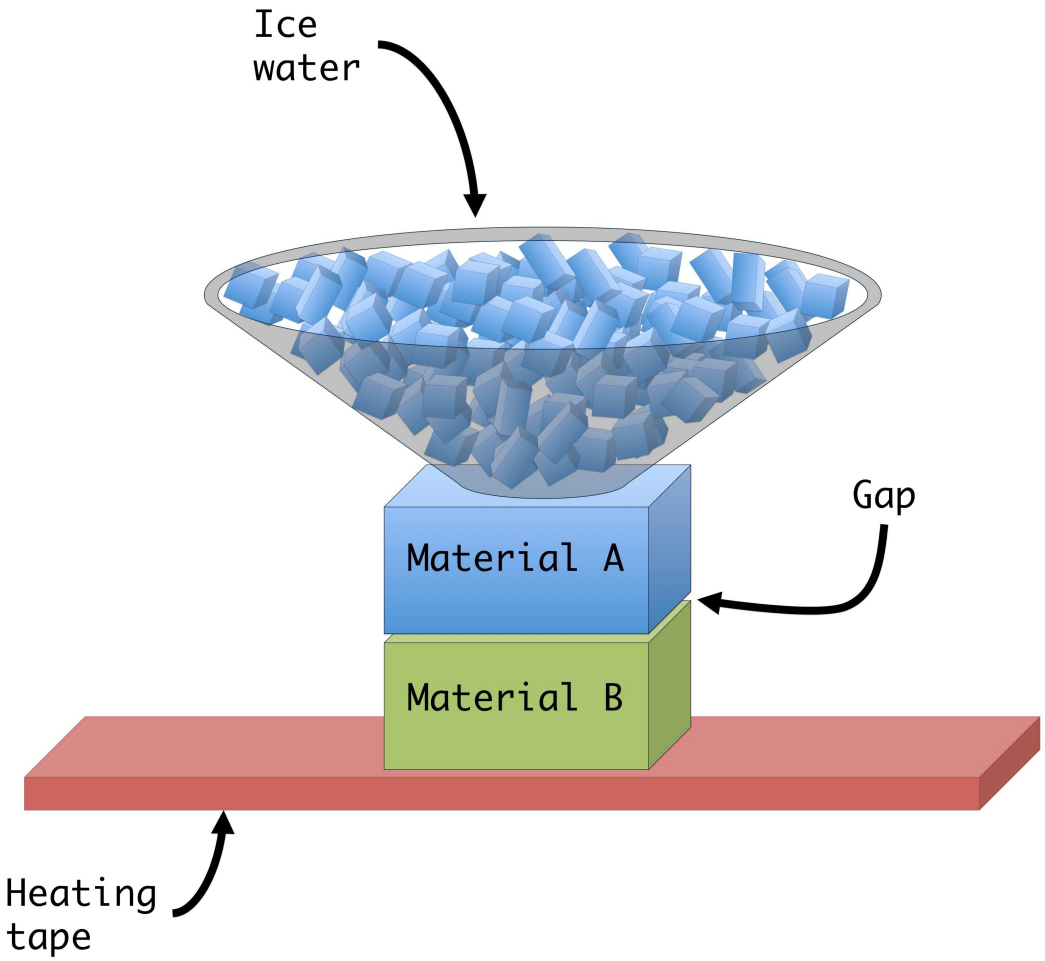

Figure 44: Preliminary Sketch of the experimental set-up for two different materials in thermoelastic contact

APPENDIX

NOMENCLATURE

English Symbols:

a	: radius of the contact spot
A	: cross sectional area of the particle
A_{bed}	: area of the granular bed
A_i	: area of bin i
Bi	: Biot number
c	: heat capacity
C_p	: heat capacity of the bed
c_i	: heat capacity of particle i
d_p	: particle diameter
E^*	: effective Young's modulus
E_i	: Young's modulus of particle i
F_{max}	: maximum value of normal force during collision
$\vec{F}_n$	: normal force
F_{old}	: normal force at the previous time step
$\vec{F}_t$	: tangential force
F_{t_o}	: old tangential force
F_y	: yield force

English Symbols:

g	: gravitational acceleration
g	: gap between two rods (Ch. 5)
G	: shear modulus
h	: granular bed height
h_c	: convective heat transfer coefficient
H_c	: contact conductance
H_I	: initial drop height
H_R	: maximum rebound height
h_o	: initial height of granular bed
I_p	: particle moment of inertia
k	: conductivity of the bed
k_{air}	: thermal conductivity of air
k_{eff}	: effective conductivity
k_f	: fluid interstitial medium conductivity
k_n	: normal contact stiffness
k_s	: thermal conductivity of the solid
k_t	: tangential contact stiffness
k_{t_o}	: initial tangential stiffness
k_y	: plastic stiffness
L	: length or depth
m_p	: particle mass
N	: total number of particles
N_i	: number of particles in bin i
P_{char}	: characteristic pressure
Q	: heat flow
Q_i	: total amount of heat transported to particle i
Q_{ij}	: heat flow between particles i and j

English Symbols:

r	: radius of a particle
R	: particle radius
R^*	: effective particle radius
$\bar{R}$	: dimensionless radius
R_0	: initial zero gap resistance
R_c	: resistance at the contact spot
r_i	: radius of bin i
$\vec{R_i}$	: radius of particle i
r_o	: radius of outer wheel
R_o	: initial radius of the particle
R_p	: radius of curvature after plastic deformation
r_w	: radius of inner wheel
S_{12}	: distance between particle centers of particle 1 and 2
T	: temperature
T^*	: first load reverse point for tangential force
T^{**}	: second load reverse point for tangential force
T_i	: granular temperature
T_o	: initial temperature
T_f	: fluid temperature
V_{bed}	: volume of the granular bed
V_{bed_o}	: initial volume of the granular bed
V_i	: volume of particle i
v_I	: impact velocity
v_{I_G}	: impact velocity of the granule
v_{I_P}	: impact velocity of the plate
$\vec{v_p}$	: particle velocity
v_R	: rebound velocity

English Symbols:

v_{R_G}	: rebound velocity of the granule
v_{R_i}	: radial velocity of particle i
v_{R_j}	: radial velocity of particle j
v_{R_P}	: rebound velocity of the plate
V_{solid}	: volume of the solid
V_{solid_o}	: initial volume of the solid
v_t	: tangential velocity
V_{T_i}	: average tangential velocity
v_{T_i}	: tangential velocity of particle i
v_{T_j}	: tangential velocity of particle j
x_t	: position at time t
$\dot{x}_t$	: velocity at time t
$\ddot{x}_t$	: acceleration at time t

Greek symbols:

α	: computational overlap between contacting particles
$\dot{\alpha}$	: relative normal velocity of particles
α_{max}	: maximum deformation
α_o	: constant
α_T	: thermal diffusivity
α_y	: deformation at the point of yield
β	: a damping (fitting) parameter
Δs	: tangential displacement
Δt	: time-step
ΔT_{ij}	: temperature difference between the mid-planes of the spheres

Greek symbols:

η	: dimensionless spatial coordinate (similarity variable)
λ	: relevant disturbance wave speed
μ_f	: friction coefficient
μ	: friction coefficient
ν	: solid fraction
ν_i	: solid fraction in radial bin i
ν_o	: initial solid fraction
Ω	: rotation rate
$\vec{\omega}_p$	: particle angular velocity
ρ	: density of the particle
ρ_i	: density of particle i
σ	: poisson ratio of the particle
σ_i	: poisson ratio of particle i
σ_i	: standard deviation (Ch. 4)
τ	: dimensionless time
θ	: tangential force flag
Θ	: dimensionless temperature
ξ	: dimensionless length

Subscripts and superscripts:

L	: loading
max	: maximum value
old	: previous time-step
R	: reloading
U	: unloading
y	: yield point

Abbreviations:

CA	: Cellulose Acetate
COR	: Coefficient Of Restitution
DEM	: Discrete Element Method
$DPTV$	: Digital Particle Tracking Velocimetry
FCC	: Face Center Cubic
GSC	: Granular Shear Cell
HCP	: Hexagonal Close Packing
MD	: Molecular Dynamics
MFD	: Mixed-Flow Drayer
MRI	: Magnetic Resonance Imaging
PD	: Particle Dynamics
RSS	: Residual Sum of the Squared
RTD	: Residence Time Distribution
TPD	: Thermal Particle Dynamics
XMT	: X-ray Microtomography

BIBLIOGRAPHY

[1] O. Reynolds. On the dilatancy of media comprised of rigid particles in contact. with experimental illustration. *Phil. Mag.*, 20:469–481, 1881.

[2] C. Thornton and D. J. Barnes. Computer simulated deformation of compact granular assemblies. *Acta Mech.*, 64:45–61, 1986.

[3] C. H. Liu, S. Nagel, D. Shechter, S. Coppersmith, S. Majumdar, O. Narayan, and T. Witten. Force fluctuations in bead packs. *Science*, 269:513–515, 1995.

[4] H. Rumpf. *Particle Technology*. Chapman and Hall Publishers, New York, 1975.

[5] K. Kendall, McN, and J. D. Birchall. Elasticity of particle assemblies as a measure of the surface energy of solids. *Proceedings of the Royal Society of London. Series A, Mathematical and Physical Sciences*, 412(1843):269–283, 1987.

[6] H. M. Jaeger and S. R. Nagel R. P. Behringer. Granular solids, liquids and gases. *Rev. Mod. Phys.*, 68:1259–1273, 1996.

[7] C Campbell. Granular material flows – an overview. *Powder Technology*, 162(3):208–229, 2006.

[8] J. J. McCarthy, V. Jasti, M. Marinack, and C. F. Higgs. Quantitative validation of the discrete element method using an annular shear cell. *Powder Technology*, 203(1):70–77, 10 2010.

[9] C.J. Broadbent, J. Bridgwater, D.J. Parker, S.T. Keningley, and P. Knight. A phenomenological study of a batch mixer using a positron camera. *Powder Technology*, 76(3):317 – 329, 1993.

[10] Z. Yang, P. J. Fryer, S. Bakalis, X. Fan, D. J. Parker, and J. P. K. Seville. An improved algorithm for tracking multiple, freely moving particles in a positron emission particle tracking system. *Nuclear Instruments & Methods in Physics Research Section A-Accelerators Spectrometers Detectors and Associated Equipment*, 577(3):585–594, JUL 11 2007.

[11] M. Nakagawa, S. A. Altobelli, A. Caprihan, E. Fukushima, and E. K. Jeong. Non-invasive measurements of granular flows by magnetic resonance imaging. *Experiments in Fluids*, 16(1):54–60, 11 1993/11/01/.

[12] MS Nikitidis, U Tuzun, and NM Spyrou. Measurement of size segregation by self-diffusion in slow-shearing binary mixture flows using dual photon gamma-ray tomography. *CHEMICAL ENGINEERING SCIENCE*, 53(13):2335–2351, JUL 1998.

[13] Venkata Jasti and III Higgs, C. Fred. Experimental study of granular flows in a rough annular shear cell. *Physical Review E*, 78(4), OCT 2008.

[14] C. T. Veje, Daniel W. Howell, and R. P. Behringer. Kinematics of a two-dimensional granular couette experiment at the transition to shearing. *Phys. Rev. E*, 59(1):739–745, Jan 1999.

[15] G. Chambon, J. Schmittbuhl, A. Corfdir, J. P. Vilotte, and S. Roux. Shear with comminution of a granular material: Microscopic deformations outside the shear band. *Physical Review E*, 68(1), 07 2003/07/23/.

[16] Nitin Jain, J. M. Ottino, and R. M. Lueptow. An experimental study of the flowing granular layer in a rotating tumbler. *Physics of Fluids*, 14(2):572–582, 02 2002.

[17] Martin C. Marinack, Venkata K. Jasti, Young Eun Choi, and C. Fred Higgs III. Couette grain flow experiments: The effects of the coefficient of restitution, global solid fraction, and materials. *Powder Technology*, 211(1):144 – 155, 2011.

[18] R. A. Bagnold. Experiments on a gravity-free dispersion of large solid spheres in a newtonian fluid under shear. *Proceedings of the Royal Society of London, A*, 225:4–63, 1954.

[19] Daniel M. Mueth, Georges F. Debregeas, Greg S. Karczmar, Peter J. Eng, Sidney R. Nagel, and Heinrich M. Jaeger. Signatures of granular microstructure in dense shear flows. *Nature*, 406(6794):385–389, 07 2000.

[20] Charles S. Campbell and Christopher E. Brennen. Computer simulation of granular shear flows. *Journal of Fluid Mechanics*, 151:167–188, 1985.

[21] Michel Y. Louge. Computer simulations of rapid granular flows of spheres interacting with a flat, frictional boundary. *Physics of Fluids*, 6(7):2253–2269, 1994.

[22] H. P. Kuo, P. C. Knight, D. J. Parker, Y. Tsuji, M. J. Adams, and J. P. K. Seville. The influence of dem simulation parameters on the particle behaviour in a v-mixer. *Chemical Engineering Science*, 57(17):3621 – 3638, 2002.

[23] A.P. Grima and P.W. Wypych. Investigation into calibration of discrete element model parameters for scale-up and validation of particle–structure interactions under impact conditions. *Powder Technology*, 212(1):198 – 209, 2011.

[24] Steffen Schöllmann. Simulation of a two-dimensional shear cell. *Phys. Rev. E*, 59:889–899, Jan 1999.

[25] J. J. McCarthy, D. V. Khakhar, and J. M. Ottino. Computational studies of granular mixing. *Pow. Technol.*, 109:72–82, 2000.

[26] Shunying Ji, Daniel M. Hanes, and Hayley H. Shen. Comparisons of physical experiment and discrete element simulations of sheared granular materials in an annular shear cell. *Mechanics of Materials*, 41(6):764 – 776, 2009.

[27] P. A. Cundall and O. D. L. Strack. A discrete numerical model for granular assemblies. *Géotechnique*, 29:47–65, 1979.

[28] M. Kwapinska, G. Saage, and E. Tsotsas. Continous versus discrete modelling of heat transfer to agitated beds. *Powder Technology*, 181:331–342, 2008.

[29] B. Chaudhuri, F. J. Muzzio, and M. S. Tomassone. Modeling of heat transfer in granular flow in rotating vessels. *Chemical Engineering Science*, 61:6348–6360, 2006.

[30] W. L. Vargas and J. J. McCarthy. Heat conduction in granular materials. *AIChE Journal*, 47:1052–1059, 2001.

[31] D. K. Kafui and C. Thornton. Fully-3d dem simulation of fluidised bed spray granulation using an exploratory surface energy-based spray zone concept. *Powder Technol.*, 2007.

[32] Xiaowei Fu, Meenakshi Dutt, A. Craig Bentham, Bruno C. Hancock, Ruth E. Cameron, and James A. Elliott. Investigation of particle packing in model pharmaceutical powders using x-ray microtomography and discrete element method. *Powder Technology*, 167(3):134 – 140, 2006.

[33] James W. Landry and Gary S. Grest. Granular packings with moving side walls. *Phys. Rev. E*, 69(3):031303, Mar 2004.

[34] Gary E. Mueller. Numerically packing spheres in cylinders. *Powder Technology*, 159(2):105 – 110, 2005.

[35] Konstantin Sobolev and Adil Amirjanov. The development of a simulation model of the dense packing of large particulate assemblies. *Powder Technology*, 141(1-2):155 – 160, 2004.

[36] Jiansheng Xiang. The effect of air on the packing structure of fine particles. *Powder Technology*, 191(3):280 – 293, 2009.

[37] Jong Cheol Kim, David M. Martin, and Chang Sung Lim. Effect of rearrangement on simulated particle packing. *Powder Technology*, 126(3):211 – 216, 2002.

[38] Hernan A. Makse, David L. Johnson, and Lawrence M. Schwartz. Packing of compressible granular materials. *Phys. Rev. Lett.*, 84(18):4160–4163, May 2000.

[39] Thomas C. Hales. The sphere packing problem. *Journal of Computational and Applied Mathematics*, 44(1):41 – 76, 1992.

[40] Chaoming Song, Ping Wang, and Hernan A. Makse. A phase diagram for jammed matter. *Nature*, 453(7195):629–632, 05 2008.

[41] Robert S. Farr and Robert D. Groot. Close packing density of polydisperse hard spheres. *The Journal of Chemical Physics*, 131(24):244104, 2009.

[42] Neil J. A. Sloane. Kepler's conjecture confirmed. *Nature*, 395(6701):435–436, 10 1998.

[43] Wenli Zhang, Karsten E. Thompson, Allen H. Reed, and Liese Beenken. Relationship between packing structure and porosity in fixed beds of equilateral cylindrical particles. *Chemical Engineering Science*, 61(24):8060 – 8074, 2006.

[44] T. Aste, M. Saadatfar, A. Sakellariou, and T. J. Senden. Investigating the geometrical structure of disordered sphere packings. *Physica A: Statistical Mechanics and its Applications*, 339(1-2):16 – 23, 2004. Proceedings of the International Conference New Materials and Complexity.

[45] Robert Connelly. Rigidity of packings. *Eur. J. Comb.*, 29(8):1862–1871, 2008.

[46] B. N. Asmar, P. A. Langston, A. J. Matchett, and J. K. Walters. Validation tests on a distinct element model of vibrating cohesive particle systems. *Computers and Chemical Engineering*, 26(6):785 – 802, 2002.

[47] C. Thornton and K. K. Yin. Impact of elastic spheres with and without adhesion. *Powder Technology*, 65:153–166, 1991.

[48] C. Thornton, K. K. Yin, and M. J. Adams. Numerical simulation of the impact fracture and fragmentation of agglomerates. *Journal of Physics D: Applied Physics*, 29:424–435, 1996.

[49] C. Thornton and S. J. Antony. Quasi-static shear deformation of a soft particle system. *Powder Technology*, 109(1-3):179 – 191, 2000.

[50] Y. Sheng, C. J. Lawrence, B. J. Briscoe, and C. Thornton. Numerical studies of uniaxial powder compaction process by 3d dem. *Engineering Computations: Int J for Computer-Aided Engineering*, pages 304–317, 2004.

[51] P. G. de Gennes. Granular matter: a tentative view. *Rev. Mod. Phys.*, 71:S374–S382, 1999.

[52] Patrick Richard, Mario Nicodemi, Renaud Delannay, Philippe Ribiere, and Daniel Bideau. Slow relaxation and compaction of granular systems. *Nat Mater*, 4(2):121–128, 02 2005.

[53] D. Arsenovic, S. B. Vrhovac, Z. M. Jaksic, Lj. Budinski-Petkovic, and A. Belic. Simulation study of granular compaction dynamics under vertical tapping. *Phys. Rev. E*, 74(6):061302, Dec 2006.

[54] P. Philippe and D. Bideau. Compaction dynamics of a granular medium under vertical tapping. *EPL (Europhysics Letters)*, 60(5):677–683, December 2002.

[55] A. Mehta and G. C. Barker. Vibrated powders: A microscopic approach. *Phys. Rev. Lett.*, 67:394–397, 1991.

[56] James B. Knight, Christopher G. Fandrich, Chun Ning Lau, Heinrich M. Jaeger, and Sidney R. Nagel. Density relaxation in a vibrated granular material. *Phys. Rev. E*, 51(5):3957–3963, May 1995.

[57] G. C. Barker and Anita Mehta. Transient phenomena, self-diffusion, and orientational effects in vibrated powders. *Phys. Rev. E*, 47(1):184–188, Jan 1993.

[58] Jasna Brujic, Ping Wang, Chaoming Song, David L. Johnson, Olivier Sindt, and Hernan A. Makse. Granular dynamics in compaction and stress relaxation. *Phys. Rev. Lett.*, 95(12):128001, Sep 2005.

[59] G. DAVID Scott. Packing of spheres: Packing of equal spheres. *Nature*, 188(4754):908–909, 12 1960.

[60] Adem Dogangun, Zeki Karaca, Ahmet Durmus, and Halil Sezen. Cause of damage and failures in silo structures. *Journal of Performance of Constructed Facilities*, 23(2):65–71, 2009.

[61] John W. Carson and Tracy Holmes. Silo failure: Why do they happen? *Task Quarterly*, 7(4):499–512, 2003.

[62] K. Chen, J. Cole, C. Conger, J. Draskovic, M. Lohr, K. Klein, T. Scheidemantel, and P. Schiffer. Granular materials: Packing grains by thermal cycling. *Nature*, 442:257–257, 2006.

[63] Thibaut Divoux, Hervé Gayvallet, and Jean-Christophe Géminard. Creep motion of a granular pile induced by thermal cycling. *Phys. Rev. Lett.*, 101(14):148303, Oct 2008.

[64] K. Chen, A. Harris, J. Draskovic, and P. Schiffer. Granular fragility under thermal cycles. *Granular Matter*, 2009.

[65] Thibaut Divoux, Ion Vassilief, Herve Gayvallet, and Jean-Christophe Geminard. Aging of a granular pile induced by thermal cycling. In Masami Nakagawa and Stefan Luding,

editors, *Aging of a granular pile induced by thermal cycling*, volume 1145, pages 473–476. AIP, 2009.

[66] Steven Slotterback, Leonard Goff, Masahiro Toiya, Jack Douglas, Martin Van Hecke, and Wolfgang Losert. Microscopic rearrangements in a granular column during compaction by thermal cycling. volume 1145, pages 489–491. AIP, 2009.

[67] Watson L. Vargas and J. J. McCarthy. Thermal expansion effects and heat conduction in granular materials. *Physical Review E*, 76, 2007.

[68] C. Argento and D. Bouvard. Thermal conductivity of granular media. *Powders and grains*, pages 129–134, A.A. Balkema, Rotterdam, 1993.

[69] C. Argento and D. Bouvard. Modeling the effective thermal conductivity of random packing of spheres through densification. *International Journal of Heat and Mass Transfer*, 39(7):1343 – 1350, 1996.

[70] M. Kaviany. *Principles of Heat Transfer in Porous Media*. Springer, New York, 1995.

[71] W. L. Vargas and J. J. McCarthy. Stress effects on the conductivity of particulate beds. *Chemical Engineering Science*, 57:3119–3131, 2002.

[72] E. U. Schlünder. Heat transfer to moving spherical packings at short contact times. *International Chemical Engineering*, 20:550–554, 1980.

[73] W. L. Vargas and J. J. McCarthy. Conductivity of granular media with stagnant interstitial fluids via thermal particle dynamics simulation. *International Journal of Heat and Mass Transfer*, 45:4847–4856, 2002.

[74] M. L. Hunt. Discrete element simulations for granular material flows: Effective thermal conductivity and self-diffusivity. *Int. J. Heat Mass Transfer*, 40:3059–3068, 1997.

[75] A. Jagota and C. Y. Hui. The effective thermal conductivity of a packing of spheres. *J. Appl. Mech.*, 57:789–791, 1990.

[76] Y. M. Lee, A. Haji-Sheikh, L. S. Flecher, and G. P. Peterson. Effective thermal conductivity in multidimensional bodies. *Journal of Heat Transfer*, 116:17–27, 1994.

[77] G. Buonanno and A. Carotenuto. The effective thermal conductivity of packed bed of spheres for a finite contact area. *Numerical Heat Transfer, Part A*, 37:343–357, 2000.

[78] F.R.S. G. K. Batchelor and R. W. O'Brien. Thermal or electrical conduction through a granular material. *Proceedings of the Royal Society of London, A*, 355:313–333, 1977.

[79] M. M. Yovanovich. Thermal contact resistance across elastically deformed spheres. *J. Spacecraft Rockets*, 4:119, 1967.

[80] M. A. Lambert and L. S. Fletcher. Thermal contact conductance of spherical rough metals. *Journal of Heat Transfer*, 119:684–690, 1997.

[81] R. Holm. *Electrical Contacts: Theory and Application*. Springer-Verlag, New York, 1967.

[82] C. K. Chan and C. L. Tien. Conductance of packed spheres in vacuum. *Journal of Heat Transfer*, pages 302–308, 1973.

[83] Y.T. Feng, K. Han, C.F. Li, and D.R.J. Owen. Discrete thermal element modelling of heat conduction in particle systems: Basic formulations. *Journal of Computational Physics*, 227(10):5072 – 5089, 2008.

[84] Ronggang Zhang and J. R. Barber. Effect of material properties on the stability of static thermoelastic contact. *Journal of Applied Mechanics*, 57(2):365–369, 1990.

[85] T YEO and JR BARBER. Finite-element analysis of thermoelastic contact stability. *Journal of Applied Mechanics-Transactions of the Asme*, 61(4):919–922, DEC 1994.

[86] J. R. Barber, J. Dundurs, and M. Comninou. Stability considerations in thermoelastic contact. *Journal of Applied Mechanics*, 47(4):871–874, 1980.

[87] J. R. Barber. Stability of thermoelastic contact for the aldo model. *Journal of Applied Mechanics*, 48(3):555–558, 1981.

[88] J. R. Barber and Ronggang Zhang. Transient behaviour and stability for the thermoelastic contact of two rods of dissimilar materials. *International Journal of Mechanical Sciences*, 30(9):691 – 704, 1988.

[89] JR Barber. Thermoelasticity and contact. *Journal of Thermal Stresses*, 22(4):513, 1999.

[90] H Zhu, Z Zhou, R Yang, and A Yu. Discrete particle simulation of particulate systems: A review of major applications and findings. *Chemical Engineering Science*, 63(23):5728–5770, 2008.

[91] C. Thornton and C. W. Randall. Applications of theoretical contact mechanics to solid particle system simulation. In M. Satake and J. T. Jenkins, editors, *Micromechanics of Granular Material*, pages 133–142. Elsevier Science Publishers, Amsterdam, 1988.

[92] M. Satake. Constitution of mechanics of granular materials through the graph theory. In S.C. Cowin and M. Satake, editors, *U.S.-Japan Seminar in Continuum Mechanics and Statistical Approaches in the Mechanics of Granular Materials*, pages 47–62, 1978.

[93] Y. Kaneko, T. Shiojima, and M. Horio. Dem simulation of fluidized beds for gas-phase olefin polymerization. *Chemical Engineering Science*, 54:5809–5821, 1999.

[94] O. R. Walton and R. L. Braun. Viscosity, granular-temperature, and stress calculations for shearing assemblies of inelastic, frictional disks. *J. Rheol.*, 30:949–980, 1986.

[95] H. J. Herrmann and S. Luding. Modeling granular media on the computer. *Continuum Mech. Thermodyn.*, 10:189–231, 1998.

[96] C. S. Campbell. Rapid granular flows. *Ann. Rev. Fluid Mech.*, 22:57–90, 1990.

[97] Rimantas Kačianauskas, Robertas Balevičius, Darius Markauskas, and Algirdas Maknickas. Discrete element method in simulation of granular materials. In *IUTAM Symposium on Multiscale Problems in Multibody System Contacts*, pages 65–74. 2007.

[98] Yanjie Li, Yong Xu, and Colin Thornton. A comparison of discrete element simulations and experiments for 'sandpiles' composed of spherical particles. *Powder Technology*, 160(3):219 – 228, 2005.

[99] C. Thornton (Guest Editor). Special issue on numerical simulations of discrete particle systems. *Powder Technology*, 109:3–292, 2000.

[100] J. P. Bardet. Introduction to computational granular mechanics. In B. Cambou, editor, *Behavior of granular materials*, pages 99–169. Springer-Verlag, 1998.

[101] K. Z. Y. Yen and T. K. Chaki. A dynamic simulation of particle rearrangement in powder packings with realistic interactions. *Journal of Applied Physics*, 71:3164–3173, 1992.

[102] Q. M. Tai and M. H. Sadd. A discrete element study of the relationship of fabric to wave propagational behaviours in granular material. *Int. J. Numer. Anal. Meth. Geomech.*, 21:295–311, 1997.

[103] Y. Tsuji, T. Kawaguchi, and T. Tanaka. Discrete particle simulation of two-dimensional fluidized bed. *Powder Technology*, 77:79–87, 1993.

[104] C. S. Campbell and C. E. Brennen. Chute flows of granular material: some computer simulations. *Journal of Applied Mechanics*, 52:172–178, 1985.

[105] J. J. McCarthy and J. M. Ottino. Particle dynamics simulation: A hybrid technique applied to granular mixing. *Powder Technology*, 97:91–99, 1998.

[106] K. L. Johnson. *Contact Mechanics*. Cambridge University Press, Cambridge, 1987.

[107] R. D. Mindlin. Compliance of elastic bodies in contact. *J. Appl. Mech.*, 16:256–270, 1949.

[108] M. P. Allen and D. J. Tildesley. *Computer Simulation of Liquids*. Clarendon Press, Oxford, 1987.

[109] H. Hertz. üeber die berührung fester elastischer körper. *J. f. reine u. angewandte Math.*, 92:1–15, 1882.

[110] J. Lee and H. J. Herrmann. Angle of repose and angle of marginal stability: molecular dynamics of granular particles. *Journal of Physics A*, 26:373–383, 1993.

[111] J. T. Oden and J. A. C. Martins. Models and computational methods for dynamic friction phenomena. *Computer Methods in Applied Mechanics and Engineering*, 52(1-3):527–634, 1985/9.

[112] V. Buchholtz and T. Poschel. Numerical investigations of the evolution of sandpiles. *Physica A*, 202:390–401, 1994.

[113] J. T. Oden and J. A. C. Martins. Computer methods for dynamic friction phenomena. *Computer Methods in Applied Mechanics and Engineering*, 1984.

[114] R. D. Mindlin and H. Deresiewicz. Elastic spheres in contact under varying oblique forces. *J. Appl. Mech.*, 75:327–344, 1953.

[115] J. Schäfer, S. Dippel, and E. Wolf. Force schemes in simulations of granular materials. *J. Phys. I*, 67:1751–1776, 1991.

[116] H Zhu, Z Zhou, R Yang, and A Yu. Discrete particle simulation of particulate systems: Theoretical developments. *Chemical Engineering Science*, 62(13):3378–3396, 2007.

[117] A. Di Renzo. Comparison of contact-force models for the simulation of collisions in dem-based granular flow codes. *Chemical Engineering Science*, 59(3):525–541, February 2004.

[118] H. Kruggel-Emden, E. Simsek, S. Rickelt, S. Wirtz, and V. Scherer. Review and extension of normal force models for the discrete element method. *Powder Technology*, 171(3):157–173, February 2007.

[119] S. T. Nase, W. L. Vargas, A. A. Abatan, and J. J. McCarthy. Discrete characterization tools for wet granular media. *Powder Technol.*, 116:214–223, 2001.

[120] C. Thornton and Z. Ning. A theoretical model for the stick/bounce behavior of adhesive, elastic-plastic spheres. *Powder Technology*, 99:154–162, 1998.

[121] O. R. Walton. Numerical simulation of inclined chute flows of monodisperse, inelastic, frictional spheres. *Mech. Mat.*, 16:239–247, 1993.

[122] J. Sun and M. M. Chen. A theoretical analysis of heat transfer due to particle impacts. *Int. J. Heat Mass Transfer*, 31:969–975, 1988.

[123] M. R. Sridhar and M. M. Yovanovich. Review of elastic and plastic contact conductance models: Comparison with experiment. *Journal of Thermophysics and Heat Transfer*, 8:633–640, 1994.

[124] M. A. Lambert and L. S. Fletcher. Review of models for thermal contact conductance of metals. *Journal of Heat Transfer*, 11:129–140, 1997.

[125] W. W. Siu and S. H. Lee. Transient temperature computation for a system of multiply contacting spheres in a 180 degrees orientation. *Journal of heat transfer*, 121:739–742, 1999.

[126] Zi Lu, Mohamed Abdou, and Alice Ying. 3d micromechanical modeling of packed beds. *Journal of Nuclear Materials*, 299(2):101–110, 2001.

[127] O. R. Walton. Numerical simulation of inelastic, frictional particle-particle interactions. In M. C. Roco, editor, *Particulate two-phase flow*, page 884, Boston, 1993. Butterworth-Heinemann.

[128] C. Thornton. Coefficient of restitution for collinear collisions of elasti-perfectly plastic spheres. *Journal of Applied Mechanics*, 64:383–386, 1997.

[129] C.A. Coulomb. Sur une application des regles de maximis and minimus a quelques problemes de statique, relatifs a l'architecture, memoires de mathematique et de physique. *Presentes a l'Academie Royale des Sciences, Paris*, pages 343–384, 1773. cited By (since 1996) 1.

[130] A. W. Jenike and R. T. Shield. On the plastic flow of coulomb solids beyond original failure. *Journal of applied mechanics*, 26:599–602, 1959.

[131] J. F. Davidson and R. M. NEDDERMAN. The hour-glass theory of hopper flow. *Chemical Engineering Research and Design*, 51a:29–35, 1973.

[132] C. Brennen and J. C. Pearce. Granular material flow in two-dimensional hoppers. *Journal of Applied Mechanics*, 45(1):43–50, 1978.

[133] S. Ogawa. Multitemperature theory of granular materials. In S. C. Cowin and M. Satake, editors, *Proc. of US-Japan Symp. on Continuum Mechanics and Statistical Approaches to the Mechanics of Granular Media*, page 208, Fukyu-kai, 1978. Gakujutsu Bunken.

[134] Cliff K. K. Lun. Granular dynamics of inelastic spheres in couette flow. *Physics of Fluids*, 8(11):2868–2883, 1996.

[135] D. G. Wang and C. S. Campbell. Reynolds analogy for a shearing granular material. *J. Fluid Mech.*, 244:527–546, 1992.

[136] V. V. R. Natarajan and M. L. Hunt. Heat transfer in vertical granular flows. *Exp. Heat Trans.*, 10:89–107, 1997.

[137] W. Losert, L. Bocquet, T. C. Lubensky, and J. P. Gollub. Particle dynamics in sheared granular matter. *Phys. Rev. Lett.*, 85:1428–1431, Aug 2000.

[138] C. R. Wassgren, M. L. Hunt, P. J. Freese, J. Palamara, and C. E. Brennen. Effects of vertical vibration on hopper flows of granular material. *Physics of Fluids*, 14(10):3439–3448, 2002.

[139] Kiwing To, Pik-Yin Lai, and H. K. Pak. Jamming of granular flow in a two-dimensional hopper. *Phys. Rev. Lett.*, 86:71–74, Jan 2001.

[140] CHARLES S. CAMPBELL. Self-diffusion in granular shear flows. *Journal of Fluid Mechanics*, 348:85–101, 1997.

[141] Yi Zhang and Charles S. Campbell. The interface between fluid-like and solid-like behaviour in two-dimensional granular flows. *Journal of Fluid Mechanics*, 237:541–568, 1992.

[142] Kingsley Iroba, Jochen Mellmann, Fabian Weigler, Thomas Metzger, and Evangelos Tsotsas. Particle velocity profiles and residence time distribution in mixed-flow grain dryers. *Granular Matter*, 13:159–168, 2011. 10.1007/s10035-010-0222-7.

[143] Haitao Xu, Anthony P. Reeves, and Michel Y. Louge. Measurement errors in the mean and fluctuation velocities of spherical grains from a computer analysis of digital images. *Review of Scientific Instruments*, 75(4):811–819, 2004.

[144] G. R. D. MIDI. On dense granular flows. *The European Physical Journal E: Soft Matter and Biological Physics*, 14:341–365, 2004. 10.1140/epje/i2003-10153-0.

[145] Gabriel I. Tardos, M. Irfan Khan, and David G. Schaeffer. Forces on a slowly rotating, rough cylinder in a couette device containing a dry, frictional powder. *Physics of Fluids*, 10(2):335–341, 1998.

[146] Kenneth E. Elliott, Goodarz Ahmadi, and William Kvasnak. Couette flows of a granular monolayer—an experimental study. *Journal of Non-Newtonian Fluid Mechanics*, 74(1–3):89 – 111, 1998.

[147] Chun-Chung Liao, Shu-San Hsiau, Jheng-Syun Li, and Chi-Hwang Tai. The influence of gravity on dynamic properties in sheared granular flows. *Chemical Engineering Science*, 65(8):2531 – 2540, 2010.

[148] Shu-San Hsiau, Jr-Yuan Shiu, Wen-Lung Yang, and Li-Shin Lu. Influence of internal friction on transport properties in sheared granular flows. *AIChE Journal*, 52(10):3592–3599, 2006.

[149] L. Bocquet, W. Losert, D. Schalk, T. C. Lubensky, and J. P. Gollub. Granular shear flow dynamics and forces: Experiment and continuum theory. *Phys. Rev. E*, 65:011307, Dec 2001.

[150] J. E. Ungar Hui k., P. K. Haff and R. Jackson. Boundary conditions for high-shear grain flows. *Journal of Fluid Mechanics*, 145:223–233, 1984.

[151] J. T. Jenkins and M. W. Richman. Boundary conditions for plane flows of smooth, nearly elastic, circular disks. *Journal of Fluid Mechanics Digital Archive*, 171:53–69, 1986.

[152] M. Y. Louge, J. T. Jenkins, and M. A. Hopkins. Computer simulations of rapid granular shear flows between parallel bumpy boundaries. *Physics of Fluids A: Fluid Dynamics*, 2(6):1042–1044, 1990.

[153] D. M. Hanes, J. T. Jenkins, and M. W. Richman. The thickness of steady plane shear flows of circular disks driven by identical boundaries. *Journal of Applied Mechanics*, 55(4):969–974, 1988.

[154] J. T. Jenkins. Boundary conditions for rapid granular flow: Flat, frictional walls. *Journal of Applied Mechanics*, 59(1):120–127, 1992.

[155] Thorsten Pöschel and Volkhard Buchholtz. Complex flow of granular material in a rotating cylinder. *Chaos, Solitons & Fractals*, 5(10):1901–1912, 1995.

[156] J. Rajchenbach. Flow in powders: From avalanches to continuous regime. *Phys. Rev. Lett.*, 65:2221–2224, 1990.

[157] Paul W Cleary and Mark L Sawley. Dem modelling of industrial granular flows: 3d case studies and the effect of particle shape on hopper discharge. *Applied Mathematical Modelling*, 26(2):89 – 111, 2002.

[158] Paul W. Cleary. Dem simulation of industrial particle flows: case studies of dragline excavators, mixing in tumblers and centrifugal mills. *Powder Technology*, 109(1–3):83 – 104, 2000.

[159] Paul W Cleary, Rob Morrisson, and Steve Morrell. Comparison of dem and experiment for a scale model sag mill. *International Journal of Mineral Processing*, 68(1–4):129 – 165, 2003.

[160] J. Duran. Sands, powders, and grains: An introduction to the physics of granular materials. *Springer, New York*, 2000.

[161] T. Pahtz, H. J. Herrmann, and T. Shinbrot. Why do particle clouds generate electric charges? *Nat Phys*, 6(5):364–368, 05 2010.

[162] Y. C. Zhou, B. H. Xu, A. B. Yu, and P. Zulli. Numerical investigation of the angle of repose of monosized spheres. *Physical Review E*, 64(2), 07 2001.